Geophysical Journal International

Advancing Astronomy and Geograpies

Geophys. J. Int. (2023) 233, 586–626
Advance Access publication 2022 November 25

https://doi.org/10.1093/gji/ggac467

A discontinuous Galerkin method for sequences of earthquakes and aseismic slip on multiple faults using unstructured curvilinear grids

Carsten Uphoff, Dave A. May and Alice-Agnes Gabriel 1,2

¹Department of Earth and Environmental Sciences, Ludwig-Maximilians-University, 80333 Munich, Germany. E-mail: gabriel@geophysik.uni-muenchen.de ²Scripps Institution of Oceanography, UC San Diego, La Jolla, CA 92093, USA

Accepted 2022 November 18. Received 2022 November 18; in original form 2022 January 17

SUMMARY

Physics-based simulations provide a path to overcome the lack of observational data hampering a holistic understanding of earthquake faulting and crustal deformation across the vastly varying space-time scales governing the seismic cycle. However, simulations of sequences of earthquakes and aseismic slip (SEAS) including the complex geometries and heterogeneities of the subsurface are challenging. We present a symmetric interior penalty discontinuous Galerkin (SIPG) method to perform SEAS simulations accounting for the aforementioned challenges. Due to the discontinuous nature of the approximation, the spatial discretization natively provides a means to impose boundary and interface conditions. The method accommodates 2-D and 3-D domains, is of arbitrary order, handles subelement variations in material properties and supports isoparametric elements, that is, high-order representations of the exterior boundaries, interior material interfaces and embedded faults. We provide an open-source reference implementation, Tandem, that utilizes highly efficient kernels for evaluating the SIPG linear and bilinear forms, is inherently parallel and well suited to perform high-resolution simulations on large-scale distributed memory architectures. Additional flexibility and efficiency is provided by optionally defining the displacement evaluation via a discrete Green's function approach, exploiting advantages of both the boundary integral and volumetric methods. The optional discrete Green's functions are evaluated once in a pre-computation stage using algorithmically optimal and scalable sparse parallel solvers and pre-conditioners. We illustrate the characteristics of the SIPG formulation via an extensive suite of verification problems (analytic, manufactured and code comparison) for elastostatic and quasi-dynamic problems. Our verification suite demonstrates that high-order convergence of the discrete solution can be achieved in space and time and highlights the benefits of using a high-order representation of the displacement, material properties and geometries. We apply *Tandem* to realistic demonstration models consisting of a 2-D SEAS multifault scenario on a shallowly dipping normal fault with four curved splay faults, and a 3-D intersecting multifault scenario of elastostatic instantaneous displacement of the 2019 Ridgecrest, CA, earthquake sequence. We exploit the curvilinear geometry representation in both application examples and elucidate the importance of accurate stress (or displacement gradient) representation on-fault. This study entails several methodological novelties. We derive a sharp bound on the smallest value of the SIPG penalty ensuring stability for isotropic, elastic materials; define a new flux to incorporate embedded faults in a standard SIPG scheme; employ a hybrid multilevel pre-conditioner for the discrete elasticity problem; and demonstrate that curvilinear elements are specifically beneficial for volumetric SEAS simulations. We show that our method can be applied for solving interesting geophysical problems using massively parallel computing. Finally, this is the first time a discontinuous Galerkin method is published for the numerical simulations of SEAS, opening new avenues to pursue extreme scale 3-D SEAS simulations in the future.

Key words: Seismic cycle; Transient deformation; Numerical approximations and analysis; Numerical modelling; Earthquake dynamics; Earthquake interaction, forecasting, and prediction.

LIST OF SYMBOLS

Governing equations

Symbol	Definition	Dimension
D	Spatial dimension	Scalar (\mathbb{Z}^+)
x_i, x	Spatial coordinate (component, vector)	\mathbb{R}^D
t	Time	Scalar $(\mathbb{R}_{>0})$
n_i , \boldsymbol{n}	Unit normal vector to a surface (component, vector)	\mathbb{R}^D –
u_i , \boldsymbol{u}	Displacement (component, vector)	\mathbb{R}^D
v_i , \boldsymbol{v}	Velocity (component, vector)	\mathbb{R}^D
S_i , S	Slip (component, vector)	\mathbb{R}^{D-1}
V_i, V	Slip rate (component, vector)	\mathbb{R}^{D-1}
В	Fault basis	Matrix, $\mathbb{R}^{D \times (D-1)}$
$g_{:}^{D}$	Imposed boundary values associated with the Dirichlet constraints	\mathbb{R}^D
g_i^D g_i^F	Imposed boundary values associated with the fault constraints	\mathbb{R}^D
$\sigma_{ij}, \boldsymbol{\sigma}$	Stress (component, tensor)	Tensor, $\mathbb{R}^{D \times D}$
μ, λ	Shear modulus (first Lame parameter), second Lame parameter	Scalar
τ_i , $\boldsymbol{\tau}$	Shear traction (component, vector)	\mathbb{R}^{D-1}
τ_S	Fault strength	Scalar $(\mathbb{R}_{\geq 0})$
T_i, T	Shear traction on fault (component, vector)	\mathbb{R}^{D-1}
σ_n	Compressive normal stress	Scalar $(\mathbb{R}_{\geq 0})$
T_{i}^{0}, T^{0}	Background/reference value for shear traction	\mathbb{R}^{D-1}
T_i^0, T^0 σ_n^0	Background/reference value for compressive normal stress	Scalar $(\mathbb{R}_{\geq 0})$
$\psi^{''}$	State variable	Scalar
F	Effective coefficient of friction	Scalar
Γ^D , Γ^N , Γ^F	Boundaries associated with Dirichlet, Neumann and fault constraints	

Numerics

Symbol	Definition	
$\overline{\mathcal{T}_h}$	Curvilinear mesh	
$\dim(\mathcal{T}_h)$	Number of elements in the mesh	
$E \in \mathcal{T}_h$	Element in physical coordinates (x)	
$\dim(\mathcal{T}_h)$	Number of elements in the mesh	
$\dim(\Gamma^F)$	Number of fault cell facets	
ξ_i , ξ	Reference spatial coordinate (component, vector)	
X_E	Transformation for element E from reference to physical coordinates	
\hat{E}	Element E mapped to reference coordinates ξ	
\widehat{n}_i^{lpha} , $\widehat{m{n}}^{lpha}$	Outward point normal vector $(0 \le \alpha \le D)$ from the boundary of \hat{E} (component, vector)	
$P_N(\hat{E})$	Space of polynomials of complete degree N defined over \hat{E}	
Σ_h, V_h	Function space for stress and displacement	
e	Facet of E	
$a(\cdot,\cdot)$	Bilinear form	
$L(\cdot)$	Linear form	
δ_e	SIPG penalty	
ϕ_k^E	kth basis function defined on E	
\tilde{A}	Matrix associated with $a(\cdot, \cdot)$	
b	Vector associated with $L(\cdot)$	
<u>u</u>	Vector of finite-element coefficients associated with displacement u	
<u>S</u>	Vector of finite-element coefficients associated with slip S	
$\frac{S}{\underline{\psi}} \frac{\psi}{N_h}$	Vector of finite-element coefficients associated with state variable ψ	
$\overline{N_h}$	Number of displacement unknowns in the volume	
n_h	Number of slip unknowns on the fault	

1 INTRODUCTION

Numerical modelling is an important tool to enhance our understanding of how faults slip, since the spatial and temporal scales involved in (sequences of) earthquakes render the direct observation of earthquake source processes difficult or infeasible (e.g. Lapusta *et al.* 2019). While historical and geological records have been used to construct catalogues of major earthquakes on known natural fault systems that extend over several thousands of years (Ben-Menahem 1991; Rockwell *et al.* 2015), the lack of space–time complete, quantitative data on fundamental observables of the seismic cycle such as the magnitude and recurrence interval of large earthquakes challenges constructing

seismic hazard maps and estimating aftershocks probabilities in the aftermath of large earthquakes (Petersen *et al.* 2014; Milner *et al.* 2021). Computational models informed by laboratory experiments and first-order physical principles provide a path to constrain sets of plausible scenarios that extend the knowledge beyond regional statistical laws and enhance our fundamental understanding of earthquake faulting and crustal deformation on different space—time scales.

Numerical simulations of sequences of earthquakes and aseismic slip (termed 'SEAS' models) aim to capture the complete seismic cycle in a single self-consistent model (Rice & Tse 1986; Kato 2002; Lapusta & Liu 2009; Kaneko et al. 2011; Segall & Bradley 2012; Barbot et al. 2012; Allison & Dunham 2018; Abdelmeguid et al. 2019; Mckay et al. 2019; Erickson et al. 2020; Romanet & Ozawa 2022; Barbot 2021; Jiang et al. 2022; Erickson et al. 2022). SEAS models consider unified earthquake system dynamics by combining the inter-seismic phase, spontaneous earthquake nucleation as well as co-seismic and post-seismic slip to connect long-term deformation (expressed in fault zone rheology, tectonics and geometry) and short-term seismicity. In SEAS models, pre-defined fault surfaces obey a rate- and state-dependent friction law, which well describes frictional sliding for many rock types in laboratory experiments (Dieterich 1979; Ruina 1983; Dieterich & Kilgore 1994). SEAS simulations typically do not account for changes in fault geometry. The linear theory of elasticity, ubiquitous in seismology, is used to compute the mechanical response to the displacement discontinuity on-fault and sets shear and normal traction in the rate and state constitutive relation. Often, the required initial and interface conditions governing SEAS models, in particular the loading stresses and constitutive parameters, are not well constrained, necessitating simulations for a wide range of parameters. However, already a single SEAS simulation for one choice of parameters is computationally challenging: temporal scales vary from milliseconds to years, as a fault may be 'locked' for decades, centuries, or millennia, and then rupture within seconds. In space, SEAS models need to resolve hundreds of kilometres of tectonic structures to metre-scale resolution on-fault.

Due to the wide variability in timescales, the acceleration term in the elastodynamic relations is often neglected, hence seismic waves are not modelled and transient wave-mediated stress transfer is ignored. The radiation damping part of the inertia term represents the outflow of energy due to the instantaneous fault response to slip (Cochard & Madariaga 1994; Tada *et al.* 2000). SEAS models that neglect inertia and include radiation damping have been termed quasi-dynamic and can capture the period of stress accumulation and slow movements across faults (e.g. Rice 1993; Segall *et al.* 2010; Perez-Silva *et al.* 2021). Quasi-dynamic models quantitatively differ during the co-seismic phase in comparison to fully dynamic models (that include dynamic earthquake rupture) and it is under discussion under which circumstances the qualitative behaviour is affected (Lapusta & Liu 2009; Thomas *et al.* 2014; Romanet & Ozawa 2022). Models that include inertial effects are typically restricted to idealized scenarios. Efficient long-term seismicity models considering larger scale fault networks using semi-kinematic approaches have been developed (Tullis *et al.* 2012; Dieterich *et al.* 2015) but are approximating or neglecting the effects of inertia effects, slow slip and inelastic deformation. Switching between fully dynamic and quasi-dynamic approaches is possible but comes at great computational expense (Kaneko *et al.* 2011; Aagaard *et al.* 2013).

A variety of numerical discretization methods have been applied to SEAS type problems, including the boundary integral method (BIM) and boundary element method (BEM, Lapusta *et al.* 2000; Liu & Rice 2005; Lapusta & Liu 2009; Segall & Bradley 2012; Bradley 2014; Li & Liu 2016, 2017; Barbot 2019; Luo *et al.* 2017), the finite-difference method (FDM, Erickson & Dunham 2014; Allison & Dunham 2018; Pranger 2021; Almquist & Dunham 2021) and the finite-element method (FEM, Kaneko *et al.* 2011; Aagaard *et al.* 2013; Kozdon 2019; Luo *et al.* 2020). In the BEM one only needs to discretize the domain boundaries and the fault (or only the fault for specific geometries such as the half-space), such that the dimensionality of the problem is effectively reduced by one. Restricting models to single planar faults allows using fast Fourier transforms (FFT) in BEM, and assuming that fault slip does not alter the BEM analytical fundamental solution allows handling fault systems of arbitrary geometry. However, this method relies on the existence of the analytic fundamental solution (Chen & Zhou 2010), which is typically only available for homogeneous material parameters. BEM is generally not applicable for scenarios in general heterogeneous media or requiring more flexible boundary conditions (e.g. Erickson & Dunham 2014; Thakur *et al.* 2020). While heterogeneous material parameters can be easily included in the FDM and FEM, these methods inherently require more degrees of freedom than BEM since they discretize the volume.

Discontinuous Galerkin (DG) FEMs are increasingly popular for solving general hyperbolic problems (e.g. Hesthaven & Warburton 2008; Reinarz et al. 2020) including seismic wave propagation and dynamic earthquake rupture simulations (e.g. Moczo et al. 2021). DG methods combine advantages from finite-volume method and FEM (Hill 1973; Cockburn & Shu 1989; Dumbser & Käser 2006) and are advantageous for modelling wave phenomena due to their low numerical dispersion and well-characterized numerical dissipation (e.g. Kopriva et al. 2017). DG method's usage of numerical fluxes allows to naturally include nonlinear interface conditions (e.g. Tago et al. 2012; Krenz et al. 2021). One of the perceived disadvantages of DG methods is their increased computational cost (e.g. as compared to FEM or spectral element method) associated with the duplicate degrees of freedom on each cell facet and the need to perform both, operations over cell volumes and cell facets. However, geometrically and rheologically complicated wave propagation and dynamic rupture simulations using DG can be performed in a few hours on large-scale high-performance computing (HPC) infrastructure (e.g. Wilcox et al. 2010; Heinecke et al. 2014; Uphoff et al. 2017; Dorozhinskii & Bader 2021). For example, the open-source software SeisSol combines a modal DG formulation using the Godunov flux with Arbitrary DERivative time stepping (ADER-DG) leading to high-order accuracy in space and in time and exploiting on-node hardware optimizations (e.g. Dumbser & Käser 2006; Pelties et al. 2014; Wollherr et al. 2018; Wolf et al. 2022).

While to the best of our knowledge the DG method has not been published to date for SEAS problems, it is promising for the following reasons:

- (i) The method is geometrically flexible, meaning there are few restrictions on the complexity and shape of the fault geometry. Such flexibility is realized as the method permits the domain to be decomposed into a set of triangles or quadrilaterals (2-D), or a set of tetrahedra or hexahedra (3-D), and allows for unstructured meshes to be used. Static spatial adaptivity can be applied to bridge spatial scales (e.g. Mazzieri *et al.* 2013; Ulrich *et al.* 2022).
- (ii) Values defined on the faces of each cell are double-valued such that the DG function spaces naturally include the displacement discontinuity at the (mesh-aligned) fault. There is no need to split nodes at the fault or to introduce Lagrange multipliers as is the case in the continuous Galerkin FEM (Kaneko *et al.* 2011; Aagaard *et al.* 2013). These characteristics of the DG scheme have been successfully exploited in modelling faults in dynamic rupture applications (e.g. Tago *et al.* 2012; Pelties *et al.* 2014).
- (iii) The polynomial degree of the basis function can be chosen flexibly and the implementation is agnostic with respect to the polynomial degree. Thus, we obtain an arbitrary high-order method on unstructured grids. When high-order convergence is achieved for sufficiently smooth solutions, less degrees of freedom are required in comparison to low-order methods. Establishing whether high-order convergence can be achieved for SEAS problems using symmetric interior penalty discontinuous Galerkin (SIPG) is central to this paper.
- (iv) DG methods are provably stable for a wide range of physical processes governed by elliptic, parabolic and hyperbolic partial differential equations (e.g. Hill 1973; Cockburn & Shu 1989; Grote *et al.* 2006; Dumbser & Käser 2006; Hesthaven & Warburton 2008; Rivière 2008; Reinarz *et al.* 2020; Duru *et al.* 2022).
- (v) The physical characteristics of quasi-dynamic SEAS require an incredibly large number of time steps to be performed (in the order of million time steps). To enable both high-resolution 3-D simulations and rapid-to-solution, parallelism must be exploited. The DG discretization is well suited to complex large-scale simulations and scalable up to the largest-available supercomputers (Wilcox *et al.* 2010; Heinecke *et al.* 2014; Kronbichler *et al.* 2017; Uphoff *et al.* 2017; Kronbichler & Kormann 2019; Schoeder *et al.* 2019; Arndt *et al.* 2020; Krenz *et al.* 2021).

In this paper, we introduce the symmetric interior penalty Galerkin (SIPG) method—which is a DG scheme suitable for discretizing elastostatic (i.e. elliptic) problems—for SEAS simulations on unstructured curvilinear meshes. DG methods for elastostatics have been thoroughly analysed mathematically (Rivière 2008) but have not been widely adopted. One may speculate that this is due to the perception that DG methods for elliptic problems are expensive (Kirby *et al.* 2012). SIPG is an interior penalty method which classically uses penalties to weakly enforce (i.e. integral constraints) both the continuity of the solution and the Dirichlet boundary conditions. Interior penalty methods come in many flavours, including non-symmetric and symmetric variants. SIPG is desirable since it leads to a symmetric operator and is provably stable provided the penalty is chosen large enough. Its symmetry property is important to establish robust iterative solvers.

In the context of using SIPG to discretize the elastostatic problem this study entails several novelties: we define a new flux to incorporate embedded faults with the standard SIPG scheme. We derive a sharp bound on the smallest value of the SIPG penalty ensuring stability for isotropic and elastic materials. Similar analysis has been conducted for the Poisson equation (Epshteyn & Rivière 2007) and the variable viscosity Stokes problems (Charrier *et al.* 2017), but not yet for the elasticity equations. We employ a hybrid multilevel pre-conditioner for the discrete elasticity problem following Fehn *et al.* (2020), who employed such multilevel solvers for the constant coefficient Poisson problem. Interestingly, we find that the convergence of our solver is insensitive to embedded discontinuities in the model: the presence of faults governed by rate-and-state friction does not alter the solver's convergence properties. We show that curvilinear elements are specifically beneficial for volumetric simulations of SEAS. Lastly, we demonstrate that our method can be applied for solving interesting geophysical problems using massively parallel computing.

The evaluation of the SIPG method is realized through our open-source reference implementation *Tandem*, which exploits all of the aforementioned benefits. The novelty and functionality of the computational SEAS framework can be summarized as follows:

- (i) support for 2-D and 3-D spatial discretizations using unstructured meshes comprised of triangles (2-D) and tetrahedra (3-D);
- (ii) support for high-order (curvilinear) representation of exterior boundaries and interfaces (faults);
- (iii) subelement (high-order accurate) representation of material properties and subelement (high-order accurate) representation of slip, slip rate in SEAS problems;
- (iv) efficient kernels for the assembly of DG operators and residual evaluation;
- (v) a fully parallel implementation, including mesh loading, solution stage, output and visualization;
- (vi) access to state-of-the art solvers, pre-conditioners and time integrators by using the Portable, Extensible Toolkit for Scientific Computation (PETSc);
- (vii) support to optionally compute the discrete Green's function (i.e. the affine function which maps slip to traction) via efficient scalable (algorithmic and parallel) solvers.

The remainder of this paper is organized as follows. We begin with reviewing the quasi-dynamic SEAS model in Section 2. The SIPG method supporting the fault slip boundary condition is introduced in Section 3. Specific aspects of the DG implementation on curvilinear meshes are presented in Section 4 and coupling to rate-and-state friction is discussed in Section 5. In Section 6, we show how the discrete analogue to a Green's function can be obtained. Results of our numerical experiments are reported in Sections 7 and 8, with the SIPG verification presented in Section 7 and the 2-D SEAS splay fault and 3-D elastostatic Ridgecrest demonstrators presented in Section 8. We discuss our results in Section 9 and conclude in Section 10.

2 QUASI-DYNAMIC SEAS MODEL

We here present the equations of the quasi-dynamic SEAS model. The equations are formulated for D = 2 and 3, that is, for two and three space dimensions. We note that summation over lower indices (but not upper indices) appearing twice is implied throughout the paper.

2.1 Rate and state friction

In the framework of rate and state friction, the effective coefficient of friction F depends on the slip-rate vector V and the scalar state variable ψ , such that fault strength τ_S is given by

$$\tau_S = \sigma_n F(|V|, \psi),\tag{1}$$

where σ_n is the normal stress and $|\cdot|$ denotes the Euclidean norm of a vector. The evolution of the state variable is governed by the following ordinary differential equation (ODE):

$$\frac{\mathrm{d}\psi}{\mathrm{d}t} = G(|V|, \psi). \tag{2}$$

The slip-rate vector has D-1 components, since the slip rate normal to the fault is defined to be zero (we ignore fault opening). The basis of the slip-rate vector is given by the D-1 unit tangents of the fault. By stacking the tangents in the $D\times (D-1)$ matrix \mathbf{B} we relate the slip-rate vector to the velocity vector \mathbf{v} as $[\![v_i]\!] = B_{ij}V_j$. The jump operator $[\![\cdot]\!]$ is defined as $[\![v_i]\!] := v_i^- - v_i^+$ and we define that the normal vector \mathbf{n} points from the '-' side to the '+' side of a fault discontinuity.

With the conventions adopted, the fault strength is related to shear traction τ and slip rate by (Day et al. 2005)

$$|\tau| \le \tau_S,\tag{3}$$

$$\tau_S V + \tau |V| = 0. \tag{4}$$

The first equation limits the traction by the fault strength and the second equation ensures that traction is antiparallel to slip rate. Moreover, it follows from the second equation that either slip rate is zero or the magnitude of shear traction is equal to fault strength. That is, if $|V| \neq 0$ then

$$-\tau = \sigma_n F(|V|, \psi) \frac{V}{|V|}. \tag{5}$$

In this paper, we use the regularized version of the rate and state friction law (Rice & Ben-Zion 1996; Lapusta et al. 2000)

$$F(|V|, \psi) = a \operatorname{arcsinh}\left(\frac{|V|}{2V_0} \exp\left(\frac{\psi}{a}\right)\right)$$
 (6)

and the Dieterich-Ruina ageing law

$$G(|V|, \psi) = \frac{bV_0}{L} \left(\exp\left(\frac{f_0 - \psi}{b}\right) - \frac{|V|}{V_0} \right),\tag{7}$$

where a, b, V_0 , f_0 , L are (possibly space-dependent) constants. We note that the form of the ageing law in eq. (7) is equivalent to the more familiar form $d\theta dt = 1 - |V|\theta/L$ with the substitution $\psi = f_0 + b\ln(V_0\theta/L)$. However, we prefer eq. (7) which results in the state variable being order one, that is, $\psi \sim \mathcal{O}(1)$. In addition, this formulation avoids $\theta < 0$.

2.2 Quasi-dynamic approximation

The theory of linear elasticity is used to compute the mechanic response to slip on a fault. In the quasi-dynamic approach the acceleration term $\rho \frac{dv}{dt}$ is removed from the elastodynamic problem such that one needs to solve the following conservation of momentum equation

$$-\frac{\partial \sigma_{ij}(\mathbf{u})}{\partial x_j} = f_i,\tag{8}$$

where σ_{ij} is the stress, \boldsymbol{u} the displacement and f_i is the body-force vector. The constitutive relationship is given by

$$\sigma_{ij}(\mathbf{u}) = c_{ijkl}\varepsilon_{kl}(\mathbf{u}), \quad \varepsilon_{ij}(\mathbf{u}) = \frac{1}{2} \left(\frac{\partial u_i}{\partial x_j} + \frac{\partial u_j}{\partial x_i} \right), \tag{9}$$

where c_{ijkl} is the stiffness tensor and ε_{ij} the strain tensor. Here, we further assume the material is isotropic and thus $c_{ijkl} = \lambda \delta_{ij} \delta_{kl} + \mu(\delta_{ik} \delta_{jl} + \delta_{il} \delta_{jk})$, where λ and μ are the Lamé parameters and δ is the Kronecker symbol.

We consider three types of boundary conditions to define a unique displacement solution for eq. (8): (i) a free surface condition imposed as a Neumann boundary condition on Γ^N in which we specify $\sigma_{ij}(\boldsymbol{u})n_j=0$; (ii) tectonic loading which is imposed as a Dirichlet boundary condition on Γ^D in which we specify $u_i=g_i^D$ and (iii) slip imposed as an interface condition on an embedded surface Γ^F . The slip vector \boldsymbol{S} on the fault is related to the displacement vector \boldsymbol{u} by $[\![u_i]\!]=B_{ij}S_j=g_i^F$.

Given the displacement u that solves the boundary value problem, one computes the shear traction T in the fault-aligned basis using

$$T_i = T_i^0 + B_{ii}\sigma_{ik}(\mathbf{u})n_k \tag{10}$$

and the compressive normal stress σ_n via

$$\sigma_n = \max\left(0, \sigma_n^0 - n_i \sigma_{ij}(\mathbf{u}) n_j\right). \tag{11}$$

In eqs (10) and (11), the loading stress field is included with T_i^0 and σ_n^0 . One might consider requiring $\tau = T$, however, the resulting system of equations diverges (Rice 1993). Instead, the radiation damping term $-\eta V$ is added, with η being half the shear wave impedance. That is, one requires $T = \tau - \eta V$ such that

$$-T = \sigma_n F(|V|, \psi) \frac{V}{|V|} + \eta V. \tag{12}$$

We note that the radiation damping term appears naturally when deriving non hyper-singular BEMs (Cochard & Madariaga 1994; Perrin *et al.* 1995; Geubelle & Rice 1995; Tada *et al.* 2000) and when considering the exact Riemann problem at the fault, which can be used to implement provable stable fault boundary conditions for the fully dynamic equations (Duru & Dunham 2016; Uphoff 2020).

2.3 Summary of equations

We denote the physical domain by Ω and its boundary by $\partial\Omega$. We assume that Ω is defined in $\mathbb{R}^{\mathbb{D}}$, where D=2 or 3. The boundary of the domain $\partial\Omega$ is partitioned in three pairwise disjoint sets: a Dirichlet boundary Γ^D , Neumann boundary Γ^N and internal fault boundary Γ^F , On Γ^F we solve the following rate and state friction relations

$$-T_{i} = \sigma_{n} F(|V|, \psi) \frac{V_{i}}{|V|} + \eta V_{i},$$

$$\frac{d\psi}{dt} = G(|V|, \psi),$$

$$\frac{dS_{i}}{dt} = V_{i}, \quad \text{where}$$

$$T_{i} = T_{i}^{0} + B_{ji}\sigma_{jk}(\mathbf{u})n_{k},$$

$$\sigma_{n} = \max\left(0, \sigma_{n}^{0} - n_{i}\sigma_{ij}(\mathbf{u})n_{j}\right),$$
(13)

and the displacement is the solution of the boundary value problem

$$-\frac{\partial \sigma_{ij}(\boldsymbol{u})}{\partial x_{j}} = f_{i} \qquad \text{in } \Omega,$$

$$\sigma_{ij}(\boldsymbol{u}) = c_{ijkl} \varepsilon_{kl}(\boldsymbol{u}) \qquad \text{in } \Omega,$$

$$u_{i} = g_{i}^{D} \qquad \text{on } \Gamma^{D},$$

$$\sigma_{ij}(\boldsymbol{u}) n_{j} = 0 \qquad \text{on } \Gamma^{N},$$

$$\|u_{i}\| = B_{ij} S_{i} = g_{i}^{F} \qquad \text{on } \Gamma^{F}.$$

$$(14)$$

3 SYMMETRIC INTERIOR PENALTY GALERKIN

In this section, we develop a DG method to solve the elasticity subproblem eq. (14) numerically. DG schemes for elliptic PDEs are typically stated either in the *flux formulation* or in the *primal formulation* (Arnold *et al.* 2002). Central to the flux formulation is the *numerical flux* which approximates the stress tensor and the displacement on the boundary of an element. The numerical flux is typically single-valued but this is not a necessity. We introduce a double-valued numerical flux that is equivalent to the numerical flux of the symmetric interior penalty Galerkin (SIPG) method, except on the fault Γ^F . We then derive the primal formulation from the flux formulation. The primal formulation defines a variational problem common in finite elements, that is, it is stated in terms of a bilinear and a linear form, and is useful to assemble the stiffness matrix.

3.1 Flux formulation

We note that $c_{ijrs} \frac{\partial u_r}{\partial x_s} = c_{ijrs} \varepsilon_{kl}(\boldsymbol{u})$ due to the symmetries in the stiffness tensor $(c_{ijrs} = c_{ijsr})$ and rewrite the elasticity PDEs as the first-order system

$$\sigma_{ij} - c_{ijrs} \frac{\partial u_r}{\partial x_s} = 0,$$

$$-\frac{\partial \sigma_{ij}}{\partial x_j} = f_i.$$
(15)

Table 1. Summary of the numerical flux. The numerical flux is double-valued on $\Gamma^0 \cup \Gamma^F$ and single-valued on $\Gamma^D \cup \Gamma^N$.

Interior	$\widetilde{\sigma}_{ij}$	$\{\widetilde{u}_i\}$	$[\![\widetilde{u}_i]\!]$
$e \in \Gamma^0$	$\{c_{ijrs}\frac{\partial u_r}{\partial x_s}\} - \delta_e[[u_i n_j]]$	$\{\{u_i\}\}$	0
$e\in\Gamma^F$	$\{c_{ijrs}\frac{\partial u_r}{\partial x_s}\} - \delta_e(\llbracket u_i \rrbracket - g_i^F)n_j$	$\{\{u_i\}\}$	g_i^F
Boundary	$\widetilde{\sigma}_{ij}$	\widetilde{u}_i	
$e \in \Gamma^D$	$c_{ijrs} \frac{\partial u_r}{\partial x_s} - \delta_e(u_i - g_i^D) n_j$	g_i^D	
$e \in \Gamma^N$	0	u_i	

The domain Ω is approximated using a conforming curvilinear mesh $\mathcal{T}_h = \{E\}$. The mesh is defined via mapping $X_E : \widehat{E} \to E$ from the reference element \widehat{E} to the physical element E. We require that X_E is invertible. The reference element \widehat{E} is given by

$$\widehat{E} = \left\{ \boldsymbol{\xi} : 0 \le \boldsymbol{\xi}, \sum_{i=1}^{D} \xi_i \le 1 \right\},\tag{16}$$

thus we have a reference triangle for D = 2 and a reference tetrahedron for D = 3.

The mapping relates the quantities (σ, u) on the physical element to the quantities $(\widehat{\sigma}, \widehat{u})$ on the reference element via the following transformation:

$$\sigma = (\widehat{\sigma}(\nabla X_E)^{-1}) \circ X_F^{-1}, \quad u = \widehat{u} \circ X_F^{-1}. \tag{17}$$

We introduce the finite-element spaces

$$\Sigma_{h} = \left\{ \boldsymbol{\sigma} \in [L^{2}(\Omega)]^{D \times D} : \widehat{\boldsymbol{\sigma}}|_{E} \in [P_{N}(\widehat{E})]^{D \times D} \ \forall E \in \mathcal{T}_{h} \right\},
V_{h} = \left\{ \boldsymbol{u} \in [L^{2}(\Omega)]^{D} : \widehat{\boldsymbol{u}}|_{E} \in [P_{N}(\widehat{E})]^{D} \ \forall E \in \mathcal{T}_{h} \right\},$$
(18)

where $P_N(\widehat{E})$ is the space of polynomials of degree at most N on \widehat{E} . Note that we have the inclusion $\nabla_h V_h \subset \Sigma_h$, where ∇_h takes the gradient element-wise.

We multiply eq. (15) with test functions $\tau \in \Sigma_h$ and $v \in V_h$, integrate over element E, integrate by parts, and introduce numerical fluxes $\widetilde{\sigma}_{ij}$ and \widetilde{u}_i :

$$\int_{F} \tau_{ij} \sigma_{ij} \, \mathrm{d}\mathbf{x} + \int_{F} \frac{\partial (\tau_{ij} c_{ijrs})}{\partial x_{s}} u_{r} \, \mathrm{d}\mathbf{x} - \int_{\partial F} \tau_{ij} c_{ijrs} \widetilde{u}_{r} n_{s} \, \mathrm{d}s = 0; \tag{19}$$

$$\int_{E} \frac{\partial v_{i}}{\partial x_{j}} \sigma_{ij} \, \mathrm{d}\mathbf{x} - \int_{\partial E} v_{i} \widetilde{\sigma}_{ij} n_{j} \, \mathrm{d}\mathbf{s} = \int_{E} v_{i} f_{i} \, \mathrm{d}\mathbf{x} \,. \tag{20}$$

We need a few definitions in order to define the numerical flux. First, let $\Gamma := \bigcup_{E \in \mathcal{T}_h} \partial E$ be the set of facets. The set of interior faces is given by $\Gamma^i := \Gamma \setminus \partial \Omega$ and the set of non-fault interior faces is given by $\Gamma^0 = \Gamma^i \setminus \Gamma^F$. Second, we define averages and jumps. Let E_1^e and E_2^e be two elements that share an edge $e \in \Gamma^i$, that is, $e = E_1^e \cap E_2^e$. Then, the average and jump of a quantity w along e is given by

$$\{w\} = \frac{1}{2}(w|_{E_1^e} + w|_{E_2^e}), \quad \llbracket w \rrbracket = w|_{E_1^e} - w|_{E_2^e}. \tag{21}$$

When the normal n^e is included in the average or jump we define that it is oriented from E_1^e to E_2^e . For convenience, we also define average and jump for $e \in \partial \Omega$:

$$\{w\} = w|_{E_1^e}, \quad [\![w]\!] = w|_{E_1^e}.$$
 (22)

The numerical flux we adopt is equivalent to the usual SIPG numerical flux (Arnold *et al.* 2002; Rivière 2008), except on the fault. For $e \in \Gamma^F$ we define the fluxes according to

$$\widetilde{\sigma}_{ij} = \left\{ \left[c_{ijrs} \frac{\partial u_r}{\partial x_o} \right] - \delta_e \left(\left[\left[u_i \right] \right] - g_i^F \right) n_j,$$
(23a)

$$\{\widetilde{u}_i\} = \{u_i\},\tag{23b}$$

$$[\widetilde{u}_i] = g_i^F. \tag{23c}$$

By allowing the displacement flux to be double-valued we can prescribe the fault slip g_i^F . Moreover, in the stress flux, we add a penalty term that becomes active when the displacement discontinuity differs from the prescribed slip. The penalty parameter δ_e needs to be large enough to ensure stability. In Appendix A, we give a lower bound on δ_e . All numerical fluxes used are summarized in Table 1.

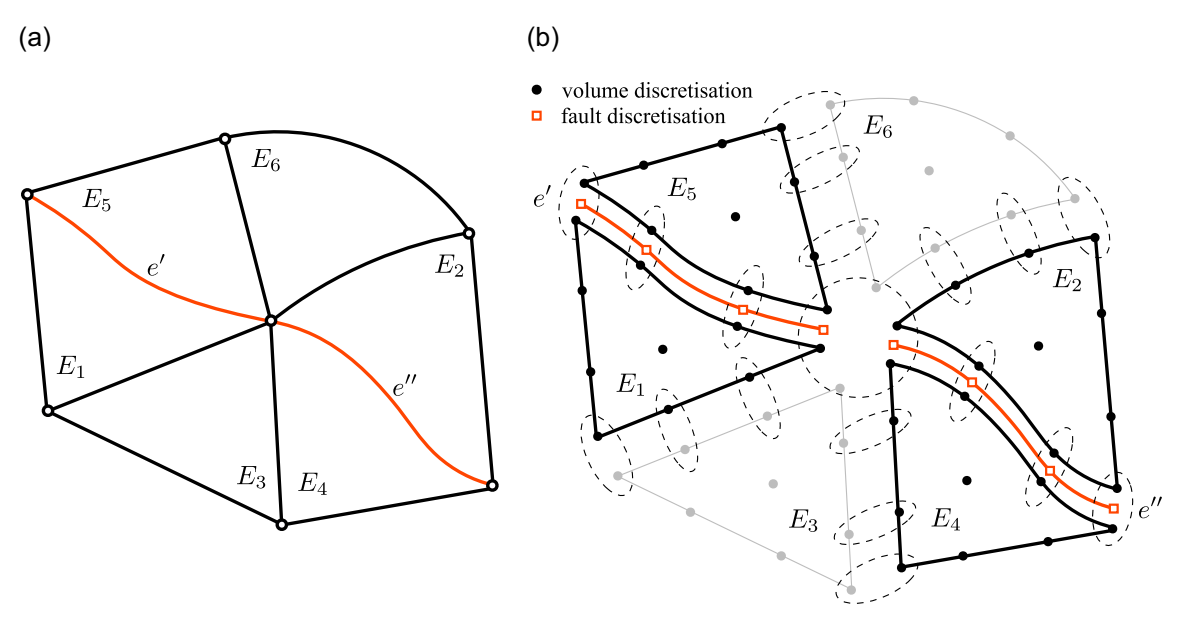


Figure 1. DG representation of a SEAS problem. (a) Partitioning of the physical domain into a set of cells E_k , k = 1, ..., 6 and two fault facets e', e'' (shown in red). The fault facets are given by $e' = \partial E_1 \cap \partial E_5$ and $e'' = \partial E_4 \cap \partial E_2$. (b) DG representation of the fields and parameters defined over cells and fault facets using N = 3. Nodal basis function locations for the cell disretization are denoted via solid circles, whilst nodal basis function locations for the fault discretization are denoted via open squares. The boundaries of cells E_2 , E_6 (shown in light grey) do not overlap with the fault Γ^F . To emphasis the discontinuous nature of the DG representation and the weak coupling between the cells, cells and facets are depicted as being disjoint from one another. The loops denoted via dashed lines indicate the basis function integration points which are actually collocated in space.

3.2 Primal formulation

Arnold *et al.* (2002) explain in detail how to derive the primal formulation from the flux formulation. Inserting our numerical flux and following their procedure (using $\nabla_h V_h \subset \Sigma_h$), we obtain

$$\sum_{E \in \mathcal{T}_{h}} \int_{E} c_{ijrs} \frac{\partial u_{r}}{\partial x_{s}} \frac{\partial v_{i}}{\partial x_{j}} dx + \sum_{e \in \Gamma^{i} \cup \Gamma^{D}} \int_{e} \delta_{e} \llbracket v_{i} \rrbracket \llbracket u_{i} \rrbracket ds - \sum_{e \in \Gamma^{i} \cup \Gamma^{D}} \int_{e} \left(\llbracket u_{i} \rrbracket \Biggl\{ c_{ijrs} \frac{\partial v_{r}}{\partial x_{s}} \right\} + \llbracket v_{i} \rrbracket \Biggl\{ c_{ijrs} \frac{\partial u_{r}}{\partial x_{s}} \right\} \Biggr) n_{j} ds$$

$$= \int_{\Omega} f_{i} v_{i} dx + \sum_{e \in \Gamma^{D}} \int_{e} \delta_{e} v_{i} g_{i}^{D} ds + \sum_{e \in \Gamma^{F}} \int_{e} \delta_{e} \llbracket v_{i} \rrbracket g_{i}^{F} ds - \sum_{e \in \Gamma^{F}} \int_{e} g_{i}^{F} \Biggl\{ c_{ijrs} \frac{\partial v_{r}}{\partial x_{s}} n_{j} \Biggr\} ds - \sum_{e \in \Gamma^{D}} \int_{e} g_{i}^{D} c_{ijrs} \frac{\partial v_{r}}{\partial x_{s}} n_{j} ds . \tag{24}$$

From eq. (24), we collect all terms which are function of both the test and trial function spaces (LHS of eq. 24) into a single bilinear form a(u, v). The linear form, denoted by L(v), collects all terms which are only a function of the test function space (RHS of eq. 24). The variational problem can be then stated as: find $u \in V_h$ which satisfies

$$a(\mathbf{u}, \mathbf{v}) = L(\mathbf{v}), \quad \forall \mathbf{v} \in V_b. \tag{25}$$

Finally, we note that for $\Gamma^F = \emptyset$ and $g_i^D = 0$ the bilinear form $a(\mathbf{u}, \mathbf{v})$ and the linear form $L(\mathbf{v})$ is equivalent to the SIPG scheme for elasticity given by Rivière (2008, chap. 5).

4 DISCONTINUOUS GALERKIN WITH CURVILINEAR COORDINATES AND SUBCELL MATERIAL RESOLUTION

4.1 Overview

Our DG implementation for SEAS starts with partitioning the domain Ω into a set of non-overlapping cells E with boundaries ∂E that conform to the exterior boundary of the domain $(\partial\Omega)$ and the fault interface Γ^F . In Fig. 1(a), we illustrate such a partitioning. Note that we define fault facets by cells E which possess a facet contained in Γ^F (see Fig. 1b). Over the cells and facets, different fields and physical parameters are discretized using nodal DG basis functions. Independent of whether a quantity is defined on a cell or a facet, we always represent the quantity via a degree N polynomial. Over all cells $E \in \mathcal{T}_h$ we discretize the primary unknown displacement u, and the Lamé parameters μ , λ . On all cell facets $e \in \Gamma^F$ (e.g. those facets on the fault), we discretize the state variable ψ , slip S, the background shear traction T^0 and normal stress σ_n^0 and all the other parameters associated with fault friction, such as a, b, V_0 , f_0 and L. An important characteristic of the representation of the aforementioned fields and parameters with a DG basis is that they are discontinuous between adjacent cells (or facets). More precisely, continuity of the fields is not strongly enforced in the definition of the basis functions—rather continuity (or the lack there off) is a result of the numerical DG flux defined on each facet. In Fig. 1(b), we illustrate the nature of the DG basis functions for quantities defined on the cells

$$\widehat{n}^{1} = \begin{pmatrix} -1 \\ 0 \end{pmatrix} \underbrace{\begin{pmatrix} 1 \\ 1 \end{pmatrix}}_{0}$$

$$\widehat{n}^{0} = \begin{pmatrix} 0 \\ -1 \end{pmatrix}$$

Figure 2. Numbering conventions and normals for the reference triangle. Nodes are plotted for N = 5, with N being the polynomial degree.

and along the fault. For example, continuity of the discrete displacement u defined over E_1 is not strongly enforced across the facets shared with E_5 and E_3 . Similarly, the continuity of the discrete slip S defined along e' is not strongly enforced across the common point shared with e''.

Given the spatial dimension D and polynomial degree N, the total number of displacement unknowns in our DG problem is

$$N_h = D \times \dim(\mathcal{T}_h) \times \binom{N+D}{D}. \tag{26}$$

The total number of unknowns associated with a slip vector defined on the fault Γ^F is given by

$$n_h = (D-1) \times \dim(\Gamma^F) \times \binom{N+D-1}{D-1}. \tag{27}$$

The total number of unknowns associated with a scalar field defined over the mesh volume and the fault surface can be obtained by dividing eqs (26) and (27) by the factors D and (D-1), respectively.

4.2 Basis definition

The solution to the variational problem (25) is obtained by solving the linear system of equations Au = b with

$$A_{(kmE)(lnF)} = a \left(\phi_k^F e_m, \phi_l^F e_n \right), \quad b_{(kmE)} = L \left(\phi_k^E e_m \right). \tag{28}$$

Here, functions in the set $\{\phi_k^E e_m\}_{k,m,E}$ are a basis for V_h , where $k=1,\ldots,\binom{N+D}{D}$, $m=1,\ldots,D$, and $E\in\mathcal{T}_h$. The local basis functions ϕ_l^E are non-zero on E and zero otherwise, and $(e_m)_i=\delta_{mi}$. We note that $\underline{\boldsymbol{u}}$ denotes the degrees of freedom of $\boldsymbol{u}\in V_h$. Local degrees of freedom are denoted with superscript E, i.e.that is, $(\underline{\boldsymbol{u}})_{(lnE)}=\underline{\boldsymbol{u}}_{ln}^E$, such that $\underline{\boldsymbol{u}}=\sum_E\phi_l^Ee_n\underline{\boldsymbol{u}}_{ln}^E$ with components $u_i=\sum_E\phi_l^E\underline{\boldsymbol{u}}_{li}^E$.

Strategies to solve $A\underline{u} = b$ may require the explicit assembly of the non-zero entities of the matrix A, or they may use the so-called matrix-free approach, in which one implements the action of A on the degrees of freedom \underline{u} , that is,

$$(A\underline{\boldsymbol{u}})_{(kmE)} = \sum_{F} a \left(\phi_{k}^{E} \boldsymbol{e}_{m}, \phi_{l}^{F} \boldsymbol{e}_{n} \right) \underline{\boldsymbol{u}}_{ln}^{F}$$

$$= a \left(\phi_{k}^{E} \boldsymbol{e}_{m}, \sum_{F} \phi_{l}^{F} \boldsymbol{e}_{n} \underline{\boldsymbol{u}}_{ln}^{F} \right) = a \left(\phi_{k}^{E} \boldsymbol{e}_{m}, \boldsymbol{\boldsymbol{u}} \right). \tag{29}$$

In either case, machinery to evaluate volume and surface integrals on the reference element is required, and we detail the necessary tools to implement the DG scheme on unstructured curvilinear meshes in Section 4.3.

4.3 Computations on the reference element

We assume that a map from the reference element \hat{E} to a physical element E is expressed via the following nodal basis expansion:

$$X_{E}(\xi) = \sum_{j} \phi_{j}(\xi) \underline{X}_{j}^{E}. \tag{30}$$

The defining property of nodal basis functions is $\phi_j(\xi_i) = \delta_{ij}$, with Kronecker delta δ_{ij} and nodes $\xi_1, \dots, \xi_{B_N} \in \widehat{E}$, where $B_N = \binom{N+D}{D}$. We use the warp and blend nodes in this paper as they have a small Lebesgue constant and are easy to construct on the triangle and the tetrahedron (Warburton 2006). The warp and blend nodes are illustrated in Figs 2 and 3.

The points $\underline{X}_j^E \in \mathbb{R}^D$ give the location of a node in the domain, as $X_E(\xi_j) = \underline{X}_j^E$. In practice, these can be obtained in at least two ways: either, one generates a simplex mesh and applies a warp function to each node, such that X_E is an interpolant of the warp function. Or, one can use high-order meshing software, for example, the open-source software Gmsh (Geuzaine & Remacle 2009; Johnen *et al.* 2013).

$$\widehat{\boldsymbol{n}}^{2} = \begin{pmatrix} -1 \\ 0 \\ 0 \end{pmatrix} \qquad \widehat{\boldsymbol{n}}^{3} = \begin{pmatrix} 1 \\ 1 \\ 1 \end{pmatrix}$$

$$\widehat{\boldsymbol{n}}^{1} = \begin{pmatrix} 0 \\ -1 \\ 0 \end{pmatrix} \qquad 0 \qquad 1$$

$$\widehat{\boldsymbol{n}}^{0} = \begin{pmatrix} 0 \\ 0 \\ 0 \\ -1 \end{pmatrix} \qquad \widehat{\boldsymbol{t}}^{1}$$

Figure 3. Numbering conventions and normals for the reference tetrahedron. Nodes are plotted for N=5.

Volume integrals over the physical element $E = X_E(\widehat{E})$ can be computed using quadrature rules (Witherden & Vincent 2015; Jaśkowiec & Sukumar 2020). For example, the integral of $u \in V_h$ is computed with

$$\int_{E} u_{p}(\mathbf{x}) \, \mathrm{d}\mathbf{x} = \int_{\widehat{E}} \underline{u}_{ip}^{E} \phi_{i}(\boldsymbol{\xi}) J^{E}(\boldsymbol{\xi}) \, \mathrm{d}\boldsymbol{\xi}$$

$$\approx \sum_{q} W_{q} \underline{u}_{ip}^{E} \phi_{i}(\widehat{\boldsymbol{\xi}}_{q}) J^{E}(\widehat{\boldsymbol{\xi}}_{q}), \tag{31}$$

where we use the nodal basis expansion $u_p|_E \circ X_E = \underline{u}_{ip}^E \phi_i(\xi)$, W_q and $\widehat{\xi}_q$ are quadrature weights and abscissa for \widehat{E} , and

$$J^{E}(\boldsymbol{\xi}) = |\det(\nabla X_{E}(\boldsymbol{\xi}))|. \tag{32}$$

For the surface integral's parametrization, we introduce the maps $\Upsilon_E^f: \widehat{e} \to \widehat{E}$ from the reference facet \widehat{e} (i.e. reference edge in 2-D and reference triangle in 3-D) to the reference element \widehat{E} , given by

$$\mathbf{\Upsilon}^{f}(\mathbf{\chi}) = \left(1 - \sum_{i=1}^{D-1} \chi_{i}\right) \boldsymbol{\xi}_{0}^{f} + \sum_{i=1}^{D-1} \chi_{i} \boldsymbol{\xi}_{i}^{f}, \tag{33}$$

where $\xi_0^f, \dots, \xi_{D-1}^f$ are the vertices of the reference simplex that make up the fth facet $(f = 0, \dots, D)$.

Surface integrals in DG involve information of the two simplices E_1 and E_2 adjoining the facet $e = \partial E_1 \cap \partial E_2$. Let f, g be the local face number of e in E_1, E_2 , respectively, and Υ^g the respective facet maps. The parametrization is greatly simplified by ensuring consistent local edge directions. For triangle or tetrahedral meshes, one can show that local edge directions are always consistent when the local vertex order is chosen according to a global vertex order (Rognes et al. 2009). In this case, we have

$$\forall \chi \in \widehat{e}: X_{E_1} \circ \Upsilon^f = X_{E_2} \circ \Upsilon^g. \tag{34}$$

For example, for $u, v \in V_h$ we have

$$\int_{e} u_{p}|_{E_{1}} v_{p}|_{E_{2}} ds = \int_{\widehat{e}} u_{ip}^{E_{1}} \phi_{i}(\mathbf{\Upsilon}^{f}(\mathbf{\chi})) \underline{v}_{jp}^{E_{2}} \phi_{j}(\mathbf{\Upsilon}^{g}(\mathbf{\chi})) |\mathbf{n}^{e}(\mathbf{\chi})| d\mathbf{\chi}$$

$$\approx \sum_{q} w_{q} \underline{u}_{ip}^{E_{1}} \phi_{i}(\mathbf{\Upsilon}^{f}(\widehat{\mathbf{\chi}}_{q})) \underline{v}_{jp}^{E_{2}} \phi_{j}(\mathbf{\Upsilon}^{g}(\widehat{\mathbf{\chi}}_{q})) |\mathbf{n}^{e}(\widehat{\mathbf{\chi}}_{q})|, \tag{35}$$

where we have used the nodal basis expansions $u_p|_{E_1} \circ X_{E_1} = \underline{u}_{ip}^{E_1} \phi_i(\xi)$ and $v_p|_{E_2} \circ X_{E_2} = \underline{v}_{ip}^{E_2} \phi_i(\xi)$. Quadrature weights and abscissa for \widehat{e} are given by w_q and $\widehat{\chi}_q$ (Witherden & Vincent 2015) and

$$\boldsymbol{n}^{e}(\boldsymbol{\chi}) = J^{E_1}(\boldsymbol{\Upsilon}^{f}(\boldsymbol{\chi})) \left(\nabla X_{E_1}(\boldsymbol{\Upsilon}^{f}(\boldsymbol{\chi})) \right)^{-T} \widehat{\boldsymbol{n}}^{f}, \tag{36}$$

where \hat{n}^f are the outward pointing normals of the reference simplex (see Figs 2 and 3). We remark that the absolute value of the determinant of the face Jacobian is taken in eq. (36), because the determinant might be negative as a consequence of the numbering convention (e.g. in 2-D the vertices might be ordered both clockwise and counter-clockwise.) The same reasoning also holds for the cell Jacobian in eq. (32).

4.4 Trace spaces

The mapping $\mathbf{m}_e : \widehat{e} \to e$ from the reference facet \widehat{e} to $e \in \Gamma^F$ is given by

$$\boldsymbol{m}_{e}(\boldsymbol{\chi}) = \boldsymbol{X}_{E_{1}^{e}} \circ \boldsymbol{\Upsilon}^{f_{1}^{e}} = \boldsymbol{X}_{E_{2}^{e}} \circ \boldsymbol{\Upsilon}^{f_{2}^{e}}. \tag{37}$$

Quantities (T, S, ψ) on the physical element are related to quantities $(\widehat{T}, \widehat{S}, \widehat{\psi})$ on the reference element via

$$T = \widehat{T} \circ \mathbf{m}_{e}^{-1}, \quad S = \widehat{S} \circ \mathbf{m}_{e}^{-1}, \quad \psi = \widehat{\psi} \circ \mathbf{m}_{e}^{-1}. \tag{38}$$

To discretize fields and parameters on the the fault, we use the following finite element spaces

$$M_h^d = \left\{ \boldsymbol{\mu} \in \left[L^2(\Gamma^F) \right]^d : \widehat{\boldsymbol{\mu}}|_e \in [P_N(\widehat{e})]^d \ \forall e \in \Gamma^F \right\}$$
 (39)

for $T, S \in M_h^{D-1}$ and $\psi \in M_h^1$.

4.5 Residual evaluation and matrix-free implementation

We first eliminate the derivative in eq. (19) through integration by parts:

$$\int_{E} \tau_{ij} \sigma_{ij} \, \mathrm{d}\mathbf{x} = \int_{E} \tau_{ij} c_{ijrs} \frac{\partial u_r}{\partial x_s} \, \mathrm{d}\mathbf{x} + \int_{\partial E} \tau_{ij} c_{ijrs} (\widetilde{u}_r - u_r) n_s \, \mathrm{d}s \,. \tag{40}$$

We set $\tau_{ij} = \partial v_i / \partial x_j$ in eq. (40), which is valid due to $\nabla_h V_h \subset \Sigma_h$. The result is plugged into eq. (20):

$$\int_{E} \frac{\partial v_{i}}{\partial x_{j}} c_{ijrs} \frac{\partial u_{r}}{\partial x_{s}} d\mathbf{x} + \int_{\partial E} \frac{\partial v_{i}}{\partial x_{j}} c_{ijrs} (\widetilde{u}_{r} - u_{r}) n_{s} ds - \int_{\partial E} v_{i} \widetilde{\sigma}_{ij} n_{j} ds = \int_{E} f_{i} v_{i} d\mathbf{x}.$$

$$(41)$$

The computation of the numerical flux on $e = \partial E_1^e \cap \partial E_2^e$ is described next. Recall the basis expansion $\mathbf{u} = \sum_E \phi_l^E \mathbf{e}_n \underline{u}_{ln}^E$, where ϕ_l^E is only non-zero on E. If $e \in \Gamma^0$ we have for $\mathbf{x} \in e$

$$\widetilde{\sigma}_{ij}^{e}(\mathbf{x}) = \left\{ \left\{ c_{ijrs} \frac{\partial u_{r}}{\partial x_{s}} \right\} - \delta_{e} \left[\left[u_{i} \right] \right] n_{j} \right. \\
= \frac{1}{2} c_{ijrs}^{E_{l}^{e}} \frac{\partial \phi_{l}^{E_{l}^{e}}}{\partial x_{s}} \underbrace{u_{lr}^{E_{l}^{e}} + \frac{1}{2} c_{ijrs}^{E_{l}^{e}}}_{\partial x_{s}} \underbrace{u_{lr}^{E_{l}^{e}} - \delta_{e} \left(\underbrace{u_{li}^{E_{l}^{e}} \phi_{l}^{E_{l}^{e}} - u_{li}^{E_{l}^{e}} \phi_{l}^{E_{l}^{e}} \right)}_{\partial x_{s}} n_{j}. \tag{42}$$

For $x \in E$, the basis functions are given by $\phi_l^E = \phi_l \circ X_E^{-1}$. Using the chain rule we obtain (Brezzi & Fortin 1991,III.1.3)

$$\nabla \phi_k^E = \left(\nabla \phi_l \circ X_F^{-1}\right) \nabla X_F^{-1} = \left(\nabla \phi_l (\nabla X_E)^{-1}\right) \circ X_F^{-1}. \tag{43}$$

Moreover, we introduce the shorthand notation

$$G_{ej}^{E}(\boldsymbol{\xi}) = (\nabla X_{E}(\boldsymbol{\xi}))_{ej}^{-1}, D_{ke}(\boldsymbol{\xi}) = \frac{\partial \phi_{k}(\boldsymbol{\xi})}{\partial \xi_{e}},$$

$$G_{ej}^{E,f}(\boldsymbol{\chi}) = G_{ej}^{E}(\boldsymbol{\Upsilon}^{f}(\boldsymbol{\chi})), D_{ke}^{f}(\boldsymbol{\chi}) = D_{ke}(\boldsymbol{\Upsilon}^{f}(\boldsymbol{\chi})),$$

$$\phi_{k}^{f}(\boldsymbol{\chi}) = \phi_{k}(\boldsymbol{\Upsilon}^{f}(\boldsymbol{\chi})),$$

$$(44)$$

where f = 0, ..., D is the local facet number. Let f_1^e and f_2^e be the local facet numbers for e of elements E_1^e and E_2^e , respectively. Hence, we get on the reference facet

$$\widetilde{\sigma}_{ij}^{e}(\mathbf{\chi}) = \frac{1}{2} c_{ijrs}^{E_{l}^{e}} D_{le}^{f_{l}^{e}} G_{es}^{E_{l}^{e}, f_{l}^{e}} \underline{u}_{lr}^{E_{l}^{e}} + \frac{1}{2} c_{ijrs}^{E_{2}^{e}} D_{le}^{f_{2}^{e}} G_{es}^{E_{2}^{e}, f_{2}^{e}} \underline{u}_{lr}^{E_{2}^{e}} - \delta_{e} \left(\underline{u}_{li}^{E_{l}^{e}} \phi_{l}^{f_{l}^{e}} - \underline{u}_{li}^{E_{2}^{e}} \phi_{l}^{f_{2}^{e}} \right) n_{j}^{e}.$$

$$(45)$$

Likewise, the displacement flux on the reference facet is

$$\widetilde{u}_{i}^{e}(\mathbf{\chi}) = \{u_{i}\} = \frac{1}{2} \left(\underline{u}_{li}^{E_{i}^{e}} \phi_{l}^{f_{i}^{e}} + \underline{u}_{li}^{E_{i}^{e}} \phi_{l}^{f_{i}^{e}} \right). \tag{46}$$

The numerical fluxes on the fault, Dirichlet, or Neumann boundaries are derived similarly. We only note that on $e \in \Gamma^F$ the flux is double valued with $\widetilde{u}_i|_{E_i^e} = \{u_i\} + g_i^F/2$ and $\widetilde{u}_i|_{E_i^e} = \{u_i\} - g_i^F/2$.

Next, we recover an expression for the residual $\mathbf{r} := A\underline{\mathbf{u}} - \mathbf{b}$. In eq. (41), we move the force term to the left-hand side and plug in the basis expansion and the test function $\mathbf{v} = \mathbf{e}_u \phi_k^E$:

$$r_{(kuE)} = \underline{u}_{lr}^{E} \int_{E} \frac{\partial \phi_{k}^{E}}{\partial x_{j}} c_{ujrs} \frac{\partial \phi_{l}^{E}}{\partial x_{s}} d\mathbf{x} + \sum_{e \in \partial E} \int_{e} \frac{\partial \phi_{k}^{E}}{\partial x_{j}} c_{ujrs} \left(\widetilde{u}_{r}^{e} - \underline{u}_{lr}^{E} \phi_{l}^{E} \right) n_{s} ds - \sum_{e \in \partial E} \int_{e} \phi_{k}^{E} \widetilde{\sigma}_{uj}^{e} n_{j} ds - \int_{E} \phi_{k}^{E} \widetilde{\sigma}_{u}^{e} n_{j} ds .$$

$$(47)$$

With the tools developed in Section 4.3 we map eq. (47) to the reference element:

$$r_{(kuE)} = \underline{u}_{lr}^{E} \int_{\widehat{E}} D_{ke} G_{ej}^{E} c_{ujrs} D_{lf} G_{fs}^{E} J^{E} d\xi$$

$$+ \sum_{f=0}^{D} \int_{\widehat{e}} D_{ke}^{f} G_{ej}^{E,f} c_{ujrs} \left(\widetilde{u}_{r}^{ef} - \underline{u}_{lr}^{E} \phi_{l}^{f} \right) n_{s}^{ef} d\chi$$

$$- \sum_{f=0}^{D} \int_{\widehat{e}} \phi_{k}^{f} \widetilde{\sigma}_{uj}^{ef} n_{j}^{ef} d\chi - \int_{\widehat{E}} \phi_{k} f_{u} J^{E} d\xi , \qquad (48)$$

where e_f is the fth facet of E. Finally, we introduce the convention that an additional index q means evaluation at $\widehat{\boldsymbol{\xi}}_q$ or $\widehat{\boldsymbol{\chi}}_q$, for example, $G_{ejq}^E := G_{ej}^E(\widehat{\boldsymbol{\xi}}_q)$ or $n_{iq}^e := n_i^e(\widehat{\boldsymbol{\chi}}_q)$. The fully discrete form is

$$r_{(kuE)} \approx \sum_{q} W_{q} \underline{u}_{lr}^{E} D_{keq} G_{ejq}^{E} c_{ujrsq} D_{lfq} G_{fsq}^{E} J_{q}^{E}$$

$$+ \sum_{f} \sum_{q} w_{q} D_{keq}^{f} G_{ejq}^{E,f} c_{ujrsq} \left(\widetilde{u}_{rq}^{ef} - \underline{u}_{lr}^{E} \phi_{lq}^{f} \right) n_{sq}^{ef}$$

$$- \sum_{f} \sum_{q} w_{q} \phi_{kq}^{f} \widetilde{\sigma}_{ujq}^{ef} n_{jq}^{ef} - \sum_{q} W_{q} \phi_{kq} f_{uq} J_{q}^{E}.$$

$$(49)$$

The action $A\underline{u}$ is readily obtained by setting $g_i^D = 0$, $g_i^F = 0$, and $f_i = 0$ in the residual r. That is, the action $A\underline{u}$ is obtained by setting all terms which would appear in b (in the discrete problem), or in L(v) (in the continuous problem), to zero.

4.6 Linear solvers

There are many direct and iterative methods to find the solution of the sparse linear system $A\underline{u} = b$. We gain access to many of these methods by using the PETSc, which provides high-level data structures for distributed matrices and vectors and a unified interface to many Krylov methods, pre-conditioners and sparse direct solvers (Balay *et al.* 1997, 2021a, b).

In this paper, we use two different kinds of solvers, LU factorization and Krylov methods pre-conditioned with multigrid. LU factorization is a good choice for small-scale problems, in particular in 2-D. For SEAS problems we consider, the operator *A* is independent of time, such that the expensive factorization step is only required once. PETSc provides an interface to many state-of-the-art LU factorization packages (Balay *et al.* 2021a). In this work, when we resort to using LU, we used the sparse direct solver MUMPS (Amestoy *et al.* 2001, 2019).

For large problems, in particular in 3-D, iterative methods are used with a pre-conditioner that combines the p-multigrid and the algebraic multigrid methods. We define a sequence of coarse to fine grids $V_h^{p_1} \subset \cdots \subset V_h^{p_L}$ for the p-multigrid method, where $p_1 = 1 < \cdots \le p_L = N$. The spaces $V_h^{p_i}$ are obtained by replacing N with p_i in eq. (18). As the spaces are nested and the same mesh is used, the interpolation operator I_i^{i+1} for the transfer of the residual from grid i to grid i+1 is simply a block diagonal matrix. Following the Galerkin approach, the restriction operator is set to $I_{i+1}^i = (I_i^{i+1})^T$ and the coarse grid operators are given by $A^i = I_{i+1}^i A^{i+1} I_i^{i+1}$. On the coarsest grid, we apply the algebraic multigrid pre-conditioner GAMG (Balay *et al.* 2021a).

4.7 Implementation details

Our C++-implementation of the DG scheme is freely available under the BSD 3-Clause license (https://github.com/TEAR-ERC/tandem).

Tandem supports matrix assembly as well as the matrix-free approach. The matrix-free computation of the residual or operator application $A\underline{u}$ consists solely of small tensor contractions. We use Yet Another Tensor Toolbox (Uphoff & Bader 2020) to generate high-performance kernels for eq. (49).

Tandem is inherently parallel and designed for large-scale distributed memory architectures. In addition to PETSc for parallel linear algebra, solvers and pre-conditioner support, we also employ the graph partitioning libraries Metis and Parmetis (Karypis & Kumar 1998) to facilitate run-time mesh partitioning for a given MPI communicator size.

Tandem natively loads meshes generated with Gmsh in parallel. Once loaded, a new mesh decomposition (load balanced partition) is defined using Parmetis. Given the new partition, the elements and all associated attributes (e.g. cell tags/labels, vertex coordinates, vertex tags/labels) are scattered to the appropriate MPI rank. In this paper, all meshes were created using Gmsh version 4.8.4 (Geuzaine & Remacle 2009; Johnen *et al.* 2013).

In principle, given a DG function space of degree N, the error is expected to decrease with $\mathcal{O}(h^N)$, where h is the maximum element diameter. In order to retain the desirable convergence behaviour in domains with curved boundary or heterogeneous material parameters, we approximate the geometry and material parameters with polynomials of the same maximum degree N as the displacement.

5 COUPLING AND TIME STEPPING

We complete the numerical scheme for SEAS model with the following three steps. First, we discuss the coupling between on- and off-fault variables. Second, we show how eqs (14) and (13) can be recast as an ordinary system of differential equations. Lastly, we discuss the time integrator used to advance the numerical solution forward in time.

5.1 Coupling

The change in traction δT_i given by

$$\delta T_i = T_i - T_i^0 = B_{ji} \sigma_{jk}(\mathbf{u}) n_k, \tag{50}$$

couples the elasticity solver to the friction law, but σ_{jk} is double-valued on Γ^F . Thus, we replace with σ_{jk} with the numerical flux $\widetilde{\sigma}_{jk}$ (see eq. 23a), because the flux is single-valued and is designed to be a (stable) approximation of σ_{jk} on Γ^F . Moreover, $(\boldsymbol{B}^T \widetilde{\boldsymbol{\sigma}} \boldsymbol{n})|_{\Gamma^F} \notin M_h^{D-1}$ for non-affine mappings. Hence, we define the projection operator $\pi_e^d : [L^2(\Gamma^F)]^d \to M_h^d$ defined by

$$\int_{a} \boldsymbol{\mu} \cdot \boldsymbol{\pi}_{e}(\boldsymbol{\theta}) \, \mathrm{d}s = \int_{a} \boldsymbol{\mu} \cdot \boldsymbol{\theta} \, \mathrm{d}s \,, \quad \forall \, \boldsymbol{\mu} \in M_{h}^{d}. \tag{51}$$

In our implementation, we define the change in traction in eq. (50) via $\delta T|_e = \pi_e^{D-1}(B^T \widetilde{\sigma} n)$. Specifically, we represent the change in traction using the nodal basis $\varphi_i(\chi)$ on the reference face \widehat{e} . That is, with $\delta T_i|_e \circ m_e = \sum_l \underline{\delta T_{li}^e} \varphi_l$ we have

$$\underline{\delta T_{li}^e} \int_{\widehat{\mathcal{F}}} \varphi_k \varphi_l |\mathbf{n}^e| \, \mathrm{d}\mathbf{\chi} = \int_{\widehat{\mathcal{F}}} \varphi_k B_{ji}^e \widetilde{\sigma}_{ij}^e n_j^e \, \mathrm{d}\mathbf{\chi} \,. \tag{52}$$

Similarly, we also have to project the terms within the normal stress (eq. 11) yielding

$$\sigma_n|_e = \max\left(0, \pi_e^1\left(\sigma_n^0\right) - \pi_e^1(n\tilde{\boldsymbol{\sigma}}\boldsymbol{n})\right). \tag{53}$$

Fault slip and state are represented as polynomials on element faces (see Section 4.4). These polynomials are defined using a nodal basis expansion. We note that in practice we do not need to distinguish between the polynomial and the solution on each node because we can obtain one from the other in an unique manner. Slip is set as boundary condition in the elasticity solver, for example, eq. (14). Using the nodal basis expansion $\widehat{S}_j = \sum_l \underline{S}_{lj}^e \varphi_l(\chi)$ we simply set $g_i^F|_{e} \circ \mathbf{m}_e = B_{ij}^e \underline{S}_{lj}^e \varphi_l$.

We note that in an early stage of developing the numerical scheme we defined on-fault traction as $\{c_{ijkl} \ \partial u_k / \partial x_l \} n_j$ instead of $\widetilde{\sigma}_{ij} n_j$. We found that this choice is unstable, that is, the on-fault traction might become discontinuous along the fault and grow without bounds.

5.2 Ordinary differential equations

The boundary conditions associated with the Dirichlet constraints (g_i^D) and fault constraints (g_i^F) only appear in the right-hand side L(v) (see eq. 24). g_i^F is an explicit function of slip (i.e. eq. 14), and in order to permit time-dependent loading we assume that $g_i^D = g_i^D(t)$. Noting that the bilinear form $a(\cdot, \cdot)$ is both independent of slip and time, the slip S and time t dependence within the discrete elasticity problem is given by

$$A\underline{u} = b, \quad b = b(\underline{S}, t). \tag{54}$$

The above problem has a unique solution for a large enough penalty (see Section A) formally given by $\underline{u} = A^{-1}b(\underline{S}, t)$. The change δT in traction depends linearly on \underline{u} (Section 5.1), thus traction T is a function of time and slip.

Slip rate, state and traction are linked via the friction law. Taking the magnitude T = |T| reduces eq. (12) to the following scalar equation

$$\sigma_n F(V, \psi) + \eta V - T = 0, \tag{55}$$

where V = |V|. The derivative of eq. (55) with respect to V is $\sigma_n \frac{\partial F}{\partial V} + \eta$, where for the particular choice of F from eq. (6) we have $\partial F/\partial V > 0$ for a > 0 and $V_0 > 0$. With $\eta \ge 0$ it follows from the implicit function theorem that there exists a unique function $V(\psi, T, \sigma_n)$ that solves eq. (55). It follows that V is a function of ψ , T, σ_n .

In practice, the solution to eq. (55) is found using standard root-finding methods such as Brent's method (Forsythe *et al.* 1977). Note that the root lies in the interval $V \in [0, T/\eta]$.

So far we silently ignored that S, ψ depend on time. With abuse of notation we understand that for fixed time t we have $S(t) \in M_h^{D-1}$ and $\psi(t) \in M_h^1$. That is, we solve for the slip and state at each fault basis function associated with every facet $e \in \Gamma^F$ (e.g. see open red squares in Fig. 1b) yielding the semi-discrete quasi-dynamic model

$$\frac{\mathrm{d}\underline{S}}{\mathrm{d}t} = \underline{\delta}\underline{S}(\underline{\psi}, \underline{S}, t),
\frac{\mathrm{d}\underline{\psi}}{\mathrm{d}t} = \underline{\delta}\underline{\psi}(\underline{\psi}, \underline{S}, t), \tag{56}$$

where the definition of the right-hand side terms $\underline{\delta S}$ and $\underline{\delta \psi}$ are provided in Algorithm 1 (lines 18–19). In Algorithm 1, we note that the quantities $\underline{\delta T}^e$ (line 3) and $(\delta \sigma_n)^e$ (line 6) can be computed on-the-fly for each element $e \in \Gamma^F$.

Algorithm 1 Evaluation of right-hand side of quasi-dynamic model in Eq. (56)

```
Require: Degrees of freedom \psi, \underline{S} at time t and \underline{T}^0, \sigma_n^0
Ensure: Computes \delta S and \delta \psi
 1: Solve Au = b(S,t)
 2: for e \in \Gamma^F do
                                                                                                                                                                             > For every fault facet
           Compute \delta T^e using Eq.(52)
 3:
                                                                                                                                               \triangleright (T^0)^e is obtained via \pi_e^{D-1}(\cdot) as per \delta T^e
            T^e \leftarrow (T^0)^e + \delta T^e
 4:
                                                                                                                                                                                         ⊳ See Eq.(53)
 5:
           Compute (\delta \sigma_n)^e by projecting n \tilde{\sigma} n
           (\underline{\sigma_n})^e \leftarrow \max \left(0, (\sigma_n^0)^e - (\underline{\delta \sigma_n})^e\right)
                                                                                                                                                                    (\sigma_n^0)^e is obtained via \pi_e^1(\cdot)
 6:
           for k=1,\ldots,\binom{N+D-1}{D-1} do
 7:
                                                                                                                                                                     \triangleright For every fault basis on e
                                                                                                                                                                   8:
                 T \leftarrow |\boldsymbol{T}|
 9.
                 \sigma_n \leftarrow (\sigma_n)_k^e
                                                                                                                                                           > Extract facet basis normal stress
10:
                 if T \neq 0 then

⊳ Solve for non-zero slip-rate

11:
                      Let R(V) = \sigma_n F(V, \psi_i^e) + \eta V - T
12.
                      Solve R(V) = 0 using Brent's method
13:
                      V \leftarrow -(V/T)T
14:
15:
                 else
                                                                                                                                                                         V \leftarrow 0
16:
                 end if
17:
                \frac{\delta S_{ki}^e}{\delta \psi_k^e} \leftarrow V_i \text{ for } i = 1, \dots, D - 1\frac{\delta \psi_k^e}{\delta \psi_k^e} \leftarrow G(|V|, \psi_k^e)

    □ Update slip increment

18:
19:

    □ Update state increment

20:
21: end for
```

5.3 Time stepping

Eq. (56) is the canonical formulation of a system of ODEs. Hence, time stepping is handled by the software library PETSc/TS (Abhyankar *et al.* 2018). Experiments in this paper use explicit Runge–Kutta schemes with adaptive time step control.

6 DISCRETE GREEN'S FUNCTION

The most expensive part in Algorithm 1 is the solution of the discrete elasticity problem in Line 1. Given that SEAS problems typically require hundreds of thousands of time steps, we may need to solve the discrete elasticity problem millions of times, one solve per Runge–Kutta stage. Moreover, we solve for displacement in a D-dimensional domain whereas only the on-fault traction on (D-1)-dimensional surfaces is required to evolve rate and state friction. In the following, we denote the number of displacement components in the volume by N_h (see eq. 26), and the number of slip components on the fault by n_h (see eq. 27). We can optionally combine the volumetric SIPG method with the discrete Green's functions approach which builds the basis of BEM. Complex Green's functions have been evaluated numerically for applications in geodesy (e.g. Hori *et al.* 2021) and seismology (e.g. van Driel *et al.* 2015).

By inspecting the linear form L(v) in eq. (25), and assuming zero body forces as well as a linear in time Dirichlet boundary condition, we can split up the discrete right-hand side as

$$b(\underline{S},t) = tb_D + Z_1\underline{S},\tag{57}$$

where the size of \boldsymbol{b} and \boldsymbol{b}_D is N_h , the size of $\underline{\boldsymbol{S}}$ is n_h , and \boldsymbol{Z}_1 is a $N_h \times n_h$ matrix. Moreover, the linear relation between change in traction and displacement is written as

$$\delta T = Z_2 u, \tag{58}$$

where \mathbf{Z}_2 is a $n_h \times N_h$ matrix. With $\underline{\mathbf{S}} = \underline{S}_i \mathbf{e}_i$, $(\mathbf{e}_i)_j = \delta_{ij}$, we obtain

$$\underline{\delta T} = t \underbrace{Z_2 A^{-1} b_D}_{=:g_D} + \sum_{i=1}^{n_h} \underbrace{Z_2 A^{-1} Z_1 e_i}_{=:g_i} \underline{S_i}. \tag{59}$$

Therefore, instead of solving a linear system the change in traction can be written in terms of the discrete Green's function g_D , g_1 , ..., g_{n_h} . We note that our assumption of a linear in time Dirichlet boundary condition is not unique but allows us to define simple time-dependent loading conditions as used in many reference problems. It is also computationally cheap, since our parametrization allows the Dirichlet data to be described by a single discrete Green's function. More general parametrizations of the Dirichlet data would require to solve for as many discrete Green's functions as the total number of finite-element coefficients associated with the Dirichlet boundary.

The matrices A^{-1} , Z_1 , Z_2 are not required explicitly. Instead, we only need to compute the change in traction for the right-hand sides b(0, 1) and $b(e_i, 0)$, $i = 1, ..., n_h$, in order to obtain the discrete Green's function. We also note that the action of $A^{-1}y$ (for an arbitrary vector y) is defined via a solve. As an example we consider the first term on the right-hand side of eq. (59). This would be evaluated as tZ_2u^* where u^* is the solution to $Au^* = b_D$. The solution strategies employed in Section 4.6 are also adopted for obtaining the auxiliary solutions required to define the discrete Green's function. Since the operator A is sparse and we have both optimal and parallel efficient solvers for this operator, we thus also have a highly scalable means to compute all of the required Green's functions. The importance of this will be further elaborated upon in Section 9.2.

7 VERIFICATION

The presented SIPG method allows to model the slip boundary condition, curved boundaries, heterogeneous material parameters and can be coupled to rate and state friction laws. In this section, we discuss and analyse various 2-D and 3-D model problems whereby each verifies one or multiple of these method capabilities.

First, we discuss static elasticity problems which verify that the SIPG method converges. An analytic solution is available for each of these problems, hence we determine the empirical convergence order and discuss the benefits and limitations of using a high-order method.

Second, we use the method of manufactured solutions to analyse whether convergence is achieved for an SEAS problem with a modified state equation. In the method of manufactured solutions, the modeller chooses the evolution of slip and state. The modeller then adds source terms to the SEAS equations such that slip and state are the solution to the modified SEAS problem. Therefore, the analytic solution is available and the convergence behaviour of the method can be discussed (e.g. Erickson *et al.* 2017).

Last, we verify the method in a community benchmark problem (Erickson *et al.* 2020). While this problems resembles an actual SEAS model, no analytic solution is available, but we obtain a comparison to several independent methods and implementations.

We note that input files to reproduce all setups are openly available (see Data Availability).

7.1 Convergence of the elasticity solver

We analyse the convergence behaviour of the SIPG scheme for elastostatic problems. In our chosen verification problems we cover 2-D and 3-D curvilinear meshes with heterogeneous material parameters as well as the slip boundary condition.

Errors in the displacement are measured with the norm

$$\|\mathbf{u}\|_{0,h} = \left(\sum_{E \in \mathcal{T}_L} \int_E u_i u_i \, \mathrm{d}\mathbf{x}\right)^{1/2}.$$
 (60)

When coupling the elasticity solver to the nonlinear rate and state friction law we additionally require accurate gradients of the displacement. Therefore, we also measure the error in the semi-norm

$$|\mathbf{u}|_{1,h} = \left(\sum_{E \in \mathcal{T}_h} \int_E \frac{\partial u_i}{\partial x_j} \frac{\partial u_i}{\partial x_j} \, \mathrm{d}\mathbf{x}\right)^{1/2}.$$
 (61)

Given a sequence of meshes with mesh sizes $h_1 > \ldots > h_n$, respective discrete solutions u_1, \ldots, u_n , and the analytical solution u^* , the empirical convergence order is defined as

$$C_i = \frac{\log(E_{i-1}/E_i)}{\log(h_{i-1}/h_i)},\tag{62}$$

where the error E_i is either given by the L_2 norm $\|\mathbf{u}_i - \mathbf{u}^*\|_{0,h}$, or the H_1 semi-norm $\|\mathbf{u}_i - \mathbf{u}^*\|_{1,h}$.

7.1.1 Slip boundary condition

In the first 2-D verification setup, the slip boundary condition is evaluated. Our approach in constructing the test problem is to find solutions to the elasticity equation on wedge-shaped domains and then glue two wedge-shaped domains together, separated by a dipping fault.

Let a semi-infinite wedge be given by $\Omega^{\theta_1,\theta_2} = \{(x,y) \in \mathbb{R}^2 : \theta_1 < \theta(x,y) < \theta_2\}$, where $\theta \in [-\pi,\pi)$ is the polar angle, that is, $x = r\cos(\theta)$ and $y = r\sin(\theta)$. Then we can construct a dipping fault by gluing domains $\Omega^A := \Omega^{-\pi,\omega}$ and $\Omega^B := \Omega^{\omega,0}$, where the dip angle $\omega \in (-\pi,0)$. Here, we set $\omega = -\pi/3$, as illustrated in Fig. 4(a). For our test problem we require the following boundary conditions to be satisfied:

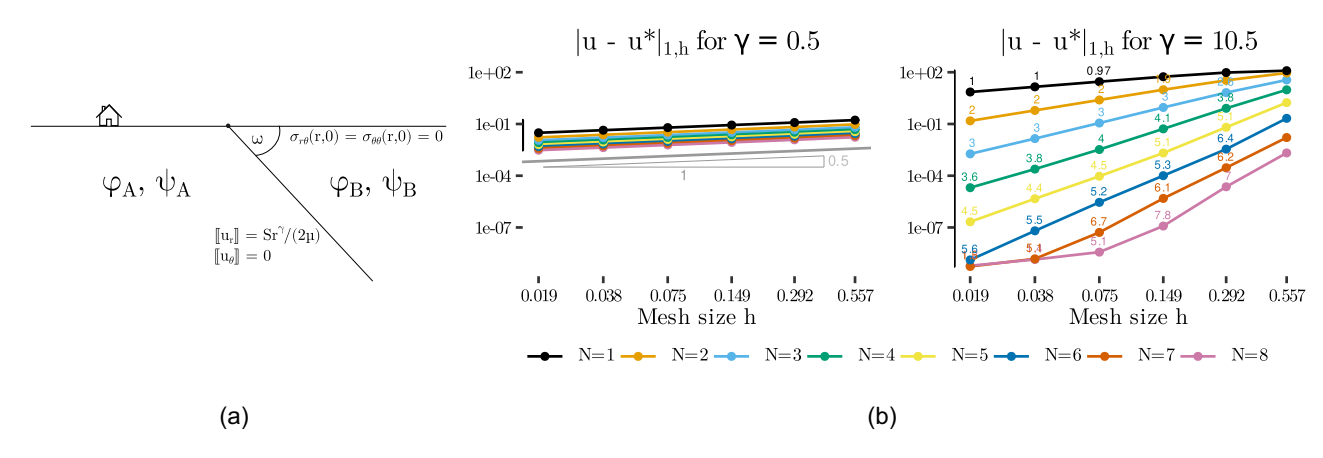


Figure 4. Setup and numerical results for a dipping fault scenario which verifies the slip boundary condition. (a) Model geometry and setup. (b) Error versus mesh size for a solution with poor regularity (left) and a smooth solution (right). Our results agree well with the theoretical predictions, that is, an empirical convergence order smaller than 1 for $\gamma = 0.5$ and empirical convergence orders close to N for $\gamma = 10.5$ (see the small text above points), with N being the polynomial degree and γ a solution smoothness parameter. The minimum attainable error is limited due to finite precision and conditioning of the linear system.

$$\sigma_{r\theta}^{A}|_{\theta=-\pi} = \sigma_{\theta\theta}^{A}|_{\theta=-\pi} = 0,
\sigma_{r\theta}^{B}|_{\theta=0} = \sigma_{\theta\theta}^{B}|_{\theta=0} = 0 \text{ (free surface)},
\llbracket \sigma_{\theta\theta} \rrbracket = \sigma_{\theta\theta}^{A}|_{\theta=\omega} - \sigma_{\theta\theta}^{B}|_{\theta=\omega} = 0,
\llbracket \sigma_{r\theta} \rrbracket = \sigma_{r\theta}^{A}|_{\theta=\omega} - \sigma_{r\theta}^{B}|_{\theta=\omega} = 0, \text{ (continuity)},
\llbracket u_{\theta} \rrbracket = u_{\theta}^{A}|_{\theta=\omega} - u_{\theta}^{B}|_{\theta=\omega} = 0 \text{ (no-opening)},
\llbracket u_{r} \rrbracket = u_{r}^{A}|_{\theta=\omega} - u_{r}^{B}|_{\theta=\omega} = \frac{r^{\gamma}}{2\mu} \text{ (slip)}.$$
(63)

It is convenient to express stress and displacement in terms of a biharmonic function ϕ and a harmonic function ψ . Following Williams (1952), we then have the plane strain solution

$$2\mu u_{r} = -\frac{\partial \phi}{\partial r} + (1 - \nu)r \frac{\partial \psi}{\partial \theta},$$

$$2\mu u_{\theta} = -\frac{1}{r} \frac{\partial \phi}{\partial \theta} + (1 - \nu)r^{2} \frac{\partial \psi}{\partial r},$$

$$\sigma_{rr} = \frac{1}{r} \frac{\partial \phi}{\partial r} + \frac{1}{r^{2}} \frac{\partial^{2} \phi}{\partial \theta^{2}},$$

$$\sigma_{\theta\theta} = \frac{\partial^{2} \phi}{\partial r^{2}},$$

$$\sigma_{r\theta} = -\frac{\partial}{\partial r} \left(\frac{1}{r} \frac{\partial \phi}{\partial \theta} \right),$$
(64)

where μ is the shear modulus, ν is Poisson's ratio, and ϕ and ψ are related by

$$\nabla^2 \phi = \frac{\partial}{\partial r} \left(r \frac{\partial \psi}{\partial \theta} \right). \tag{65}$$

We use the ansatz (Williams 1952)

$$\phi^{A} = r^{\gamma + 1} \Big[A_{1} \sin((\gamma + 1)\theta) + A_{2} \cos((\gamma + 1)\theta) + A_{3} \sin((\gamma - 1)\theta) + A_{4} \cos((\gamma - 1)\theta) \Big],$$

$$\psi^{A} = r^{\gamma - 1} \left[-\frac{4A_{3}}{\gamma - 1} \cos((\gamma - 1)\theta) + \frac{4A_{4}}{\gamma - 1} \sin((\gamma - 1)\theta) \right],$$
(66)

on subdomain Ω^A for constants γ and A_1, \ldots, A_4 . We chose this ansatz including the smoothness parameter γ to discuss the dependence of the achieved convergence on the regularity of the solution. This specific analytical solution allows us to demonstrate that our achieved high-order convergence depends on the smoothness of the solution. The ansatz ϕ^B , ψ^B for subdomain Ω^B is defined likewise but with constants B_1, \ldots, B_4 . The constants are determined as following:

- (i)Use the free surface conditions to express A_1 , A_2 , B_1 , B_2 in terms of A_3 , A_4 , A_3 , A_4 , A_5 , A_5 .
- (ii)Add the slip equation and the continuity equation for $\sigma_{\theta\theta}$. Subtract the no-opening equation from the continuity equation for $\sigma_{r\theta}$. Use the resulting two equations to express A_3 in terms of B_3 and A_4 in terms of of B_4 .
- (iii) Find the remaining constants B_3 and B_4 from the continuity equations.

y = 0.5y = 10.5 A_1 0.208333333333333 -0.1666666666666670.072168783648703 A_2 2.7424137786507 -0.20833333333333330.16666666666667 A_3 0.21650635094611 -3.3197640478403 A_{Λ} $3.3017067341026 \cdot 10^{-15}$ B_1 -0.1250.072168783648703 3.0310889132455 B_2 $3.9968028886506 \cdot 10^{-15}$ B_3 -0.375-3.0310889132455 B_4 -0.072168783648703

Table 2. Numerical parameters for the dipping fault static test case.

In practice, we use SymPy (Meurer *et al.* 2017) to execute the above steps. The full procedure is provided in an openly available Jupyter notebook (see Data Availability). Furthermore, to avoid having to deal with infinite domains, we limit the A and B domains to $r \le 1$. At the 'new' boundary at r = 1 we impose the solution as Dirichlet boundary condition.

At last, we discuss the choice of the smoothness parameter γ . The term $\sin{(\pi \gamma)}$ appears in the denominator of B_3 and B_4 , thus we must choose $\gamma \in \mathbb{R} \setminus \mathbb{Z}$. Moreover, the term $r^{\gamma-1}$ appears in the stress tensor. Hence, $\gamma > 0$ in order to bound the strain energy (Barber 2004, sect. 11.2.1). More generally, the kth derivative of the displacement contains the term $r^{\gamma-k}$. The norm of this term on a wedge-shaped domain with maximum radius r_{max} , that is, $(\int_{\theta_1}^{\theta_2} \int_0^{r_{\text{max}}} r^{2(\gamma-k)} r \, dr \, d\theta)^{1/2}$, is only bounded if $\gamma > k-1$. Consequently, γ controls the smoothness of the solution. For example, for $0 < \gamma < 1$ the solution cannot be element of H^k with $k \ge 2$ and hence one cannot achieve high-order convergence using the SIPG method (Rivière 2008).

Here, we analyse the cases $\gamma = 0.5$ and 10.5. The constants of the respective solution are listed in Table 2.

7.1.2 Circular hole

In the second 2-D verification problem, we evaluate whether high-order convergence is achieved for a curved boundary. To this end, we let the domain be the unit disc with a small hole, that is, for hole-radius a we have $\Omega^a = \{x \in \mathbb{R}^2 : a < |x| < 1\}$. The domain is illustrated in Fig. 5(a) for a = 0.2. The hole's boundary is required to be traction free, that is,

$$\sigma_{rr} = \sigma_{r\theta} = 0, \quad \forall x \in \mathbb{R}^2 : |x| = a.$$
 (67)

The solution ansatz is the biharmonic function

$$\phi = -\frac{S_0}{2}r^2\sin(2\theta) + A\sin(2\theta) + Br^{-2}\sin(2\theta),\tag{68}$$

for constants S_0 , A, B (Barber 2004, §8.3.2). From the traction free boundary conditions, it follows that

$$A = S_0 a^2, \quad B = -\frac{S_0 a^4}{2}. \tag{69}$$

A harmonic function satisfying the compatibility condition (65) is

$$\psi = -2Ar^{-2}\cos(2\theta). \tag{70}$$

Hence, a displacement field satisfying the elasticity equations and eq. (67) is given by

$$2\mu u_r = S_0 r^{-3} \left(r^4 + 4a^2 r^2 (1 - \nu) - a^4 \right) \sin(2\theta) ,$$

$$2\mu u_\theta = S_0 r^{-3} \left(r^4 + 2a^2 r^2 (1 - 2\nu) + a^4 \right) \cos(2\theta) .$$
 (71)

We set $S_0 = 1$ and impose eq. (71) on the outer circular boundary (r = 1) as Dirichlet boundary condition.

7.1.3 Spherical hole

The spherical hole verification problem is the 3-D analogue of the circular hole test case. The domain is given by $\Omega^a = \{x \in \mathbb{R}^3 : a < |x| < 1,$ see Fig. 5(b), where the hole has radius a = 0.5. In spherical coordinates, that is,

$$x = R\cos(\theta)\sin(\beta), \ y = R\sin(\theta)\sin(\beta), \ z = R\cos(\beta), \tag{72}$$

where $\theta \in [-\pi, \pi)$ and $\beta \in [0, \pi)$, we look for a displacement field which satisfies

$$\sigma_{RR} = \sigma_{R\theta} = \sigma_{R\beta} = 0, \quad \forall x \in \mathbb{R}^3 : |x| = a. \tag{73}$$

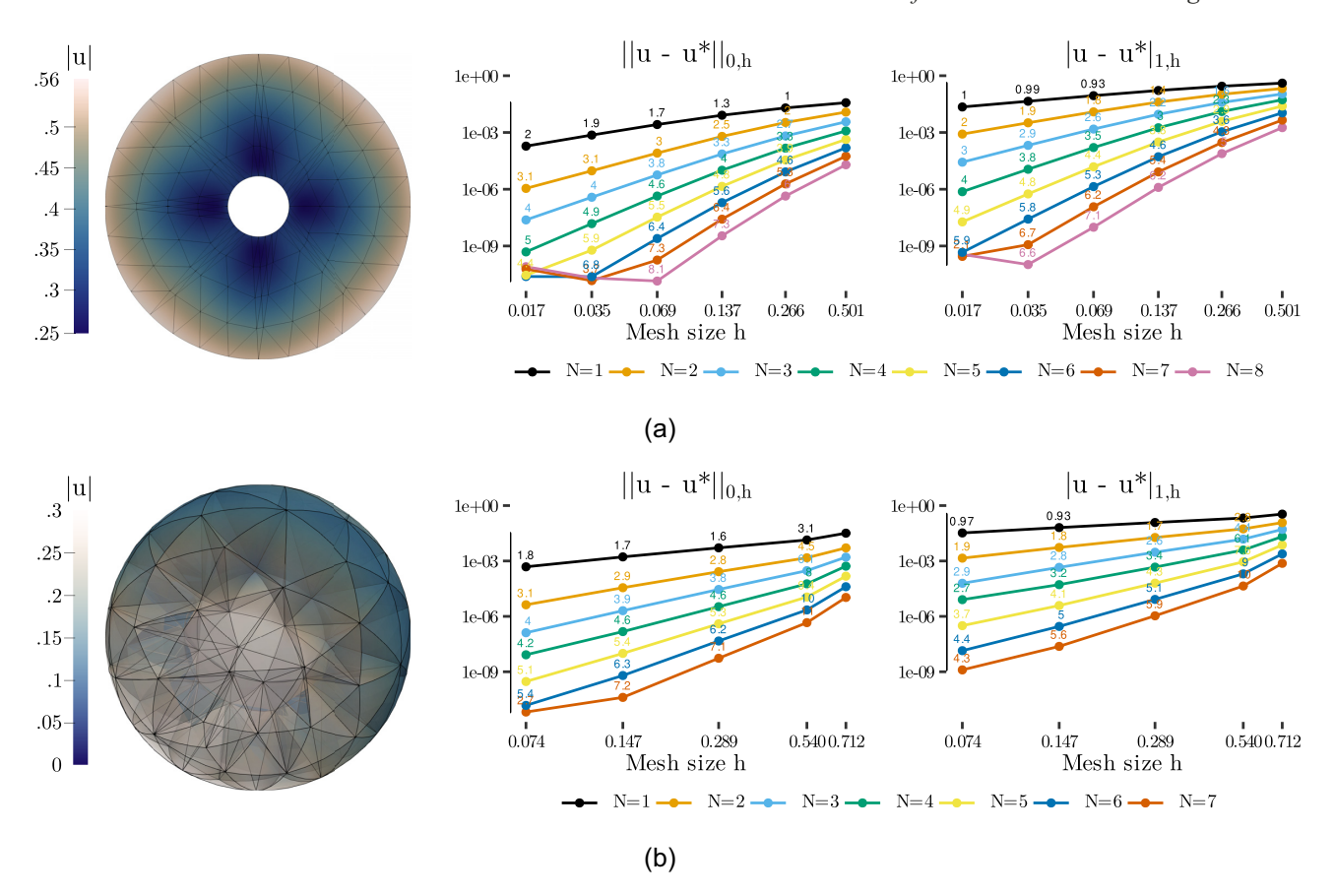


Figure 5. Results of the circular and spherical hole convergence tests which verify high-order convergence of the elasticity solver using curvilinear grids. The empirical convergence order, printed in small text above points, mostly matches the theoretical expectations. (a) Circular hole verification problem setup in 2-D. Left: snapshot of the solution and mesh. Middle and right: convergence test results. (b) Spherical hole verification problem in 3-D. Left: snapshot of the solution and mesh. Middle and right: convergence test results.

Barber (2004, sect. 24.1.2) gives potentials ϕ , ω from which stress fields satisfying eq. (73) are derived. The displacement field can be computed from these potentials (Barber 2004, table 19.2). After simplifying the resulting expressions, we have $u_{\theta} = 0$ and

$$2\mu u_{R} = S_{0} \left(\frac{R(1-\nu)}{2(1+\nu)} + \frac{a^{3}(10\nu - 13)}{4R^{2}(5\nu - 7)} + \frac{3a^{5}}{4R^{4}(5\nu - 7)} \right) + S_{0} \left(\frac{R}{2} + \frac{5a^{3}(4\nu - 5)}{4R^{2}(5\nu - 7)} + \frac{9a^{5}}{4R^{4}(5\nu - 7)} \right) \cos(2\beta),$$

$$2\mu u_{\beta} = -\frac{RS_{0}}{2} \left(\frac{5R^{2}a^{3}(1-2\nu) + 3a^{5}}{R^{5}(7-5\nu)} + 1 \right) \sin(2\beta). \tag{74}$$

We set $S_0 = 1$ and impose eq. (74) on the outer sphere (r = 1) as a Dirichlet boundary condition.

7.1.4 Heterogeneous material parameters

The material parameters are heterogeneous and set to

$$\mu(\mathbf{x}) = 1 + \sin(10\pi x_1)/4,$$

$$\lambda(\mathbf{x}) = 1 + \sin(10\pi x_2)/4.$$
(75)

The solution is manufactured to be

$$u^*(x) = (\cos(\pi x_1)\cos(\pi x_2), 0). \tag{76}$$

We ensure that the manufactured solution is a solution of eq. (14) by using only Dirichlet boundaries with $g^D = u^*$ and

$$f_i = -\frac{\partial \sigma_{ij}(\mathbf{u}^*)}{\partial x_i}.\tag{77}$$

The force term is computed using the symbolic math package SymPy (Meurer *et al.* 2017). The domain is chosen as the unit square as illustrated in Fig. 6.

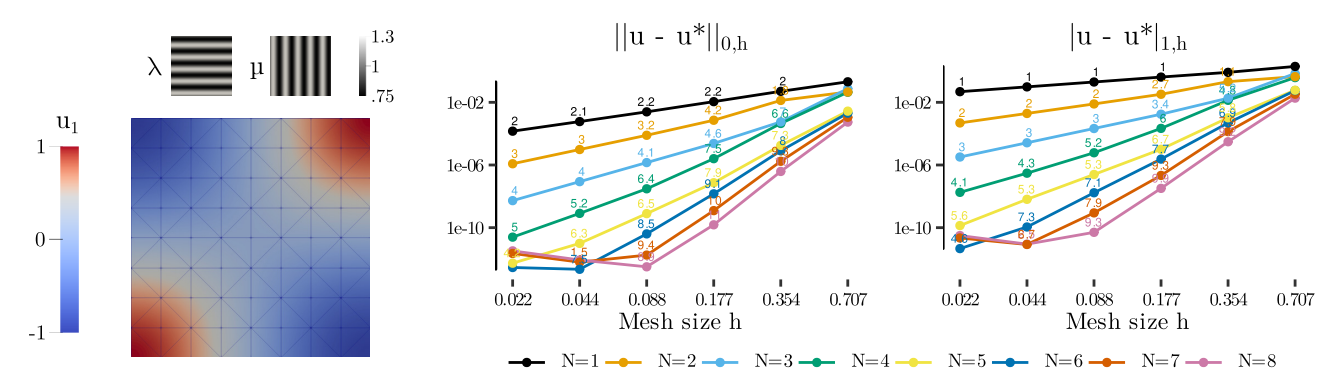


Figure 6. Verification of heterogeneous material parameters. The empirical convergence order, printed in the small text above points, mostly matches the theoretical expectations. Left: snapshot of the solution and mesh of the unit square with heterogeneous material parameters. Middle and right: convergence test results.

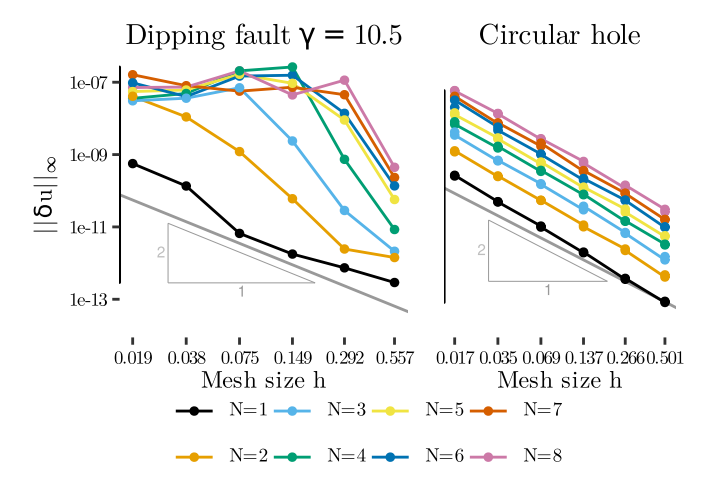


Figure 7. The conditioning of linear systems amplifies errors in the residual, that is, the error $\underline{\delta u}$ might be large even if the residual is reduced down to machine precision. Here, we show bounds on the error $\underline{\delta u}$ obtained by MUMPS for two scenarios (left: dipping fault and right: circular hole). The h^{-2} scaling is added for reference in grey.

7.1.5 Results

We conduct a convergence study for the four described test problems for polynomial degrees N = 1, ..., 8. Again, mesh sequences are generated with Gmsh version 4.8.4 (Geuzaine & Remacle 2009; Johnen *et al.* 2013). Based on a CAD model, an initial degree 8 coarse mesh is generated and successively refined such that the mesh size is roughly halved with respect to the previous mesh in the sequence. The heterogeneous material parameter verification setup is an exception, here we use an uniform mesh generator for rectangular domains. If the solution is smooth enough, the convergence order is expected to be N + 1 for displacement and N for the first derivatives (Castillo *et al.* 2000; Rivière 2008).

We first discuss the numerical convergence results for the slip boundary condition. For the case $\gamma=0.5$ we showed in Section 7.1.1 that only the first (weak) derivative of the displacement solution exists. Thus, a convergence order below one is expected independent of the polynomial degree N (Rivière 2008). Empirically, we find that the convergence order is about 0.5 (Fig. 4b). Still, the error is reduced by a constant factor with increasing polynomial degree, for example the error for N=8 is one tenth of the error for N=1 and 8 on the finest mesh. For the case $\gamma=10.5$ the empirical convergence order is close the expected order N in the $|.|_{1,h}$ semi-norm, but we observe that the error is not reduced below 5×10^{-10} . The condition number of the operator A is in $\mathcal{O}(h^{-2})$ (Antonietti & Houston 2011), hence even when reducing the residual down to machine precision the error might be much larger than machine precision.

A posteriori error analysis of the linear solve is offered by the direct sparse solver MUMPS (Amestoy et al. 2001, 2019) using the method of Arioli et al. (1989). The error analysis returns a bound on $\underline{\delta u}$, that is, a bound on the error introduced in the degrees of freedom by finite precision effects. The results of the error analysis for the dipping fault test case and the circular hole test case are shown in Fig. 7. We see that an error in the degrees of freedom of at most 2×10^{-7} in the infinity norm is possible. Therefore, the minimum achievable error in Fig. 4(b) is explained by the amplification of the error in the residual due to conditioning of the linear system. Moreover, the error bound roughly follows the h^{-2} scaling of the condition number.

We next discuss the numerical convergence results of the circular hole and spherical hole verification cases shown in Fig. 5. For degrees $N = 1, \ldots, 6$ the empirical convergence orders match the theoretical expectation very well in both the $\|.\|_{0,h}$ norm and $\|.\|_{1,h}$ semi-norm. For degrees N = 7 and 8, the empirical orders are slightly off but still increase with increasing N. We also repeated the test for an affine mesh (i.e.

Table 3. Circular hole verification problem on an affine mesh sequence. Shown are the errors and empirical convergence orders on the finest mesh (h = 0.017). The convergence order is limited due to linear approximation of the inner and outer circle.

N	$ u - u^* _{1, h}$	$\mathcal{C}_{1,h}$	$\ u-u^*\ _{0,h}$	$\mathcal{C}_{0,h}$
1	2.23271e-02	1.0	1.89689e-04	2.0
2	8.23588e-04	2.0	3.02087e-06	2.4
3	5.53858e-05	2.2	2.62902e-06	2.0
4	7.07560e-05	1.6	2.62783e-06	2.0
5	9.18152e-05	1.5	2.62678e-06	2.0
6	1.16266e-04	1.5	2.62560e-06	2.0
7	1.43651e-04	1.5	2.62449e-06	2.0
8	1.69295e-04	1.5	2.62369e-06	2.0

degree 1), as shown in Table 3. Due to the linear approximation of the boundary the convergence order in the $\|.\|_{0,h}$ norm is reduced to 2 (with a curious exception for N=2 where it is slightly higher), which shows that the curvilinear geometry approximation is necessary to retain high-order convergence. In the spherical hole test case theoretical expectations are well met until N=3. The empirical convergence orders for higher degrees are lower than expected but still increase with increasing N. The condition number of the circular hole test case increases with h^{-2} , as shown in Fig. 7, such that the error is not reduced below 10^{-11} , and, once the minimum attainable error is reached, gets slightly worse under mesh refinement.

Lastly, high-order convergence is also achieved when material parameters are smoothly varying in space (Fig. 6).

7.2 Convergence of the SEAS solver

Establishing convergence of a SEAS model is difficult as there are no known analytic solutions. However, by adding a source term to the state equation one can manufacture a solution. Erickson & Dunham (2014) manufactured such a solution for a 2-D antiplane shear problem (where the elasticity equations reduce to a Poisson equation). Here, we propose a manufactured verification problem for plane strain elasticity.

7.2.1 Domain

Assume that the fault lies in the $x_1 = 0$ plane. The first step is to construct a displacement field possessing a tangential component which is discontinuous at the fault, but with a normal component and traction which are continuous. That is, u_1 , σ_{11} and σ_{12} are continuous, but u_2 is discontinuous. We find that the Airy stress function (Barber 2004)

$$\Phi^{\pm}(\mathbf{x}) = x_1 K(t) \exp(-k^{\pm} x_1) \cos(k^{\pm} x_2) \tag{78}$$

leads to a displacement field with the desired properties. K(t) is a time-dependent function and we define $k^+ = k$ and $k^- = -k$ for a constant k. Indeed, the stress and displacement components are

$$\sigma_{11}^{\pm} = -k^{2}x_{1}K \exp(-k^{\pm}x_{1}) \cos(k^{\pm}x_{2}),$$

$$\sigma_{22}^{\pm} = k^{\pm}(k^{\pm}x_{1} - 2)K \exp(-k^{\pm}x_{1}) \cos(k^{\pm}x_{2}),$$

$$\sigma_{12}^{\pm} = k^{\pm}(1 - k^{\pm}x_{1})K \exp(-k^{\pm}x_{1}) \sin(k^{\pm}x_{2}),$$

$$u_{1}^{\pm} = \frac{k^{\pm}x_{1}(\nu + 1) - 2\nu^{2} - \nu + 1}{E}K \exp(-k^{\pm}x_{1}) \cos(k^{\pm}x_{2}),$$

$$u_{2}^{\pm} = \frac{k^{\pm}x_{1}(\nu + 1) + 2\nu^{2} - 2}{E}K \exp(-k^{\pm}x_{1}) \sin(k^{\pm}x_{2}),$$

$$(79)$$

where E is Young's modulus and ν is Poisson's ratio. For $x_1 = 0$, we have $\sigma_{11}^- = \sigma_{11}^+$, $\sigma_{12}^- = \sigma_{12}^+$, $u_1^- = u_1^+$, but

$$[\![u_2]\!] = u_2^- - u_2^+ = 4\frac{1 - v^2}{E} K \sin(kx_2).$$
(80)

Following Erickson & Dunham (2014), we choose K as

$$K(t) = \frac{2}{\pi} \left(\arctan\left(\frac{t - t_e}{t_w}\right) + \frac{\pi}{2} \right),\tag{81}$$

such that there will be one 'event' at time t_e with a duration of about t_w (Table 4).

The domains are $\Omega^- = (-3/5, 0) \times (-4/5, -1/5)$ and $\Omega^+ = (0, 3/5) \times (-4/5, -1/5)$. On the internal fault boundary $\Gamma^F = \{0\} \times [-4/5, -1/5]$ we impose the slip $[u_2]$. On the remaining boundary, $\Gamma^{D, \pm} = \partial \Omega^{\pm} \backslash \Gamma^F$ we impose the displacement field from eq. (79).

Table 4. Parameters for the 2-D plane strain SEAS model.

Parameter	Value	Parameter	Value
$\overline{t_e}$	50 s	а	0.015
t_w	1 s	b	0.02
ρ_0	$2670 \mathrm{kg} \mathrm{m}^{-3}$	V_0	$1 \times 10^{-6} \mathrm{m s^{-1}}$
C_S	$3.464 \; \mathrm{km} \mathrm{s}^{-1}$	f_0	0.6
ν	0.25	k	π
E	$2c_s^2/\rho_0(1+\nu)$ Pa	σ_n^0	$25 \sin(kx_2) MPa$
η	$2c_s^2/\rho_0(1+\nu)$ Pa $\rho_0c_s/2$ Pa s m ⁻¹	T^{0}	$20 \sin(kx_2) MPa$

7.2.2 Fault

We add a source term independent of state ψ and slip S to the state equation, that is,

$$\frac{\mathrm{d}\psi}{\mathrm{d}t} = G(V, \psi) + s(\mathbf{x}, t). \tag{82}$$

The source term is defined as

$$s(\mathbf{x},t) = -G(V^*, \psi^*) + \frac{\mathrm{d}\psi^*}{\mathrm{d}t},\tag{83}$$

where $V^*(x, t)$ and $\psi^*(x, t)$ are the manufactured solutions. Given that $V(x, 0) = V^*(x, 0)$ and $\psi(x, 0) = \psi^*(x, 0)$ the fields V^* , ψ^* are a solution for eq. (82).

The manufactured slip S^* needs to be compatible with the solution in the domain, in particular with eq. (80). With the fault normal (1, 0) and tangent (0, -1) we have $S^* := -[u_2]$. It follows that the manufactured slip rate is given by

$$V^* = -4\frac{1-\nu^2}{E} dK dt \sin(kx_2).$$
 (84)

Likewise, from eq. (79)-, the manufactured on-fault normal and shear stresses are

$$\sigma_n^* = \sigma_n^0 - \sigma_{11}|_{x_1=0} = \sigma_n^0,$$

$$T^* = T^0 - \sigma_{12}|_{x_1=0} = T^0 - kK\sin(kx_2),$$
(85)

with background stress σ_n^0 , T^0 .

Lastly, the manufactured quantities need to satisfy the friction law. From eqs (6) and (12), we have

$$-T^* = \sigma_n^* a \operatorname{arcsinh}\left(\frac{V^*}{2V_0} \exp\left(\frac{\psi^*}{a}\right)\right) + \eta V^*. \tag{86}$$

Solving the above equation for ψ^* , we obtain

$$\psi^* = a \ln \left(\frac{2V_0}{V^*} \sinh \left(-\frac{T^* + \eta V^*}{\sigma_n^* a} \right) \right). \tag{87}$$

The parameters a, V_0 , η as well the background stress and all other parameters are summarized in Table 4.

7.2.3 Results

We conduct a convergence study for polynomial degrees N = 1, ..., 8. The mesh sequence is generated with an uniform mesh generator for rectangular domains. The final simulation time is set to $t_{\text{end}} = 2t_e = 100$ s. We report the error at t_{end} , where the time-dependent error is given by

$$\left(\sum_{e \in \Gamma^F} \int_e (\psi - \psi^*)^2 + (S - S^*)^2 \, \mathrm{d}s\right)^{1/2}.$$
(88)

Time stepping is handled by PETSc/TS (Abhyankar *et al.* 2018; Balay *et al.* 2021a). We use adaptive Runge–Kutta methods such as the third order Bogacki–Shampine scheme (3bs) with the second-order embedded method or the fifth-order Dormand–Prince scheme (5dp) with the fourth-order embedded method. The local truncation error is estimated by the difference between the fifth- (third-) order method and the fourth- (second-) order embedded method. Time-step sizes are adapted automatically such that the estimated local truncation error stays below a given absolute tolerance. We set an absolute tolerance of 10^{-12} and find that the choice of time-stepping method has little impact when the error is above the error tolerance, cf. the solid and dotted lines in Fig. 8. Therefore, we only discuss the results of method 5dp.

The effective frictional resistance is related to traction via the empirical rate and state friction law, thus, we expect a maximum convergence order of N. The results in Fig. 8 show that order N is reached, although the absolute error tolerance limits the minimum achievable error. Curiously, for N = 1 the empirical convergence order is close to two.

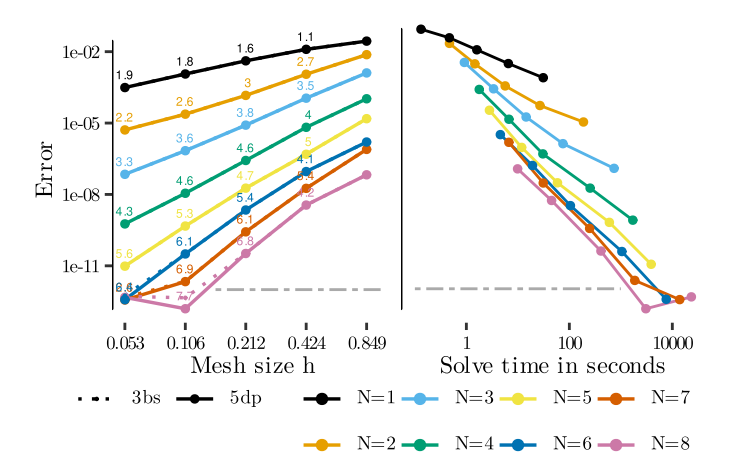


Figure 8. Results of convergence analysis for the manufactured SEAS problem. Left: the empirical convergence order, printed in small text above points, is close to the polynomial degree N in almost all cases. Right: the error versus time-to-solution plot shows that high-order pays off for this problem. The absolute tolerance of 10^{-12} used to select time steps is indicated by the grey dashed line. The error reported on the y-axis is given by eq. (88).

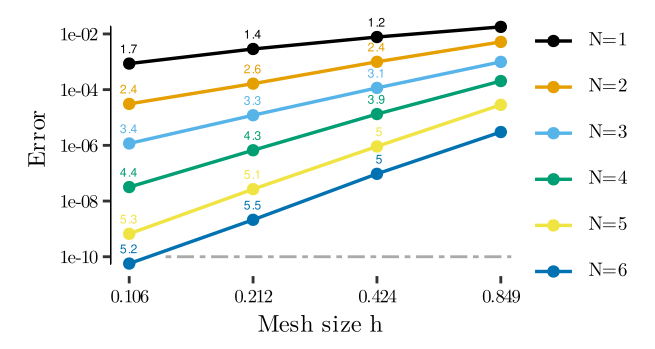


Figure 9. Convergence results for the manufactured 3-D SEAS problem. The absolute tolerance of 10^{-10} used to select time steps is indicated by the grey dashed line. The error reported on the y-axis is given by eq. (88).

Plotting the error versus the solve time (Fig. 8) shows that high-order clearly pays off. For example, for N=1 the error on the finest grid is 3.1×10^{-4} and the solve time increases by about a factor of 4 when the mesh size is halved. Assuming second-order convergence, one needs about eight refinement steps to reach an error of 1×10^{-8} . Therefore, an increase in solve time by 4^8 is necessary, that is, about 24 d. In contrast, a solve time of about 45 s is required to fall below the same error threshold for the N=8 scheme.

We extend the manufactured verification setup in a straightforward manner to three dimensions, essentially by solving the 2-D problem with the 3-D scheme. We run the 3-D test case for polynomial degrees $N = 1, \ldots, 6$ setting an absolute tolerance of 1×10^{-10} . The results are shown in Fig. 9. The empirical convergence order is close to N.

7.3 SEAS Benchmark Problem 1 (BP1)

Another means of verification is a code comparison in which a representative physical problem is defined and solved by different groups, with different numerical methods and implementations (e.g. Harris *et al.* 2018; Buiter *et al.* 2016), and the results of all approaches are subsequently compared. While this approach does not reveal the 'ground truth', we can analyse the variation between codes. A community code comparison is organized by the SEAS working group (Erickson *et al.* 2020) of the Southern California Earthquake Center (SCEC). We use their *Benchmark Problem 1 (BP1)* to test several aspects of our method: first, we investigate whether local (statically adaptive) mesh refinement is effective in comparison to uniform mesh refinement. Second, we check whether p-refinement improves our results significantly for the BP1 problem where the regularity of the solution is unknown. Lastly, we verify that a high-resolution simulation with our method matches the results of other groups.

BP1 is a 2-D antiplane problem, with a 1-D planar vertical strike-slip fault embedded in a 2-D homogeneous, linear elastic half-space with a free surface. The required problem resolution can be characterized considering two inherent critical length scales. First, the (often approximated as quasi-static) process zone size which describes the spatial region near the rupture front under which breakdown of fault resistance occurs (Palmer & Rice 1973; Day *et al.* 2005; Ampuero & Rubin 2008). Second, the critical nucleation size, which governs the minimum extend of the rate-weakening region under which spontaneous nucleation may occur (Andrews 1976a, b; Rubin & Ampuero 2005). For BP1, the suggested (low-order) model resolution is a cell size of 25 m on-fault (Erickson *et al.* 2020) resolving the quasi-static process zone with 12 and the critical nucleation zone with 80 gridpoints. For our high-order approach, cell size can be interpreted as an average resolution per degree of freedom along the face of an element. In Section 7.3.3, we will verify *Tandem* with an on-fault mesh size 10 times

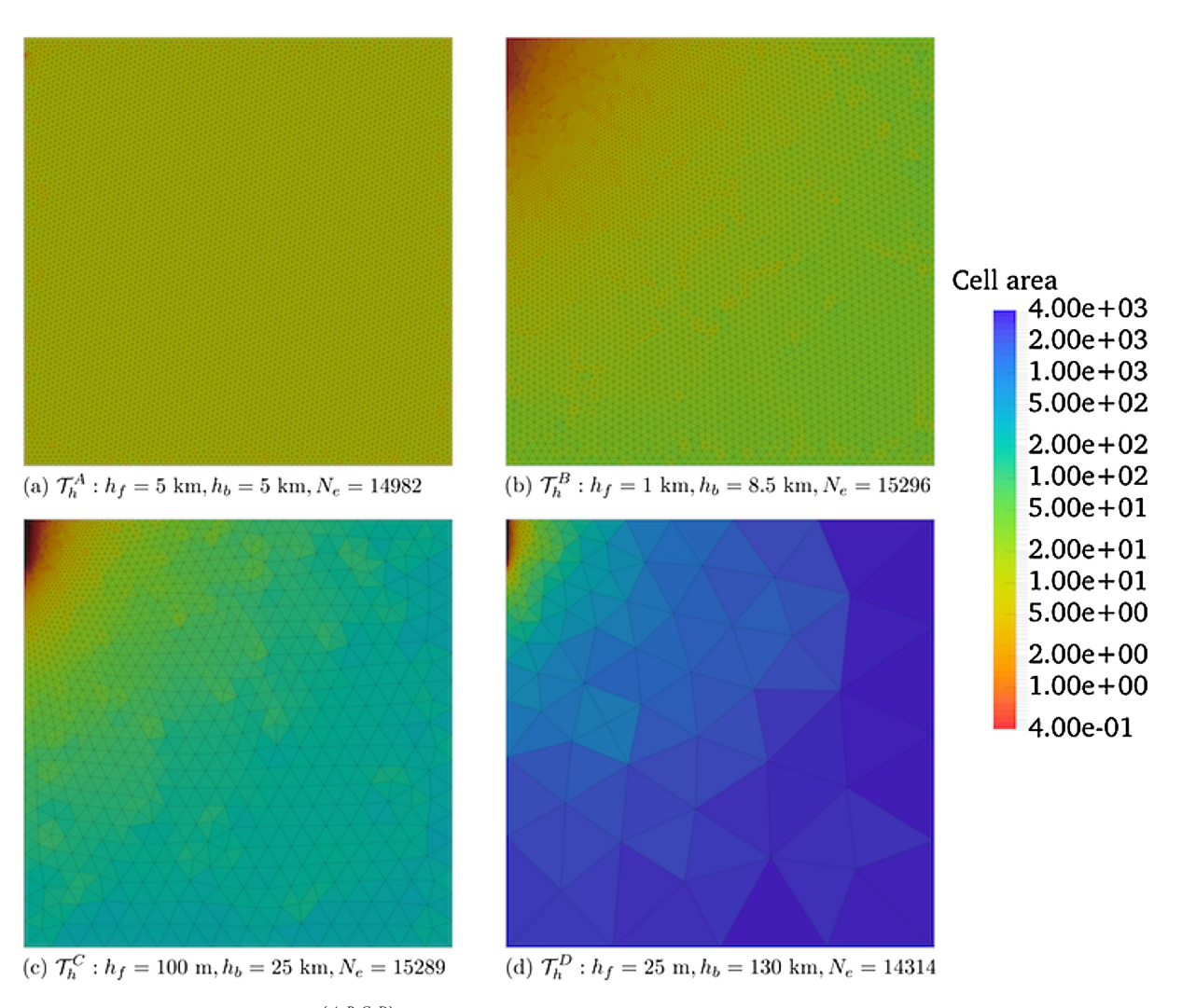


Figure 10. Family of unstructured meshes $(\mathcal{T}_h^{\{A,B,C,D\}})$ used for BP1, each with approximately the same number of elements N_e . Each mesh is constructed by specifying a target spatial resolution (triangle edge length) along the fault (h_f) and elsewhere along the exterior boundary (h_b) . The degree of local refinement is emphasized by colouring cells according to their area (km^2) , where red hues indicates regions of high local spatial resolution and blue hues denote regions of low local spatial resolution.

larger than the 25 m recommended for BP1 using code comparison. We refer to Erickson *et al.* (2022) for a detailed discussion of numerical resolution requirements of *Tandem* compared to other BEM and volumetric codes for quasi-dynamic SEAS simulations.

7.3.1 Local h-refinement

One of the issues raised by Erickson *et al.* (2020) when using volume based discretizations for BP1 is the unknown effect of the prescribed finite sized domain on the solution. Using an unstructured mesh, addressing this issue can be tackled efficiently. In the following, we chose a 2-D volumetric domain as a $[0 \text{ km}, 400 \text{ km}] \times [-400 \text{ km}, 0 \text{ km}]$ rectangle. Four unstructured meshes were constructed with approximately the same number of elements, but with differing spatial resolution on-fault (h_f) and off-fault. The off-fault resolution is controlled by specifying the spatial resolution (h_b) on the exterior boundary not containing the fault. In practice, we selected h_f and adjusted h_b to produce a mesh with approximately 15 000 cells. The four meshes (shown in Fig. 10) were defined using $h_f = \{5000, 1000, 100, 25\}$ m. The end-members (\mathcal{T}_h^A , \mathcal{T}_h^D) have an approximately uniform spatial resolution of 5 km, and an on-fault resolution of 25 m and an off-fault resolution of 130 km, respectively.

In Fig. 11, we report the simulated shear stress over five seismic cycles using the four different meshes and a degree N=2 polynomial. For cases when $h_f \ge 1$ km, our solutions dramatically deviate from the reference solution (grey line in Fig. 11). In comparison, the higher resolution simulations using an on-fault resolution of 100 m (green line $-\mathcal{T}_h^c$) and 25 m (black line $-\mathcal{T}_h^D$) are seen to closely follow the reference in terms of both, phase and amplitude.

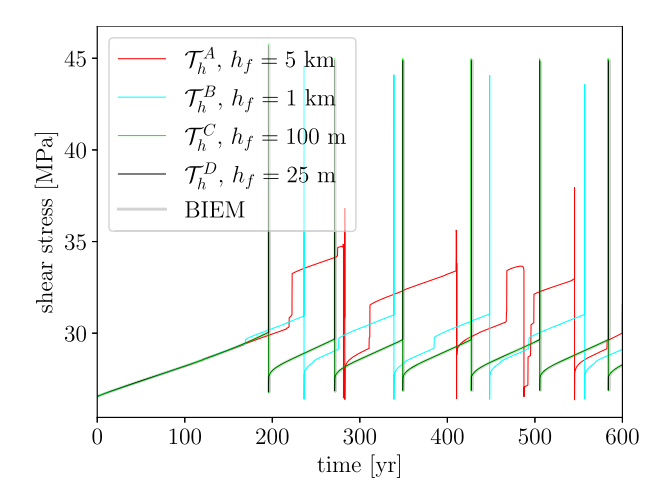


Figure 11. Shear-stress obtained from BP1 on different meshes compared with the reference BIEM solution (grey line) from C. Cattania (Erickson *et al.* 2020). All experiments used a polynomial degree of N = 2.

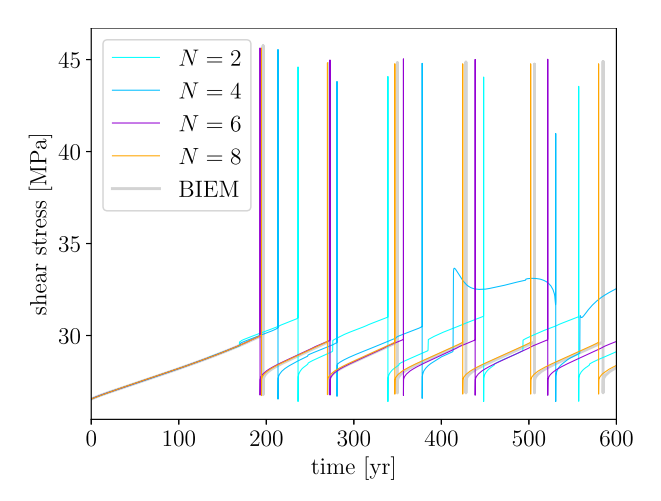


Figure 12. Shear-stress obtained from BP1 on mesh \mathcal{T}_h^B ($h_f = 1 \text{ km}$) as a function of polynomial degree N = 2, 4, 6 and 8 compared with the reference BIEM solution (grey line) from C. Cattania (Erickson *et al.* 2020).

7.3.2 p-refinement

To highlight the benefits of using high polynomial degree function spaces, we conducted simulations using T_h^B and vary the polynomial degree N. The rational for selecting one of the 'low-resolution' meshes (as inferred from the cell sizes h_f , h_b) is that with higher N, we expect that higher spatial resolution should be achieved even if the cell sizes h, where $h_f \le h \le h_b$, are in fact large. In Fig. 12, this expectation is seen to be correct. For low degrees (N = 2, 4) the solutions obtained are inaccurate in terms of phase, amplitude and number of cycles. The degree N = 6 results (purple line) are very similar to the reference solution (grey line) with a slight phase shift. The highest degree used N = 8 is visually seen to yield the closest agreement with the reference solution. Despite the small phase shift associated with N = 8 simulations, the actual recurrence interval is very similar to the reference, and more accurate than that obtained from the lower degree experiments (see Table 5).

7.3.3 Code comparison

We compare a high-resolution run using our method (N = 8) with other codes. The domain is chosen as the $[0 \text{ km}, 400 \text{ km}] \times [-400 \text{ km}, 0 \text{ km}]$ rectangle. Note that only half of the domain needs to be modelled due to symmetry. The boundaries y = -400 and 0 km are traction-free and we impose the displacement $V_p t/2$, $V_p = 1 \times 10^{-9} \text{m s}^{-1}$, on the x = 400 km boundary. The on-fault mesh size is 250 m and the mesh size is gradually coarsened to 50 km towards the far boundaries for a total of 3648 triangles. We note that the on-fault mesh size is 10 times larger than the 25 m mesh size recommended for BP1.

The slip rate at 7.5 km depth is compared to eight different reference solutions taken from Erickson *et al.* (2020) in Fig. 13. Overall, we find good agreement in the long-term behaviour. The largest deviation is seen in the onset time of the later earthquake events, which might result from different choices of domain size, as discussed in Erickson *et al.* (2020). Yet, overlaying the eighth event and correcting for the time shift (Fig. 13, lower panel) shows that the coseismic behaviour closely matches the other codes.

Table 5. Recurrence time (Δt_r) estimates from last cycle associated with the simulations reported in Figs 11 and 12. The simulation marked with '–' indicate that a stable periodic sequence of events was not obtained. The reference Δt_r from C. Cattania was 78.34 yr.

Mesh	$h_f(\mathbf{m})$	N	$\Delta t_r (yr)$	
$\overline{\mathcal{T}_h^A}$	5000	2	_	
$\mathcal{T}_h^{\dot{B}}$	1000	2	108.6	
\mathcal{T}_h^{C}	100	2	78.22	
\mathcal{T}_h^A \mathcal{T}_h^B \mathcal{T}_h^C \mathcal{T}_h^D	25	2	78.28	
\mathcal{T}_h^B	1000	4	89.5	
\mathcal{T}_{h}^{B}	1000	6	82.9	
\mathcal{T}_h^B \mathcal{T}_h^B \mathcal{T}_h^B	1000	8	77.6	

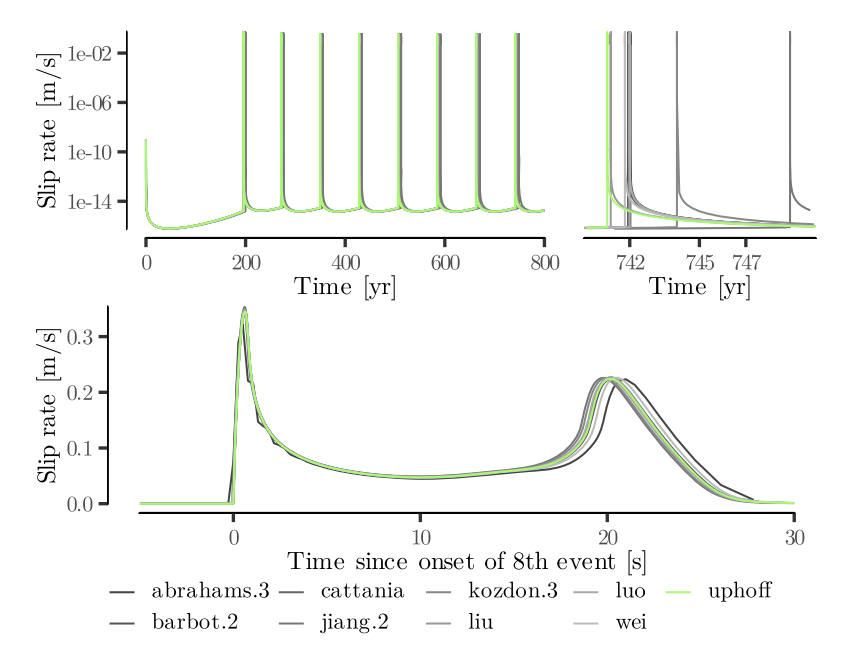


Figure 13. Comparison of the BP1 problem to Erickson *et al.* (2020, figs 5 and 6). Top left: evolution of slip rate over 800 yr at 7.5 km depth. Top right: detail view of the eighth event. The onset time of the event deviates largely between codes. Bottom: we shift the time-series by their onset time of the eighth event. The onset time is here defined as the first time when the slip rate is greater or equal than 0.001 m s^{-1} .

8 NUMERICAL EXPERIMENTS

We apply the SIPG method to two geometrically complex demonstration models and elucidate the importance of using curvilinear fault representations, compared with piecewise linear approximations (affine), when accurate stresses (or displacement gradients) are required on-fault. SEAS simulations including more than one fault segment and complex fault geometries are methodologically challenging (Romanet *et al.* 2018; Galvez *et al.* 2020; Luo *et al.* 2020; Barbot 2021, see also Section 9.2), but crucial to understand large earthquakes that often span several segments of natural regional-scale fault networks (Plesch *et al.* 2007; Ando & Kaneko 2018; Ulrich *et al.* 2019; Harris *et al.* 2021). Specifically, fault intersections and fault triple junctions require enforcement of the continuity of the slip vector (King 1983; Andrews 1989; Romanet *et al.* 2020) and how to consistently handle locally infinite stresses in BEM and volumetric methods is an open question.

Our first demonstrator consists of a 2-D SEAS model defined by a shallowly dipping normal fault interacting with four curved splay faults. We report application run-times illustrating the speed-up when computing the discrete Green's functions compared to the fully volumetric approach. In the second demonstrator, we consider a 3-D elastostatic model defining a kinematic scenario of instantaneous deformation inspired by the 2019 Ridgecrest earthquake sequence. Both applications can be simulated by either pre-computing the discrete Green's functions (Section 6) or using the fully volumetric capabilities of *Tandem*. The results are identical, but computational cost in terms of run-time and model setup varies. Both applications are here presented as proof-of-concepts. Detailed geophysical analysis and including further realistic modelling ingredients, such as subsurface material heterogeneity, will be included in future work.

8.1 A 2-D SEAS multifault scenario on a shallowly dipping normal fault with four curved splay faults

The mechanics of splay fault systems are of specific interest to seismic and tsunami hazard assessment and to understand shallowly observed slow slip transients (Wendt et al. 2009; Ikari et al. 2013). The potential of large slip on detachment normal faults has been extensively

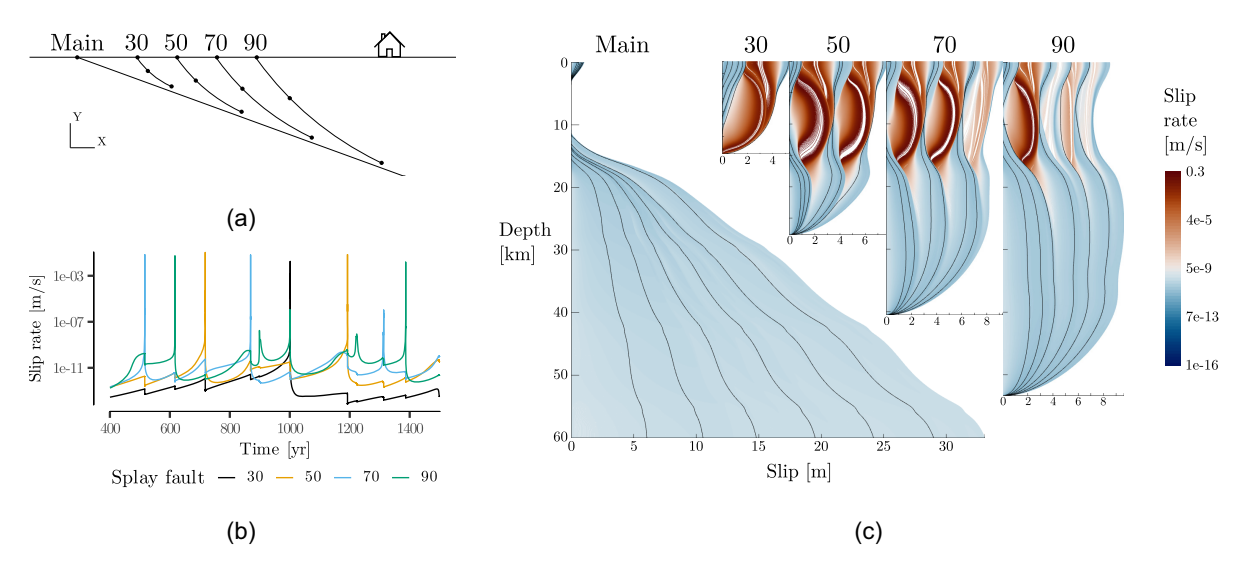


Figure 14. Results of the low-angle normal fault quasi-dynamic SEAS scenario with four curved splay faults, sketched in (a), using curvilinear elements and discrete Green's functions. The model consists of a low-angle normal fault and four splay faults which do not intersect the main fault. Numbers indicate the offset of each splay fault in kilometres in the x-direction with respect to the intersection of the main shallowly dipping normal fault with the free surface. (b) Time-series of slip rate at 10 km depth for each splay fault. We observe an irregular series of small and large events at all splay faults as shown in (b). (c) Slip plotted versus depth coloured by slip rate for the main fault and the four splay faults. Black contours indicate that 200 yr have passed, that is, the leftmost black contour line shows t = 200 yr and the right-most black contour line shows t = 1400 yr. The complete evolution of slip and slip rate over 1500 yr is shown, where a slip contour is drawn whenever the maximum slip rate changed by 10 per cent (or more). Red areas indicate a seismic event and light blue areas indicate creeping at plate rate.

Table 6. Parameters for the splay fault scenario.

Parameter	Value	Parameter	Value
a_{max}	0.025	a_0	0.010
L	0.05 m	b	0.015
f_0	0.6	ν	0.25
ρ_0	2670 kg m^{-3}	C_S	$3.464 \text{ km} - \overline{1} \text{s}^{-1}$
V_p	$-1 \times 10^{-9} \mathrm{ms^{-1}}$	V_0	$1 \times 10^{-6} \mathrm{m s^{-1}}$
$V_p = \sigma_n^0$	50 MPa	T^0	26.5461 MPa
η	$ ho_0 \mathrm{c_s} / \mathrm{2Pasm^{-1}}$	$t_{\rm end}$	1500 yr

debated. The geological record shows that shallowly dipping (<30°) crustal-scale detachment faults play a major role in accommodating extension at divergent plate boundaries (Collettini 2011, e.g.). However, such shallowly dipping normal faults appear to challenge the laws of classic static fault mechanical analysis (e.g. Fletcher *et al.* 2016; Anderlini *et al.* 2016; Webber *et al.* 2018; Biemiller *et al.* 2020, 2021). Furthermore, detachment systems can often be complex with more steeply dipping splay-faults rendering the hanging wall. Such splay faults may slip co-seismically (e.g. Biemiller *et al.* 2022) posing seismic and tsunami hazard or relieve shallow interseismic stress on detachments by subsidiary creep. We demonstrate the potential of our method to model seismic and aseismic slip naturally interacting across a main fault with multiple, geometrically complex splay faults. Similar fault system geometries are also ubiquitous in subduction zone megathrust fault systems (Park *et al.* 2002; Waldhauser *et al.* 2012), where splay fault slip trading off with slip to the trench is thought to play an important role in tsunamigenesis (Gao *et al.* 2018; Aslam *et al.* 2021; Ulrich *et al.* 2022; van Zelst *et al.* 2022).

We create a fault system model consisting of a planar, $\delta_0 = 20^\circ$ dipping main normal fault and four curved splays faults, as shown in the sketch in Fig. 14(a). For each splay fault three control points are defined that would model a 50° and a 40° dipping fault segment when connected by straight lines. Here, we define the splay faults as the spline interpolant of the three control points (using Gmsh's Spline geometry object). The fault system is embedded in the $(X_0, X_1) \times (Y_0, Y_1)$ box, where $X_0 = -1000$ km, $X_1 = 1000$ km($1 + \cos{(\delta_0)}/\sin{(\delta_0)}$), $Y_0 = -1000$ km and $Y_1 = 0$ km. The origin of the main normal fault coincides with the origin of the coordinate system and the splays are labelled according to their offsets given by 30, 50, 70 and 90 km, respectively. With V_p negative (refer to Table 6), the domain is under extension and we model normal faulting. Natural boundary conditions are imposed on the top $(y = Y_0)$ and bottom $(y = Y_1)$ boundary of the model domain. On the left $(x = X_0)$ boundary we impose $u_1 = V_p t/2$, $u_2 = 0$ m and on the right $(x = X_1)$ boundary we impose $u_1 = -V_p t/2$, $u_2 = 0$ m.

We adopt a piecewise linear parametrization of rate and state friction law parameters a-b as proposed by Rice (e.g. 1993), resembling intact granite (Blanpied *et al.* 1991). We hold *b* constant and let *a* depend on depth by piecewise linear interpolation of the points (0 km, a_{max}), (4 km, a_0), (15 km, a_0) and (18 km, a_{max}). We hold *a* constant at a_{max} below a depth of 18 km. Given a_0 , a_{max} and *b* as in Table 6, we have

velocity weakening behaviour in (8/3 km, 16 km) and velocity strengthening above and beneath that depth range. All material parameters and other parameters of the rate and state model are constant and given in Table 6.

We follow a refinement strategy analogue to Section 7.3, and set the on-fault resolution to $h_f = 0.5$ km and the far boundary resolution to h = 100 km for a total of 46721 triangles. The polynomial degree is set to N = 8 and all five faults are also approximated with a degree 8 polynomial. We note that we ran the scenario for on-fault resolutions $h_f \in \{4 \text{ km}, 2 \text{ km}, 1 \text{ km}, 0.5 \text{ km}\}$. Going from $h_f = 2$ to 0.5 km there is little difference in the number of events, the timing of events, and the peak slip rate.

Our exemplary results in Figs 14(b) and (c) illustrate 1400 yr of slip and slip-rate evolution on the main low-angle normal fault and all four curved splay faults in response to steady tectonic loading. Note, that we here do not omit a potential 'spin-up phase', and thus, the shown early events may not be fully representative of the longer-term behaviour. We observe complex slip evolution and fault interaction throughout the seismic cycle expressed in irregular fast and slow events occurring on the splay faults while the main fault predominantly creeps at plate rate. While we here assume mostly uniform initial conditions (in all parameters besides *a*), a more variable setup for example in normal stress may yield both megathrust and splay fault rupture.

The shortest splay, closest to the main fault at 30 km, shows regular low-slip-rate events and produces a single fast earthquake. It accumulates roughly half of the long-term slip compared to the two largest splays. For the splays in 50 and 70 km distance to the surface expression of the main fault, we find preliminary indications for slip, slip rate and recurrence rate correlating with splay fault length. Such apparent correlation breaks down for the largest splay, set furthest apart from the main fault at 90 km distance, which hosts regular assismic transients and seismic events which magnitude appears to decrease over time. It is offset by roughly the same amount of slip as its shorter neighbouring splay fault. In our exemplary model setup, all splays are able to co-seismically slip up to the free surface. Aseismic transients appear at 90 km and less pronounced at 70 km distance only after initial earthquakes on those splays. Interestingly, we observe rather complex splay fault coupling (due to static and quasi-dynamic stress transfer). For example, an earthquake rupturing the shortest splay after \approx 1000 yr, triggers the highest co-seismic slip rate on the longest, furthest away splay fault. While we refrain from further quantitative analysis here due to the demonstration scope of this example, we note that future work can readily use our setup for geophysical analysis of the seismic cycle in low-angle normal fault as well as megathrust-splay fault networks by adapting the loading conditions.

In the scenario presented here, we leave an arbitrarily small gap between the main fault and the splays following an equivalent strategy established for branching fault geometries in dynamic earthquake rupture code verification exercises (Pelties *et al.* 2014; Harris *et al.* 2018). We note that whilst intersecting faults can be handled by our elasticity solver (Section 8.2), when running our 2-D SEAS model including fault triple junctions ($h_f = 2 \text{ km}$), we observe that shortly after t = 10 yr the normal stress becomes tensile. Inspecting the results in Fig. 15(a) reveals that strain becomes very large at the connection point between a splay and the main fault. This is due to a local switch of the sign of the change in traction at these points, which we indicate by red lines showing the change in shear traction in the direction of the normal of the main fault. We might overcome this issue by future implementation of appropriate jump conditions for tensile stresses (Day *et al.* 2005) or accounting for off-fault inelastic deformation (Templeton & Rice 2008; Gabriel *et al.* 2013; Erickson *et al.* 2017; Wollherr *et al.* 2018; Mia *et al.* 2021). We also note certain similarities of our results to the boundary element analysis of the effect of fault curvature on fault stresses presented in Romanet & Ozawa (2022) motivating further comparative analysis of BEM and DG methods.

We repeated the scenario with non-intersecting faults on an affine mesh (degree 1) in which the splay faults are approximated by linear elements. Fig. 15(b) shows artefacts in both the strain and traction (the latter indicated as red lines). These artefacts coincide with the vertices, indicating that they are caused by the abrupt change in angle of the fault normal. The rate and state simulation aborts after t = 100 yr due to unrealistically high stresses likely caused by the ODE solver becoming unstable. In comparison, when using a curvilinear mesh, we observe no artefacts in strain and traction at t = 100 yr (see Fig. 15c).

Lastly, we report the application runtimes on a dual socket AMD EPYC 7662 server using 120 processes, the fifth-order Dormand–Prince scheme with six stages, and the linear solver combining p-multigrid and algebraic multigrid. For the $h_f = 4$ km mesh, computing the discrete Green's function took approximately 0.8 hr and the time integration took 1.5 hr. In comparison, the run without discrete Green's function took 31 hr showing that the pre-computation step clearly pays off for this application. Computation of the discrete Green's function on the finest mesh ($h_f = 0.5$ km), using the same configuration and hardware, took 1.1 d and time integration took 0.9 d for a total of 963 676 time steps and 45474 time-step rejections.

8.2 A 3-D multifault scenario of instantaneous displacement due to the 2019 Ridgecrest earthquake sequence

In our next, kinematic elastostatic demonstration example, we consider an idealized instantaneous displacement scenario due to the multifault 2019 Ridgecrest, California earthquake sequence. This foreshock—main shock pair of large events occurred on a segmented antithetic fault network dominated by northwest-trending right-lateral and northeast-trending left-lateral strike-slip (e.g. Ross *et al.* 2019; Chen *et al.* 2020; Fialko & Jin 2021). The Ridgecrest sequence has produced vigorous post-seismic crustal motions (e.g. Dorsett *et al.* 2019; Pollitz *et al.* 2021). Modelling viscous relaxation requires accurate initial conditions, such as provided in the following example.

Our demonstration model considers (simplified) distinct strike-slip displacements accumulated during both events across six geometrically complex and intersecting fault segments, inspired by data-constrained 3-D dynamic rupture modelling of both events (Taufiqurrahman *et al.* 2022). In difference to the previous example, no fault triple junctions are considered here. We note that the problem under consideration is purely elastic and does not involve a fault constitutive law. That is we prescribe the fault slip on each fault segment. Hence, the problem is

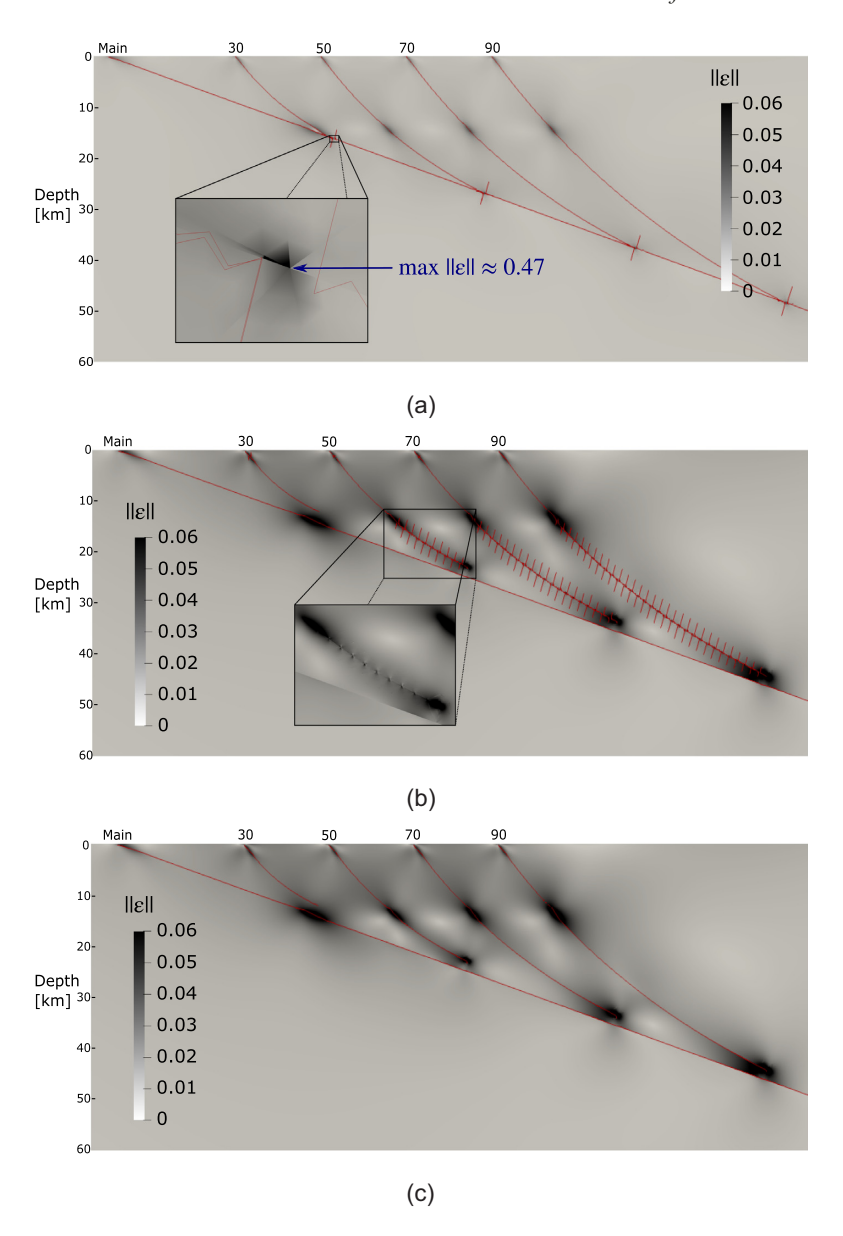


Figure 15. Variations of the scenario with four curved splay faults. The Frobenius norm of the strain tensor is shown in black and white. Red lines are used to visualize different types of artefacts. For illustration purposes, these red lines connect mesh coordinates moved according to the change in shear traction in the normal direction of the faults. Note the effect of changes in (a) and (b) at 15 km depth. The on-fault mesh size is $h_f = 2$ km in all models. (a) Curvilinear mesh, connected faults. Splays connected to the main fault thereby forming a triple junction cause large strain at the intersection point. We find that the elasticity solver can handle these intersections of splay and main fault, but the rate and state solver fails due to large strain at the intersection points shown at t = 10 yr, as highlighted in the inset. Red lines show the change in shear traction in the direction of the normal of the main fault. (b) Affine mesh, unconnected faults. Artefacts in strain and traction are visible using an affine mesh and unconnected faults due to the linear approximation of the boundary, as highlighted in the inset. The use of affine meshes causes these severe artefacts in traction and strain, shown at (t = 100 yr). The rate and state solver fails, too. Red lines show the change in shear traction in the direction of the normal of the respective splay and main faults. (c) Non-intersecting faults with curvilinear meshes causes no visible artefacts (t = 100 yr) and is well handled by the elasticity and rate state solver.

independent of time. The example geometry of the Ridgecrest fault system has been simplified from integrated geodetic InSAR data, satellite imagery, relocated seismicity and selected focal mechanisms (Carena & Suppe 2002; Taufiqurrahman *et al.* 2022).

The model domain is $130 \text{ km} \times 135 \text{ km}$ in map view and 50 km deep. The fault network is centrally located within the model domain. All faults are assumed to be purely vertical and extending to a depth of 11 km (DuRoss *et al.* 2020). The domain size is chosen such that the faults are $\sim 50 \text{ km}$ from the side walls and 39 km from the lower boundary. The geometry of each fault is represented by a Bezier spline provided by Gmsh's BSpline geometry object. We impose zero displacement (all components) on the lateral walls, and on the upper and lower boundaries we impose zero stress (in both tangential and normal directions). We drive displacement in the domain by imposing slip along each of the six fault segments. Along each fault, we prescribe constant slip to produce either pure left- or right-lateral (depending on the fault) strike-slip motion. Faults with strike tending NW-SE are assumed to slip right-lateral, while those tending NE-SW are taken to be left-lateral (Barnhart *et al.* 2020). A schematic of the fault system with the imposed slip boundary conditions is shown in Fig. 16. We further

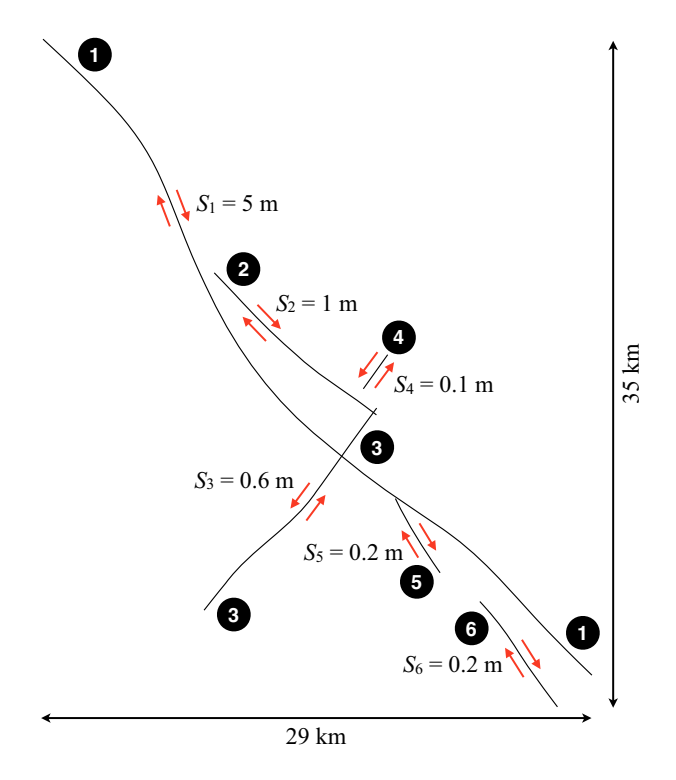


Figure 16. Schematic of the Ridgecrest fault system geometry, the sense of slip (red arrows) and values for the imposed strike-slip (S_k) on each fault segment k = 1, ..., 6 in the instantaneous, kinematic elastostatic model. The absolute values used for S_k (i.e. ignoring the sense of slip) were 5.0, 1.0, 0.6, 0.1, 0.2 and 0.2 m.

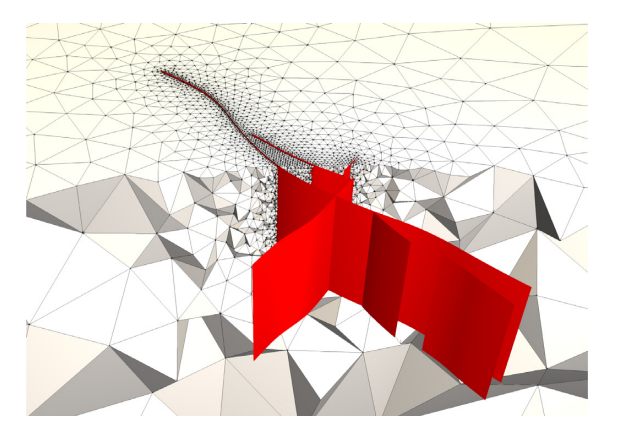


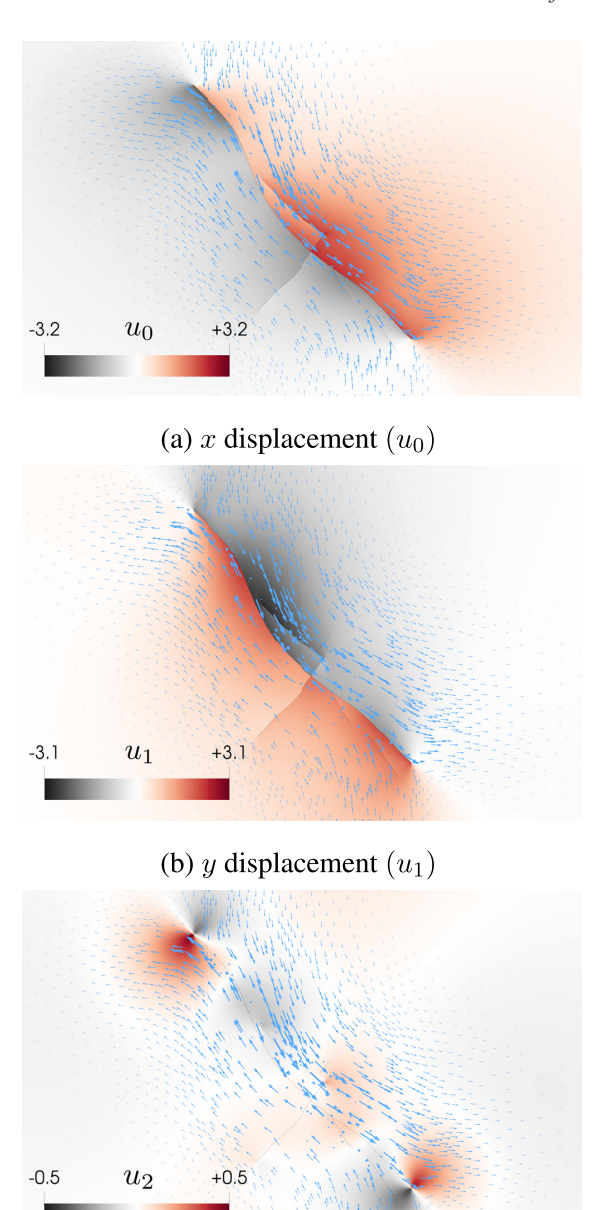
Figure 17. Close up and cut-away of the unstructured tetrahedral mesh used for the Ridgecrest example. The local refinement near the fault results in element edge lengths of 250 m. Away from the fault, the element edge length is coarsened up to a value of 20 km at the domain boundary. The mesh contained a total of 421 154 tetrahedra.

assume that the material is homogeneous with a Poisson ratio of $\nu=0.25$ and shear modulus $\mu=36$ GPa.

The mesh is constructed such that the spatial resolution (element edge length) on the faults is 250 m. We further specified that the spatial resolution on the domain boundaries be 20 km. With these specifications, the mesh generated contained 421 154 tetrahedra. A zoom (with cut-away) of the local mesh refinement near the fault system is shown in Fig. 17. In all experiments, we used the multigrid pre-conditioner described in Section 4.6. For simulations employing N = 1 (the case where polynomial coarsening cannot be invoked), the multigrid pre-conditioner reduces to using the algebraic multigrid package GAMG from PETSc.

The instantaneous displacement obtained using a polynomial of degree N = 3 for the displacement unknown and a non-affine mesh geometry with polynomial degree N = 2 is shown in Fig. 18. Due to the imposed values of slip with $S_1 > S_k$, k = 2, ..., 6, the displacement is primarily dominated by the slip from segment S_1 (see Fig. 16). We note that despite the simplicity in terms of initial slip conditions of our demonstration model, the resulting displacements are in overall agreement (qualitatively) with more advanced inferences (e.g. Fialko & Jin 2021).

The discontinuous nature of the displacement approximation is apparent when inspecting the horizontal components u_0 , u_1 (Figs 18a and b). This is expected and consistent with the imposed slip boundary conditions. What is note worthy is that no numerical artefacts appear at the intersecting points of segments S_3 – S_1 and S_2 – S_3 . In contrast, the vertical component of displacement is nearly continuous due to the



(c) z displacement (u_2)

Figure 18. Displacement field in the vicinity of the fault network. (a) and (b) Horizontal components (x, y) respectively) of the displacement. (c) Vertical component of the displacement field. All panels are overlaid with vectors denoting the horizontal components of the displacement field (u_0, u_1) . The faults are indicated by the thin black lines.

purely vertical fault orientation, homogeneous material properties and the pure strike-slip loading. Several components of the displacement gradient are shown in Fig. 19. In the upper panels (a), a low-degree polynomial was used for the displacement (N = 1) with an affine mesh. The lower panels (b) employed a displacement polynomial of N = 3 with a non-affine geometry representation using N = 2. For the N = 1 scenario, the slip vector imposed is defined such that it is tangential to the affine cell facets which approximate the fault boundary. In the high-order scenario, since the fault is discretized via a curvilinear representation, the slip imposed is tangential to the Bezier spline line used to represent the fault geometry.

Comparing the gradient fields between (a) and (b) we note that while the discontinuities are captured by the low-order displacement solution $(u_{0,x}, u_{0,y}, u_{0,z})$ significant numerical oscillations close to the fault (thin black line) are apparent. These oscillations vanish when using the higher degree displacement and geometry representation.

It is also striking that the low-order discretization is quite inaccurate in approximating the smooth field $u_{0,z}$. This is partially exaggerated by the fact that we constructed the mesh with coarse resolution off-fault; regardless, the benefits of using high-order approximations is evident: The high-order simulations resolve the singularity in the strain tensor which occurs at the end of each fault. While such singularities are the result of our idealized and somewhat unphysical model (i.e. the slip does not taper off towards the end of the fault) our exemplary results

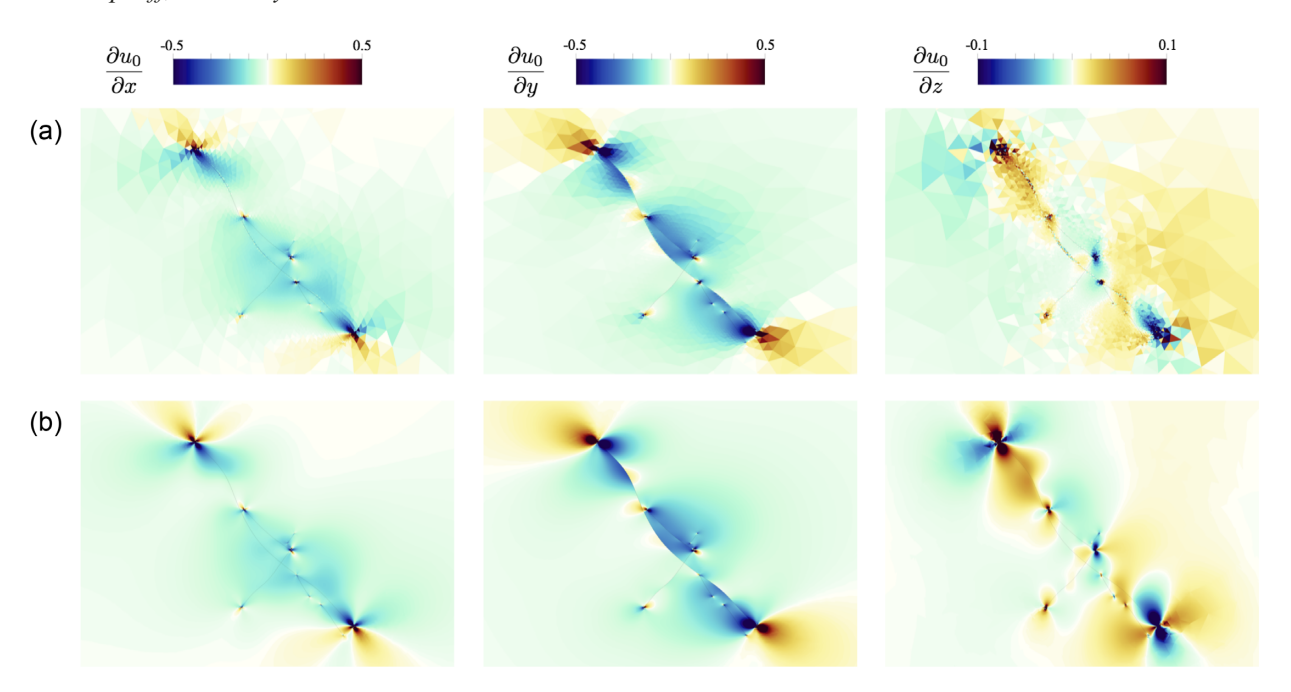


Figure 19. Gradient of the x-component of displacement (u_0) (x, y)—horizontal directions and z—vertical direction) in the vicinity of the fault network using different polynomial approximations. (a) u_h approximated with polynomial degree N = 1 over an affine mesh (fault geometry given by N = 1). (b) u_h approximated with polynomial degree N = 3 on a non-affine mesh with the fault geometry approximated by a polynomial of degree N = 2. The faults are indicated by the thin black lines.

demonstrate that the DG method is robust with respect to such loading conditions which might occur (and be physically meaningful): (i) when a fault intersects the free surface or terminates at a material interface with increased rigidity; (ii) when two faults intersect each other and (iii) at the location of a fault branch. Additionally we highlight that no special treatment was required to accommodate the fault intersections (i.e. between segments 1–3 and segments 2–3)—the DG solution, and its gradient (and, thus, strain), is well behaved at these locations.

9 DISCUSSION

In the following, we discuss the numerical results with respect to high-order convergence, give a qualitative comparison to the BEM, and describe how an extension to a fully dynamic SEAS modelling method might be obtained.

9.1 A high-order method for seismic cycling problems

We measure high-order convergence rates for elastostatic problems with a slip boundary condition, curved boundary, heterogeneous material parameters and for the time-dependent manufactured SEAS problem (Sections 7.1 and 7.2). For smooth problems, the high-order convergence pays off as the error decays much quicker in comparison to low-order rates (see the discussion in Section 7.2 and Fig. 8).

A requirement for high-order convergence is that the solution is sufficiently smooth, meaning that higher-order (weak) derivatives exist. We see in Fig. 4 that the convergence order is limited to 0.5 in the $|\cdot|_{1,h}$ semi-norm, due to a singularity at the origin in the second derivative for the case $\gamma = 0.5$. Therefore, the results in Fig. 8 model only the case ideal for high-order methods. In actual SEAS problems, the smoothness of the solution is unknown.

For non-smooth solutions, we observe that the error is still reduced by a constant factor when comparing a higher-order method to a lower-order method [see Wollherr *et al.*'s (2018) discussion for dynamic rupture problems], thus the additional degrees of freedom per element of the higher-order method are not in vain. Moreover, in combination with unstructured meshes we can locally refine the mesh. That is, small mesh sizes can be used in non-smooth regions while large mesh sizes are sufficient in smooth regions, see Fig. 10.

9.2 A qualitative comparison of DG versus BEM

The use of boundary integral equations is widespread in the SEAS community (Lapusta *et al.* 2000; Lapusta & Liu 2009; Liu & Rice 2005; Segall & Bradley 2012; Bradley 2014; Li & Liu 2016, 2017; Luo *et al.* 2017; Barbot 2019) and is also used in earlier work (e.g. Rice 1993). Here, we qualitatively compare the presented DG method to BEM for SEAS applications.

We first recall background and definitions of the BEM. For elastostatics in homogeneous and isotropic media, a necessary ingredient is the problem

$$\mu \frac{\partial^2 E_{ij}(\mathbf{x}', \mathbf{x})}{\partial x_k \partial x_k} + (\lambda + \mu) \frac{\partial^2 E_{kj}(\mathbf{x}', \mathbf{x})}{\partial x_k \partial x_i} = -\delta(\mathbf{x}' - \mathbf{x}) \delta_{ij}. \tag{89}$$

The tensor E that solves eq. (89) is called the fundamental solution or Kelvin's solution and is well known (Chen & Zhou 2010). The columns of E are interpreted as the displacement at x' due to a point force at x. From the fundamental solution one obtains the Betti–Somigliana equation (Chen & Zhou 2010), that is, for any internal point $x' \in \Omega$, we have

$$u_i(\mathbf{x}') = \int_{\partial\Omega} E_{ij}(\mathbf{x}', \mathbf{x})[t_j(\mathbf{u})](\mathbf{x}) - \tilde{T}_{ij}(\mathbf{x}', \mathbf{x})u_j(\mathbf{x}) \,\mathrm{d}s_{\mathbf{x}},\tag{90}$$

where t is the traction vector given u and the jth column of \tilde{T} is the traction vector given the jth column of E. Eq. (90) is the basis for deriving BEMs with slip boundary condition (e.g. Portela *et al.* 1992), but the details are not important for this discussion.

Inspecting eq. (90) reveals that we need both Dirichlet and Neumann data on the boundary in order to compute u. As we typically know either one or the other, eq. (90) can be slightly adapted such that it is valid for $x' \in \partial \Omega$ (Portela *et al.* 1992; Chen & Zhou 2010). Then we can discretize the boundary and solve the boundary integral equations for the discrete traction given Dirichlet data (or vice versa when Neumann data are given).

Eventually, both the DG method and the BEM require the solution to a linear system $A\underline{u} = b$, although the matrices A are quite different. For DG, A is *sparse* and, assuming a uniform grid, the number of degrees of freedom scales with n_1^D , where n_1 is the number of line elements. For BEM, A is *dense* and the number of degrees of freedom scales with n_1^{D-1} , because only the boundary needs to be discretized. Recalling that the complexity of exactly solving (e.g by LU factorization) an $n \times n$ sparse linear system is $\mathcal{O}(n^2)$ whilst the complexity for an $n \times n$ dense linear system is $\mathcal{O}(n^3)$, we can estimate a complexity of $\mathcal{O}(n_1^{2D})$ for DG and a complexity of $\mathcal{O}(n_1^{3(D-1)})$ for BEM. That is, we observe that BEM has a lower complexity in 2-D, but actually the complexity is identical in 3-D, at least using this simple estimate.

In the previous paragraph, we provided pessimistic bounds which would result from straightforward implementations of the DG method and BEM. Specializations of specific components of each method exist which reduce the algorithmic complexity and potentially alter the cost of each approach. We outline several enhancements below:

- (i) The complexity of solving the sparse DG system can be reduced to $\mathcal{O}(n)$ when iterative solvers employing multigrid are used. However, in practice achieving perfect $\mathcal{O}(n)$ scaling is somewhat problem dependent and hard to achieve in a consistent manner across a wide range of polynomial degrees (e.g. from N = 2 to 8).
- (ii) For BEM, an H-matrix approximation (Bradley 2014; Sato & Ando 2021; Ozawa *et al.* 2021) might reduce the storage and solve cost (Hackbusch & Khoromskij 2000). The H-matrix approach is of $\mathcal{O}(n \log n)$.
- (iii) The cost of evaluating the integral operator (i.e. a matrix-vector product) required by integral methods can be reduced to $\mathcal{O}(n)$ using the fast-multipole method (FMM, Rokhlin 1985; Greengard & Rokhlin 1987; Carrier *et al.* 1988; Romanet *et al.* 2018). Additionally, large-scale parallel implementations of FMM exist (Cruz *et al.* 2011; Yokota *et al.* 2011). We note that while FMM provides fast application of the kernels, it does not define a 'solve' (e.g. $A\underline{u} = b$). Hence when an FMM–BEM formulation requires the solution of a linear system, a pre-conditioner will be required to reduce the time complexity. In addition, the required multipole expansions are demanding (e.g. Gimbutas & Greengard 2016) and have not yet been applied to in-plane static or fully dynamic SEAS problems.
- (iv) Using the approach of the spectral BIM, the cost of evaluating the integral operator can be reduced to $\mathcal{O}(n \log n)$ (per fault segment) as stress interactions are evaluated in the Fourier domain and these computations can exploit an FFT (Geubelle & Rice 1995; Perrin *et al.* 1995; Bouchon & Streiff 1997; Lapusta & Liu 2009; Barbot 2021; Romanet & Ozawa 2022). Note that this specialization does limit the methods applicability to planar faults. Similarly to FMM (above), this fast integral operator evaluation does not replace the need for a solve.

In practice, one needs to consider many more aspects, e.g. which parts of the method can be parallelized [Amdahl's (1967) law], what are the memory requirements, or whether the method is suitable for current hardware architectures. We conclude that based on above considerations a fair comparison of DG and BEM is rendered inherently application-specific and it is thus not *a priori* obvious which method will yield the optimal time-to-solution.

There is, however, a common approximation which makes BEM very cost-effective for specific model setups. Assume that Dirichlet data is given and we are missing Neumann data. Further assume that we can find a tensor field G (i.e. a Green's function) such that G is a fundamental solution on Ω and $G_{ij} = 0$ if $\mathbf{x} \in \partial \Omega$. Then the first term in eq. (90) vanishes and the Neumann data are not required anymore such that \mathbf{u} is computed just by integration. In a discrete setting, the solution is thus obtained by (dense) matrix-vector multiplication only. Hence for a single Green's function, this multiplication has a time complexity of $\mathcal{O}(n^2)$. As mentioned earlier, this can be reduced in general to $\mathcal{O}(n)$ using FMM, or when applicable, to $\mathcal{O}(n \log n)$ via FFT. The use of analytical Green's function is widely adopted in the SEAS community [Lapusta & Liu (2009, eq. 5); Liu & Rice (2005, eq. 1); Li & Liu (2016, eq. 5); Segall & Bradley (2012, eq. 1); Barbot (2019, eq. 8)].

The difficulty in the analytical Green's function approach lies in the dependence of the Green's function on the boundary. Including topography, non-homogeneous media or nonlinear rheologies is difficult. While analytical Green's functions for a single planar fault in the elastic half-space are known (Mindlin 1936; Okada 1992), as well as those for multiple parallel faults in the elastic half-space (Barbot 2021) and for the 3-D Lamb's problem (Feng & Zhang 2018), finding analytical Green's function for more complex model setups is a formidable

task. Thus, in the following we assume that the analytical Green's function approach does not generalize to arbitrarily complex models and one has to resort to BEM, which involves the solution of a large and dense system of equations.

The computational cost of a time step using the discrete Green's function, see Section 6, is comparable to the cost of a time step using analytical Green's function, because only matrix multiplication is needed in both cases. Clearly, the discrete Green's function is expensive to obtain, as a linear system needs to be solved for every degree of freedom on-fault, but they may be computed for any fault geometry, fault network, material heterogeneity described by a linear constitutive model and any Dirichlet or Neumann (e.g. free-surface) boundary condition. Computing the discrete Green's functions is an embarrassingly parallel problem—that is, each discrete Green's function can be computed independently of the others. We further note that a future quantitative comparison of BEM and DG will be interesting, specifically addressing the challenges of complex fault geometries (e.g. Sato et al. 2020).

9.3 Extension to a fully dynamic method

In this work, we adopt the quasi-dynamic approach and neglect inertia. We see this as the first step towards a future SIPG implementation of the fully dynamic approach. In particular, the bilinear operator of the SIPG method can be directly employed in a wave propagation—that is, fully dynamic—scheme (Mazzieri *et al.* 2013). Moreover, the linear solvers we develop for the quasi-dynamic approach can be readily adapted for implicit time stepping in a fully dynamic model.

The extension of the SIPG method for elastostatics to wave propagation problems is straightforward. The elastodynamic equations are given by

$$\rho \frac{\partial^2 u_i}{\partial t^2} - \frac{\partial \sigma_{ij}(\mathbf{u})}{\partial x_i} = f_i. \tag{91}$$

The SIPG method for the above equation is formulated as following (Grote *et al.* 2006; Mazzieri *et al.* 2013): find $u_h \in [0, t_{end}] \times V_h \to \mathbb{R}$ such that

$$\int_{\Omega} \rho \mathbf{v} \cdot \frac{\partial^2 \mathbf{u}_h}{\partial t^2} \, \mathrm{d}\mathbf{x} + a(\mathbf{u}_h, \mathbf{v}) = L(\mathbf{v}),\tag{92}$$

for all $v \in V_h$, $t \in [0, t_{end}]$, where the bilinear form $a(\cdot, \cdot)$ and the linear form $L(\cdot)$ are defined in eq. (25). Written in terms of linear algebra, we have

$$M\frac{\partial^2 \underline{u}}{\partial t^2} + A\underline{u} = b, \tag{93}$$

where A and b are constructed identically as in Section 4, and M is the block-diagonal mass matrix weighted with the density ρ . Low-storage schemes for the inverse mass matrix are discussed by Warburton (2013) and Chan *et al.* (2017) for curvilinear meshes.

Explicit time stepping is subject to a CFL condition (Grote *et al.* 2006), rendering explicit time stepping infeasible for the time spans considered in SEAS models. One might circumvent the time-step restrictions by switching between fully dynamic solvers in the co-seismic phase and quasi-dynamic solvers in the aseismic phase (Kaneko *et al.* 2011; Galvez *et al.* 2020; Liu *et al.* 2020). Using the same finite-element space for both solvers is convenient as there is no need for interpolation.

Another possibility might be to treat the elastodynamic equation implicitly. For illustration, the classic Newmark scheme leads to the linear system that needs to be solved in every time step (Hughes 2000, eq. 9.1.12)

$$(\mathbf{M} + \beta \Delta t^2 \mathbf{A}) \mathbf{a}^{n+1} = \mathbf{b}^{n+1} - A \widetilde{\mathbf{u}}^{n+1}, \tag{94}$$

where the predictor $\underline{\tilde{u}}^{n+1}$ depends only on time step n. Here, linear solvers developed for the elastostatic problem can likely be reused, for example, the multigrid solver, (Section 4.6). Whether such a scheme yields time steps reasonable for SEAS models remains to be explored.

10 CONCLUSIONS

We present an SIPG method to perform quasi-dynamic simulations of SEAS. This is the first time a DG method is applied and thoroughly analysed in the context of SEAS simulations, which motivates several novel methodological developments in the context of SIPG, elasticity problems and embedded faults governed by rate-and-state friction. Choosing the SIPG method has several merits: it is a provably stable DG discretization for elliptic problems, can be naturally extended to incorporate embedded faults and defines symmetric positive definite discrete operators which are suitable to use with pre-conditioned iterative solvers. We see one of the most important contributions of this work in presenting how to unify these ingredients and demonstrating their benefits for SEAS simulations.

Through an extensive suite of analytic, manufactured, and code-verification examples for elastostatic and seismic cycle problems, we characterize the solution behaviour of our SIPG discretization. Our verification suite demonstrates that high-order convergence of the discrete solution can be achieved in space (and time) for both elastostatic and quasi-dynamic SEAS problems when the polynomial degree of the displacement is increased. We demonstrate that high-order convergence is maintained when either the material properties vary within a cell, or the fault or exterior boundary is curved provided both the coefficients and geometry are discretized with the same polynomial degree as used for the displacement. We exploit the curvilinear geometry representation in two demonstrator models to further elucidate the importance

of using curvilinear fault representations, compared with piecewise linear approximations (affine), when accurate stresses (or displacement gradients) are required on-fault.

We provide an open-source reference implementation, *Tandem*, which supports both 2-D and 3-D simulations of elastostatic and quasi-dynamic seismic cycle applications, accounting for geological heterogeneities and geometric complexity and arbitrary polynomial degree for the displacement, material properties and geometry. *Tandem* natively supports node-level and distributed memory parallelism. With awareness of the high computational demands of SEAS simulations, our reference implementation exploits modern, efficient libraries for the DG kernels and linear algebra, solver and pre-conditioner support. Further flexibility and efficiency is provided by optionally defining the displacement evaluation via discrete Green's functions, which are evaluated and checkpoint once in a pre-computation stage using algorithmically optimal and scalable sparse parallel solvers and pre-conditioners. This strategy appears to exploit advantages of both the boundary integral and volumetric methods and is an interesting avenue to pursue in the future for extreme scale 3-D SEAS simulations.

ACKNOWLEDGMENTS

We thank Ryosuke Ando and Pierre Romanet for their constructive and thoughtful comments which improved the manuscript. We thank Louise Alexander and Bertrand Rouet-Leduc for handling our manuscript. This work has received funding from the European Research Council (ERC) under the European Union's Horizon 2020 research and innovation programme [*TEAR* (www.tear-erc.eu), grant no. 852992, and additional support from *ChEESE*, grant no. 823844, *DT-GEO*, grant no. 101058129 and *Geo-INQUIRE*, grant no. 101058518].

This work has also received support by the National Science Foundation (NSF grant no. EAR-2121568), the Southern California Earthquake Center (SCEC grants no. 21112, 22135) and the German Research Foundation (DFG grant no. GA 2465/2-1).

The authors gratefully acknowledge the Gauss Centre for Supercomputing e.V. (www.gauss-centre.eu) for providing computing time on the GCS Supercomputer SuperMUC-NG at Leibniz Supercomputing Centre (www.lrz.de through project *pr63qo*). Additional computing resources were provided by the Institute of Geophysics of LMU Munich (Oeser *et al.* 2006).

We thank James Biemiller, Taufiqurrahman, Nico Schliwa and Duo Li for helpful discussion of demonstration examples.

AUTHOR CONTRIBUTION STATEMENT

Project conceptualization: AAG and DAM. Mathematical development: CU and DAM. Software development: CU and DAM. Conceived and designed the experiments: CU, DAM and AAG. Performed the experiments: CU and DAM. Analysed the results: CU, DAM and AAG. Dam and AAG. Dam and CU. Procured funding, project administration and supervision: AAG.

DATA AVAILABILITY

The Jupyter notebook, setups, and data are openly available in Zenodo at https://doi.org/10.5281/zenodo.5796104. Instructions on how to repeat the presented numerical experiments are also contained in the Zenodo data set. The code is available in GitHub at https://github.com/TEAR-ERC/tandem. Instructions on how to build and run the code are available at https://tandem.readthedocs.io. The setups in Section 7 are alternatively available from https://github.com/TEAR-ERC/tandem/blob/v1.0/examples/. The Jupyter notebook which details the steps to construct the solution in Section 7.1.1 is alternatively available at https://github.com/TEAR-ERC/tandem/blob/main/notebooks/wedge.ipynb.

REFERENCES

- Aagaard, B.T., Knepley, M.G. & Williams, C.A., 2013. A domain decomposition approach to implementing fault slip in finite-element models of quasi-static and dynamic crustal deformation, *J. geophys. Res.: Solid Earth*, 118(6), 3059–3079.
- Abdelmeguid, M., Ma, X. & Elbanna, A., 2019. A novel hybrid finite element-spectral boundary integral scheme for modeling earthquake cycles: Application to rate and state faults with low-velocity zones, J. geophys. Res.: Solid Earth, 124(12), 12854–12881.
- Abhyankar, S., Brown, J., Constantinescu, E.M., Ghosh, D., Smith, B.F. & Zhang, H., 2018. PETSc/TS: a modern scalable ODE/DAE solver library, Tech. rep., Argonne National Laboratory, preprint (arXiv:1806.01437).
- Allison, K.L. & Dunham, E.M., 2018. Earthquake cycle simulations with rate-and-state friction and power-law viscoelasticity, *Tectonophysics*, 733, 232–256.
- Almquist, M. & Dunham, E.M., 2021. Elastic wave propagation in anisotropic solids using energy-stable finite differences with weakly enforced boundary and interface conditions, *J. Comput. Phys.*, 424, 109842, doi:10.1016/j.jcp.2020.109842.

- Amdahl, G.M., 1967. Validity of the single processor approach to achieving large scale computing capabilities, in *Proceedings of the April 18-20, 1967, Spring Joint Computer Conference, AFIPS '67*, pp. 483–485, Association for Computing Machinery, New York, NY, USA.
- Amestoy, P.R., Duff, I.S., L'Excellent, J.-Y. & Koster, J., 2001. A fully asynchronous multifrontal solver using distributed dynamic scheduling, *SIAM J. Matrix Anal. Appl.*, **23**(1), 15–41.
- Amestoy, P.R., Buttari, A., L'Excellent, J.-Y. & Mary, T., 2019. Performance and scalability of the block low-rank multifrontal factorization on multicore architectures, ACM Trans. Math. Softw., 45(1), doi:10.1145/3242094.
- Ampuero, J.-P. & Rubin, A.M., 2008. Earthquake nucleation on rate and state faults—aging and slip laws, *J. geophys. Res.*, 113, B01302, doi:10.1029/2007JB005082.
- Anderlini, L., Serpelloni, E. & Belardinelli, M.E., 2016. Creep and locking of a low-angle normal fault: insights from the Altotiberina fault in the Northern Apennines (Italy), *Geophys. Res. Lett.*, 43(9), 4321–4329.
- Ando, R. & Kaneko, Y., 2018. Dynamic rupture simulation reproduces spontaneous multifault rupture and arrest during the 2016 Mw 7.9 Kaikoura earthquake, *Geophys. Res. Lett.*, 45(23), 12875–12883.

- Andrews, D., 1976a. Rupture velocity of plane strain shear cracks, J. geophys. Res., 81(32), 5679–5687.
- Andrews, D., 1976b. Rupture propagation with finite stress in antiplane strain, *J. geophys. Res.*, **81**(20), 3575–3582.
- Andrews, D., 1989. Mechanics of fault junctions, J. geophys. Res.: Solid Earth, 94(B7), 9389–9397.
- Antonietti, P.F. & Houston, P., 2011. A class of domain decomposition preconditioners for hp-discontinuous Galerkin finite element methods, J. Sci. Comput., 46(1), 124–149.
- Arioli, M., Demmel, J.W. & Duff, I.S., 1989. Solving sparse linear systems with sparse backward error, SIAM J. Matrix Anal. Appl., 10(2), 165–190.
- Arndt, D., Fehn, N., Kanschat, G., Kormann, K., Kronbichler, M., Munch, P., Wall, W.A. & Witte, J., 2020. ExaDG: high-order discontinuous Galerkin for the exa-scale, in *Software for Exascale Computing-SPPEXA 2016-*2019, pp. 189–224, Springer, Cham.
- Arnold, D.N., Brezzi, F., Cockburn, B. & Marini, L.D., 2002. Unified analysis of discontinuous Galerkin methods for elliptic problems, SIAM J. Numer. Anal., 39(5), 1749–1779.
- Aslam, K.S., Thomas, A.M. & Melgar, D., 2021. The effect of fore-arc deformation on shallow earthquake rupture behavior in the Cascadia subduction zone, *Geophys. Res. Lett.*, **48**(20), e2021GL093941, doi:10.1029/2021GL093941.
- Balay, S., Gropp, W.D., McInnes, L.C. & Smith, B.F., 1997. Efficient management of parallelism in object oriented numerical software libraries, in Modern Software Tools in Scientific Computing, pp. 163–202, Birkhäuser Press.
- Balay, S. et al., 2021a. PETSc users manual, Tech. Rep. ANL-95/11 Revision 3.15, Argonne National Laboratory.
- Balay, S. et al., 2021b. PETSc Web page, available at: https://petsc.org/.
- Barber, J.R., 2004. *Elasticity*, Kluwer Academic Publishers, 2nd edn.
- Barbot, S., 2019. Slow-slip, slow earthquakes, period-two cycles, full and partial ruptures, and deterministic chaos in a single asperity fault, *Tectonophysics*, **768**, 228171, doi:10.1016/j.tecto.2019.228171.
- Barbot, S., 2021. A spectral boundary-integral method for quasi-dynamic ruptures of multiple parallel faults, *Bull. seism. Soc. Am.*, 111(3), 1614– 1630.
- Barbot, S., Lapusta, N. & Avouac, J.-P., 2012. Under the hood of the earth-quake machine: toward predictive modeling of the seismic cycle, *Science*, 336(6082), 707–710.
- Barnhart, W.D., Gold, R.D. & Hollingsworth, J., 2020. Localized fault-zone dilatancy and surface inelasticity of the 2019 Ridgecrest earthquakes, *Nat. Geosci.*, 13(10), 699–704.
- Ben-Menahem, A., 1991. Four thousand years of seismicity along the Dead Sea rift, *J. geophys. Res.: Solid Earth*, **96**(B12), 20195–20216.
- Biemiller, J., Boulton, C., Wallace, L., Ellis, S., Little, T., Mizera, M., Niemeijer, A. & Lavier, L., 2020. Mechanical implications of creep and partial coupling on the world's fastest slipping low-angle normal fault in Southeastern Papua New Guinea, *J. geophys. Res.: Solid Earth*, **125**(10), e2020JB020117, doi:10.1029/2020JB020117.
- Biemiller, J., Gabriel, A.-A. & Ulrich, T., 2022. Dueling dynamics: competition between detachment rupture, splay faults, and off-fault damage, *Res. Sq.*, doi:10.21203/rs.3.rs-1650728/v1.
- Biemiller, J.B., Gabriel, A.-A. & Ulrich, T., 2021. The dynamics of unlikely slip: 3d modeling of low-angle normal fault rupture at the Mai'iu Fault, Papua New Guinea, *Earth Space Sci. Open Archive*, 36, doi:10.1002/essoar.10509373.1.
- Blanpied, M.L., Lockner, D.A. & Byerlee, J.D., 1991. Fault stability inferred from granite sliding experiments at hydrothermal conditions, *Geophys. Res. Lett.*, 18(4), 609–612.
- Bouchon, M. & Streiff, D., 1997. Propagation of a shear crack on a nonplanar fault: a method of calculation, Bull. seism. Soc. Am., 87(1), 61–66.
- Bradley, A.M., 2014. Software for efficient static dislocation-traction calculations in fault simulators, Seismol. Res. Lett., 85(6), 1358–1365.
- Brenner, S.C., 2004. Korn's inequalities for piecewise H¹ vector fields, Math. Comput., 73(247), 1067–1087.
- Brezzi, F. & Fortin, M., 1991. *Mixed and Hybrid Finite Element Methods*, Springer, New York, NY.

- Buiter, S.J. et al., 2016. Benchmarking numerical models of brittle thrust wedges, J. Struct. Geol., 92, 140–177.
- Carena, S. & Suppe, J., 2002. Three-dimensional imaging of active structures using earthquake aftershocks: the Northridge thrust, California, J. Struct. Geol., 24(4), 887–904.
- Carrier, J., Greengard, L. & Rokhlin, V., 1988. A fast adaptive multipole algorithm for particle simulations, SIAM J. Sci. Stat. Comput., 9(4), 669– 686
- Castillo, P., Cockburn, B., Perugia, I. & Schötzau, D., 2000. An a priori error analysis of the local discontinuous Galerkin method for elliptic problems, SIAM J. Numer. Anal., 38(5), 1676–1706.
- Chan, J., Hewett, R.J. & Warburton, T., 2017. Weight-adjusted discontinuous Galerkin methods: curvilinear meshes, SIAM J. Sci. Comput., 39(6), A2395–A2421
- Charrier, D.E., May, D.A. & Schnepp, S.M., 2017. Symmetric interior penalty discontinuous Galerkin discretizations and block preconditioning for heterogeneous Stokes flow, SIAM J. Sci. Comput., 39(6), B1021– B1042.
- Chen, G. & Zhou, J., 2010. Boundary Element Methods with Applications to Nonlinear Problems, Atlantis Press, 2nd edn.
- Chen, K., Avouac, J.-P., Aati, S., Milliner, C., Zheng, F. & Shi, C., 2020. Cascading and pulse-like ruptures during the 2019 Ridgecrest earth-quakes in the Eastern California Shear Zone, *Nat. Commun.*, 11(1), 22, doi:10.1038/s41467-019-13750-w.
- Cochard, A. & Madariaga, R., 1994. Dynamic faulting under rate-dependent friction, *Pure appl. Geophys.*, 142(3), 419–445.
- Cockburn, B. & Shu, C.W., 1989. TVB Runge-Kutta local projection discontinuous Galerkin finite element method for conservation laws II: general framework, *Math. Comput.*, 52, 411–435.
- Collettini, C., 2011. The mechanical paradox of low-angle normal faults: current understanding and open questions, *Tectonophysics*, 510(3), 253–268.
- Cruz, F.A., Knepley, M.G. & Barba, L.A., 2011. PetFMM—a dynamically load-balancing parallel fast multipole library, *Int. J. Numer. Methods Eng.*, **85**(4), 403–428.
- Day, S.M., Dalguer, L.A., Lapusta, N. & Liu, Y., 2005. Comparison of finite difference and boundary integral solutions to three-dimensional spontaneous rupture, *J. geophys. Res.: Solid Earth*, 110(B12), doi:10.1029/20 05JB003813.
- Dieterich, J.H., 1979. Modeling of rock friction: 1. Experimental results and constitutive equations, *J. geophys. Res.: Solid Earth*, **84**(B5), 2161–2168.
- Dieterich, J.H. & Kilgore, B.D., 1994. Direct observation of frictional contacts: new insights for state-dependent properties, *Pure appl. Geophys.*, **143**(1), 283–302.
- Dieterich, J.H., Richards-Dinger, K.B. & Kroll, K.A., 2015. Modeling injection-induced seismicity with the physics-based earthquake simulator RSQSim, Seismol. Res. Lett., 86(4), 1102–1109.
- Dorozhinskii, R. & Bader, M., 2021. Seissol on distributed Multi-GPU systems: CUDA code generation for the modal discontinuous Galerkin method, in *The International Conference on High Performance Computing in Asia-Pacific Region (HPC Asia 2021)*, Association for Computing Machinery, New York, NY, USA, pp. 69–82. doi:10.1145/3432261.3436 753.
- Dorsett, J., Johnson, K.M., Puel, S. & Becker, T.W., 2019. Postseismic deformation and stress evolution following the 2019 M7.1 and M6.4 Ridge-crest earthquakes, in AGU Fall Meeting Abstracts, Vol. 2019, pp. S31G–0500, available at: https://ui.adsabs.harvard.edu/abs/2019AGUFM.S31G-0500D/abstract.
- Dumbser, M. & Käser, M., 2006. An arbitrary high-order discontinuous Galerkin method for elastic waves on unstructured meshes II. The three-dimensional isotropic case, *Geophys. J. Int.*, **167**(1), 319–336.
- DuRoss, C.B. et al., 2020. Surface displacement distributions for the July 2019 Ridgecrest, California, earthquake ruptures, Bull. seism. Soc. Am., 110, 1400–1418.
- Duru, K. & Dunham, E.M., 2016. Dynamic earthquake rupture simulations on nonplanar faults embedded in 3D geometrically complex, heterogeneous elastic solids, *J. Comput. Phys.*, 305, 185–207.

- Duru, K., Rannabauer, L., Gabriel, A.-A., Ling, O. K.A., Igel, H. & Bader, M., 2022. A stable discontinuous Galerkin method for linear elastodynamics in 3D geometrically complex elastic solids using physics based numerical fluxes, *Comput. Methods Appl. Mech. Eng.*, 389, 114386, doi:10.1016/j.cma.2021.114386.
- Epshteyn, Y. & Rivière, B., 2007. Estimation of penalty parameters for symmetric interior penalty Galerkin methods, *J. Comput. Appl. Math.*, 206(2), 843–872.
- Erickson, B.A. & Dunham, E.M., 2014. An efficient numerical method for earthquake cycles in heterogeneous media: alternating sub-basin and surface-rupturing events on faults crossing a sedimentary basin, *J. geo-phys. Res.: Solid Earth*, 119(4), 3290–3316.
- Erickson, B.A., Dunham, E.M. & Khosravifar, A., 2017. A finite difference method for off-fault plasticity throughout the earthquake cycle, *J. Mech. Phys. Solids*, 109, 50–77.
- Erickson, B.A. et al., 2020. The community code verification exercise for simulating sequences of earthquakes and assismic slip (SEAS), Seismol. Res. Lett., 91(2A), 874–890.
- Erickson, B.A. et al., 2022. Incorporating Full Elastodynamic Effects and Dipping Fault Geometries in Community Code Verification Exercises for Simulations of Earthquake Sequences and Aseismic Slip (SEAS), preprint, doi:10.31223/X5NP87.
- Fehn, N., Munch, P., Wall, W.A. & Kronbichler, M., 2020. Hybrid multigrid methods for high-order discontinuous Galerkin discretizations, *J. Comput. Phys.*, 415, 109538, available at: https://www.sciencedirect.com/scie nce/article/pii/S0021999120303120, doi:10.1016/j.jcp.2020.109538.
- Feng, X. & Zhang, H., 2018. Exact closed-form solutions for Lamb's problem, Geophys. J. Int., 214(1), 444–459.
- Fialko, Y. & Jin, Z., 2021. Simple shear origin of the cross-faults ruptured in the 2019 Ridgecrest earthquake sequence, *Nat. Geosci.*, 14, 513–518, doi:10.1038/s41561-021-00758-5.
- Fletcher, J.M., Oskin, M.E. & Teran, O.J., 2016. The role of a keystone fault in triggering the complex El Mayor–Cucapah earthquake rupture, *Nat. Geosci.*, **9**(4), 303–307.
- Forsythe, G.E., Malcolm, M.A. & Moler, C.B., 1977. Computer Methods for Mathematical Computations, Prentice Hall.
- Gabriel, A.-A., Ampuero, J.-P., Dalguer, L.A. & Mai, P.M., 2013. Source properties of dynamic rupture pulses with off-fault plasticity, *J. geophys. Res.: Solid Earth*, **118**(8), 4117–4126.
- Galvez, P., Somerville, P., Petukhin, A., Ampuero, J.-P. & Peter, D., 2020. Earthquake cycle modelling of multi-segmented faults: dynamic rupture and ground motion simulation of the 1992 Mw 7.3 Landers earthquake, *Pure appl. Geophys.*, 177(5), 2163–2179.
- Gao, D., Wang, K., Insua, T.L., Sypus, M., Riedel, M. & Sun, T., 2018. Defining megathrust tsunami source scenarios for northernmost Cascadia, *Nat. Hazards*, 94(1), 445–469.
- Geubelle, P.H. & Rice, J.R., 1995. A spectral method for three-dimensional elastodynamic fracture problems, J. Mech. Phys. Solids, 43(11), 1791– 1824.
- Geuzaine, C. & Remacle, J.-F., 2009. Gmsh: a 3-D finite element mesh generator with built-in pre- and post-processing facilities, *Int. J. Numer. Methods Eng.*, 79(11), 1309–1331.
- Gimbutas, Z. & Greengard, L., 2016. A fast multipole method for the evaluation of elastostatic fields in a half-space with zero normal stress, Adv. Comput. Math., 42(1), 175–198.
- Greengard, L. & Rokhlin, V., 1987. A fast algorithm for particle simulations, J. Comput. Phys., 73(2), 325–348.
- Grote, M.J., Schneebeli, A. & Schötzau, D., 2006. Discontinuous Galerkin finite element method for the wave equation, SIAM J. Numer. Anal., 44(6), 2408–2431.
- Hackbusch, W. & Khoromskij, B., 2000. A sparse H-matrix arithmetic: general complexity estimates, J. Comput. Appl. Math., 125(1), 479–501.
- Harris, R.A. et al., 2018. A suite of exercises for verifying dynamic earth-quake rupture codes, Seismol. Res. Lett., 89(3), 1146–1162.
- Harris, R.A. et al., 2021. A geology and geodesy based model of dynamic earthquake rupture on the Rodgers Creek-Hayward-Calaveras fault system, California, J. geophys. Res.: Solid Earth, 126(3), e2020JB020577, doi:10.1029/2020JB020577.

- Heinecke, A. et al., 2014. Petascale high order dynamic rupture earthquake simulations on heterogeneous supercomputers, in SC'14: Proceedings of the International Conference for High Performance Computing, Networking, Storage and Analysis, pp. 3–14, IEEE.
- Hesthaven, J.S. & Warburton, T., 2008. Nodal Discontinuous Galerkin Methods, Springer, New York, USA.
- Hill, W. H. R. T.R., 1973. Triangular mesh methods for the neutron transport equation, Tech. Rep. LA-UR-73-479, Los Alamos National Laboratory, Los Alamos, New Mexico, USA.
- Hori, T., Agata, R., Ichimura, T., Fujita, K., Yamaguchi, T. & Iinuma, T., 2021. High-fidelity elastic Green's functions for subduction zone models consistent with the global standard geodetic reference system, *Earth Planets Space*, 73(1), 1–12.
- Hughes, T. J.R., 2000. The Finite Element Method: Linear Static and Dynamic Finite Element Analysis, Dover Publications, New York.
- Ikari, M.J., Marone, C., Saffer, D.M. & Kopf, A.J., 2013. Slip weakening as a mechanism for slow earthquakes, *Nat. Geosci.*, 6(6), 468–472.
- Jaśkowiec, J. & Sukumar, N., 2020. High-order cubature rules for tetrahedra, Int. J. Numer. Methods Eng., 121(11), 2418–2436.
- Jiang, J. et al., 2022. Community-driven code comparisons for threedimensional dynamic modeling of sequences of earthquakes and aseismic slip, J. geophys. Res.: Solid Earth, 127(3), e2021JB023519, doi:10.1029/ 2021JB023519.
- Johnen, A., Remacle, J.-F. & Geuzaine, C., 2013. Geometrical validity of curvilinear finite elements, J. Comput. Phys., 233, 359–372.
- Kaneko, Y., Ampuero, J.-P. & Lapusta, N., 2011. Spectral-element simulations of long-term fault slip: Effect of low-rigidity layers on earthquake-cycle dynamics, *J. geophys. Res.: Solid Earth*, 116(B10), doi:10.1029/2011JB008395.
- Karypis, G. & Kumar, V., 1998. A fast and high quality multilevel scheme for partitioning irregular graphs, SIAM J. Sci. Comput., 20(1), 359–392.
- Kato, N., 2002. Seismic cycle on a strike-slip fault with rate-and state-dependent strength in an elastic layer overlying a viscoelastic half-space, *Earth Planets Space*, 54(11), 1077–1083.
- King, G., 1983. The accommodation of large strains in the upper lithosphere of the earth and other solids by self-similar fault systems: the geometrical origin of b-value, *Pure appl. Geophys.*, **121**(5), 761–815.
- Kirby, R.M., Sherwin, S.J. & Cockburn, B., 2012. To CG or to HDG: a comparative study, J. Sci. Comput., 51(1), 183–212.
- Kopriva, D.A., Nordström, J. & Gassner, G.J., 2017. Error boundedness of discontinuous Galerkin spectral element approximations of hyperbolic problems, *J.f Sci. Comput.*, 72(1), 314–330.
- Kozdon, J., 2019. QDESDG, available at: https://github.com/jkozdon/QDE SDG.
- Krenz, L., Uphoff, C., Ulrich, T., Gabriel, A.-A., Abrahams, L.S., Dunham, E.M. & Bader, M., 2021. 3D acoustic-elastic coupling with gravity: the dynamics of the 2018 Palu, Sulawesi Earthquake and Tsunami, in *Proceedings of the International Conference for High Performance Computing, Networking, Storage and Analysis, SC '21,* Association for Computing Machinery, New York, NY, USA, Article 63, 1–14, doi:10.1145/3458817.3476173.
- Kronbichler, M. & Kormann, K., 2019. Fast matrix-free evaluation of discontinuous Galerkin finite element operators, ACM Trans. Math. Softw. (TOMS), 45(3), 1–40.
- Kronbichler, M., Kormann, K., Pasichnyk, I. & Allalen, M., 2017. Fast matrix-free discontinuous Galerkin kernels on modern computer architectures, in *International Supercomputing Conference*, pp. 237–255, Springer.
- Lapusta, N. & Liu, Y., 2009. Three-dimensional boundary integral modeling of spontaneous earthquake sequences and aseismic slip, *J. geophys. Res.: Solid Earth*, **114**(B9), doi:10.1029/2008JB005934.
- Lapusta, N., Rice, J.R., Ben-Zion, Y. & Zheng, G., 2000. Elastodynamic analysis for slow tectonic loading with spontaneous rupture episodes on faults with rate- and state-dependent friction, *J. geophys. Res.: Solid Earth*, 105(B10), 23765–23789.

- Lapusta, N. et al., 2019. Modeling earthquake source processes: from tectonics to dynamic rupture, Report to the National Science Foundation, available at: http://www.seismolab.caltech.edu/pdf/MESP_White_P aper_Main_Text_8_March_2019.pdf.
- Li, D. & Liu, Y., 2016. Spatiotemporal evolution of slow slip events in a nonplanar fault model for northern Cascadia subduction zone, *J. geophys. Res.: Solid Earth*, 121(9), 6828–6845.
- Li, D. & Liu, Y., 2017. Modeling slow-slip segmentation in Cascadia subduction zone constrained by tremor locations and gravity anomalies, J. geophys. Res.: Solid Earth, 122(4), 3138–3157.
- Liu, D., Duan, B. & Luo, B., 2020. EQsimu: a 3-D finite element dynamic earthquake simulator for multicycle dynamics of geometrically complex faults governed by rate-and state-dependent friction, *Geophys. J. Int.*, 220(1), 598–609.
- Liu, Y. & Rice, J.R., 2005. Aseismic slip transients emerge spontaneously in three-dimensional rate and state modeling of subduction earthquake sequences, *J. geophys. Res.: Solid Earth*, 110(B8), doi:10.1029/2004JB 003424.
- Luo, B., Duan, B. & Liu, D., 2020. 3D finite-element modeling of dynamic rupture and aseismic slip over earthquake cycles on geometrically complex faults, *Bull. seism. Soc. Am.*, 110(6), 2619–2637.
- Luo, Y., Ampuero, J.P., Galvez, P., van den Ende, M. & Idini, B., 2017. QDYN: A Quasi-DYNamic earthquake simulator (v1.1) (qdyn_1.1), Zenodo, doi:10.5281/zenodo.322459.
- Mazzieri, I., Stupazzini, M., Guidotti, R. & Smerzini, C., 2013. SPEED: SPectral Elements in Elastodynamics with Discontinuous Galerkin: a non-conforming approach for 3D multi-scale problems, *Int. J. Numer. Methods Eng.*, 95(12), 991–1010.
- Mckay, M.B., Erickson, B.A. & Kozdon, J.E., 2019. A computational method for earthquake cycles within anisotropic media, *Geophys. J. Int.*, 219(2), 816–833.
- Meurer, A. et al., 2017. SymPy: symbolic computing in Python, PeerJ Comput. Sci., 3, e103, doi:10.7717/peerj-cs.103.
- Mia, M.S., Abdelmeguid, M. & Elbanna, A., 2021. Self-limiting earthquake dynamics and spatio-temporal clustering of seismicity enabled by offfault plasticity, *Earth*, doi:10.31223/X50P8B.
- Milner, K.R., Shaw, B.E., Goulet, C.A., Richards-Dinger, K.B., Callaghan, S., Jordan, T.H., Dieterich, J.H. & Field, E.H., 2021. Toward physicsbased nonergodic PSHA: A prototype fully deterministic seismic hazard model for Southern California, *Bull. seism. Soc. Am.*, 111(2), 898–915.
- Mindlin, R.D., 1936. Force at a point in the interior of a semi-infinite solid, *Physics*, 7(5), 195–202.
- Moczo, P. et al., 2021. Numerical wave propagation simulation, in *The 6th IASPEI/IAEE International Symposium: Effects of Surface Geology on Seismic Motion*, available at: http://www.nuquake.eu/Publications/Moczo_etal_ESG2021.pdf.
- Oeser, J., Bunge, H.-P. & Mohr, M., 2006. Cluster design in the earth sciences: Tethys, in *International Conference on High Performance Computing and Communications*, pp. 31–40, Springer.
- Okada, Y., 1992. Internal deformation due to shear and tensile faults in a half-space, *Bull. seism. Soc. Am.*, **82**(2), 1018–1040.
- Ozawa, S., Ida, A., Hoshino, T. & Ando, R., 2021. Large-scale earthquake sequence simulations of 3D geometrically complex faults using the boundary element method accelerated by lattice H-matrices on distributed memory computer systems, preprint (arXiv:2110.12165).
- Palmer, A.C. & Rice, J.R., 1973. The growth of slip surfaces in the progressive failure of over-consolidated clay, *Proc. R. Soc. London. A. Math. Phys. Sci.*, 332(1591), 527–548.
- Park, J.-O., Tsuru, T., Kodaira, S., Cummins, P.R. & Kaneda, Y., 2002. Splay fault branching along the Nankai subduction zone, *Science*, 297(5584), 1157–1160.
- Pelties, C., Gabriel, A.-A. & Ampuero, J.-P., 2014. Verification of an ADER-DG method for complex dynamic rupture problems, *Geosci. Model Develop.*, 7(3), 847–866.
- Perez-Silva, A., Li, D., Gabriel, A.-A. & Kaneko, Y., 2021. 3D modeling of long-term slow slip events along the flat-slab segment in the Guerrero seismic gap, Mexico, *Geophys. Res. Lett.*, 48(13), e2021GL092968, doi:10.1029/2021GL092968.

- Perrin, G., Rice, J.R. & Zheng, G., 1995. Self-healing slip pulse on a frictional surface, J. Mech. Phys. Solids, 43(9), 1461–1495.
- Petersen, M.D. et al., 2014. Documentation for the 2014 update of the United States national seismic hazard maps, Tech. rep., U.S. Geological Survey Open-File Report, 2014–1091, available at: http://pubs.er.usgs.gov/publication/ofr20141091.
- Plesch, A. et al., 2007. Community fault model (CFM) for Southern California, Bull. seism. Soc. Am., 97(6), 1793–1802.
- Pollitz, F.F., Wicks, C.W., Svarc, J.L., Phillips, E., Brooks, B.A., Murray, M.H. & Turner, R.C., 2021. Postseismic relaxation following the 2019 Ridgecrest, California, earthquake sequence, *Bull. seism. Soc. Am.*, 112(2), 734–749.
- Portela, A., Aliabadi, M.H. & Rooke, D.P., 1992. The dual boundary element method: effective implementation for crack problems, *Int. J. Numer. Methods Eng.*, 33(6), 1269–1287.
- Pranger, C., 2021. GARNET, available at: https://bitbucket.org/cpranger/garnet.
- Reinarz, A. et al., 2020. ExaHyPE: An engine for parallel dynamically adaptive simulations of wave problems, Comput. Phys. Commun., 254, 107251, doi:10.1016/j.cpc.2020.107251.
- Rice, J.R., 1993. Spatio-temporal complexity of slip on a fault, *J. geophys. Res.: Solid Earth*, **98**(B6), 9885–9907.
- Rice, J.R. & Ben-Zion, Y., 1996. Slip complexity in earthquake fault models, Proc. Natl. Acad. Sci. USA, 93, 3811–3818.
- Rice, J.R. & Tse, S.T., 1986. Dynamic motion of a single degree of freedom system following a rate and state dependent friction law, *J. geophys. Res.: Solid Earth,* **91**(B1), 521–530.
- Rivière, B., 2008. Discontinuous Galerkin Methods for Solving Elliptic and Parabolic Equations, Society for Industrial and Applied Mathematics.
- Rockwell, T.K., Dawson, T.E., Young Ben-Horin, J. & Seitz, G., 2015.
 A 21-event, 4,000-year history of surface ruptures in the Anza seismic gap, San Jacinto fault, and implications for long-term earthquake production on a major plate boundary fault, *Pure appl. Geophys.*, 172(5), 1143–1165.
- Rognes, M., Kirby, R. & Logg, A., 2009. Efficient assembly of H(div) and H(curl) conforming finite elements, SIAM J. Sci. Comp., 31(6), 4130–4151.
- Rokhlin, V., 1985. Rapid solution of integral equations of classical potential theory, J. Comput. Phys., 60(2), 187–207.
- Romanet, P. & Ozawa, S., 2022. Fully dynamic earthquake cycle simulations on a nonplanar fault using the spectral boundary integral element method (sBIEM), *Bull. seism. Soc. Am.*, **112**(1), doi:10.1785/0120210178.
- Romanet, P., Bhat, H.S., Jolivet, R. & Madariaga, R., 2018. Fast and slow slip events emerge due to fault geometrical complexity, *Geophys. Res. Lett.*, 45(10), 4809–4819.
- Romanet, P., Sato, D.S. & Ando, R., 2020. Curvature, a mechanical link between the geometrical complexities of a fault: application to bends, kinks and rough faults, *Geophys. J. Int.*, 223(1), 211–232.
- Ross, Z.E. et al., 2019. Hierarchical interlocked orthogonal faulting in the 2019 Ridgecrest earthquake sequence, *Science*, 366(6463), 346–351.
- Rubin, A.M. & Ampuero, J.-P., 2005. Earthquake nucleation on (aging) rate and state faults, *J. geophys. Res.: Solid Earth*, **110**, B11312, doi:10.1029/2005JB003686.
- Ruina, A., 1983. Slip instability and state variable friction laws, *J. geophys. Res.: Solid Earth*, **88**(B12), 10359–10370.
- Sato, D.S. & Ando, R., 2021. A log-linear time algorithm for the elastodynamic boundary integral equation method, *Eng. Anal. Boundary Elements*, 133, 407–450.
- Sato, D. S.K., Romanet, P. & Ando, R., 2020. Paradox of modelling curved faults revisited with general non-hypersingular stress Green's functions, *Geophys. J. Int.*, 223(1), 197–210.
- Schoeder, S., Wall, W.A. & Kronbichler, M., 2019. ExWave: a high performance discontinuous Galerkin solver for the acoustic wave equation, SoftwareX, 9, 49–54.
- Segall, P. & Bradley, A.M., 2012. Slow-slip evolves into megathrust earthquakes in 2D numerical simulations, *Geophys. Res. Lett.*, **39**(18), doi:10.1029/2012GL052811.

- Segall, P., Rubin, A.M., Bradley, A.M. & Rice, J.R., 2010. Dilatant strengthening as a mechanism for slow slip events, *J. geophys. Res.: Solid Earth*, 115(B12), doi:10.1029/2010JB007449.
- Shahbazi, K., 2005. An explicit expression for the penalty parameter of the interior penalty method, J. Comput. Phys., 205(2), 401–407.
- Tada, T., Fukuyama, E. & Madariaga, R., 2000. Non-hypersingular boundary integral equations for 3-D non-planar crack dynamics, *Comput. Mech.*, 25(6), 613–626.
- Tago, J., Cruz-Atienza, V.M., Virieux, J., Etienne, V. & Sánchez-Sesma, F.J., 2012. A 3D hp-adaptive discontinuous Galerkin method for modeling earthquake dynamics, *J. geophys. Res.: Solid Earth*, 117(B9), doi:10.1029/2012JB009313.
- Taufiqurrahman, T., Gabriel, A.-A., Li, D., Ulrich, T., Li, B., Carena, S., Verdecchia, A. & Gallovič, F., 2022. Conversations between earthquakes: dynamics and delays of the 2019 ridgecrest rupture sequence, *Res. Sq.*, doi:10.21203/rs.3.rs-1906712/v1.
- Templeton, E.L. & Rice, J.R., 2008. Off-fault plasticity and earthquake rupture dynamics: 1. Dry materials or neglect of fluid pressure changes, *J. geophys. Res.: Solid Earth*, **113**(B9), doi:10.1029/2007JB005529.
- Thakur, P., Huang, Y. & Kaneko, Y., 2020. Effects of low-velocity fault damage zones on long-term earthquake behaviors on mature strike-slip faults, *J. geophys. Res.: Solid Earth*, **125**(8), doi:10.1029/2020JB019587.
- Thomas, M.Y., Lapusta, N., Noda, H. & Avouac, J.-P., 2014. Quasi-dynamic versus fully dynamic simulations of earthquakes and aseismic slip with and without enhanced coseismic weakening, *J. geophys. Res.: Solid Earth*, **119**(3), 1986–2004.
- Tullis, T.E. et al., 2012. Generic earthquake simulator, Seismol. Res. Lett., 83(6), 959–963.
- Ulrich, T., Gabriel, A.-A., Ampuero, J.-P. & Xu, W., 2019. Dynamic viability of the 2016 Mw 7.8 Kaikōura earthquake cascade on weak crustal faults, *Nat. Commun.*, 10(1), 1213, doi:10.1038/s41467-019-09125-w.
- Ulrich, T., Gabriel, A.-A. & Madden, E.H., 2022. Stress, rigidity and sediment strength control megathrust earthquake and tsunami dynamics, *Nat. Geosci.*, 15(1), 67–73.
- Uphoff, C., 2020. Flexible model extension and optimisation for earthquake simulations at extreme scales, Dissertation, Technische Universität München, Munich.
- Uphoff, C. & Bader, M., 2020. Yet another tensor toolbox for discontinuous Galerkin methods and other applications, ACM Trans. Math. Softw., 46(4), doi:10.1145/3406835.
- Uphoff, C., Rettenberger, S., Bader, M., Madden, E.H., Ulrich, T., Wollherr, S. & Gabriel, A.-A., 2017. Extreme scale multi-physics simulations of the tsunamigenic 2004 Sumatra megathrust earthquake, in *Proceedings of the International Conference for High Performance Computing, Networking*,

- Storage and Analysis, SC '17, Association for Computing Machinery, New York, NY, USA, Article 21, 1–16, doi:10.1145/3126908.3126948.
- van Driel, M., Krischer, L., Stähler, S.C., Hosseini, K. & Nissen-Meyer, T., 2015. Instaseis: instant global seismograms based on a broadband waveform database, *Solid Earth*, **6**(2), 701–717.
- van Zelst, I., Rannabauer, L., Gabriel, A.-A. & van Dinther, Y., 2022. Earth-quake rupture on multiple splay faults and its effect on tsunamis, *J. geo-phys. Res.: Solid Earth*, 127(8), e2022JB024300, doi:10.1029/2022JB024300.
- Waldhauser, F., Schaff, D.P., Diehl, T. & Engdahl, E.R., 2012. Splay faults imaged by fluid-driven aftershocks of the 2004 Mw 9.2 Sumatra-Andaman earthquake, *Geology*, **40**(3), 243–246.
- Warburton, T., 2006. An explicit construction of interpolation nodes on the simplex, J. Eng. Math., 56, 247–262.
- Warburton, T., 2013. A low-storage curvilinear discontinuous Galerkin method for wave problems, SIAM J. Sci. Comput., 35(4), A1987–A2012.
- Warburton, T. & Hesthaven, J., 2003. On the constants in hp-finite element trace inverse inequalities, Comput. Methods Appl. Mech. Eng., 192(25), 2765–2773.
- Webber, S., Norton, K., Little, T., Wallace, L. & Ellis, S., 2018. How fast can low-angle normal faults slip? Insights from cosmogenic exposure dating of the active Mai'iu fault, Papua New Guinea, *Geology*, **46**(3), 227–230.
- Wendt, J., Oglesby, D.D. & Geist, E.L., 2009. Tsunamis and splay fault dynamics, Geophys. Res. Lett., 36(15), doi:10.1029/2009GL038295.
- Wilcox, L.C., Stadler, G., Burstedde, C. & Ghattas, O., 2010. A high-order discontinuous Galerkin method for wave propagation through coupled elastic-acoustic media, J. Comput. Phys., 229, 9373–9396.
- Williams, M.L., 1952. Stress singularities resulting from various boundary conditions in angular corners of plates in extension, *J. appl. Mech.*, 19(4), 526–528.
- Witherden, F. & Vincent, P., 2015. On the identification of symmetric quadrature rules for finite element methods, *Comput. Math. Appl.*, 69(10), 1232–1241
- Wolf, S., Galis, M., Uphoff, C., Gabriel, A.-A., Moczo, P., Gregor, D. & Bader, M., 2022. An efficient ADER-DG local time stepping scheme for 3D HPC simulation of seismic waves in poroelastic media, *J. Comput. Phys.*, 455, 110886, doi:10.1016/j.jcp.2021.110886.
- Wollherr, S., Gabriel, A.-A. & Uphoff, C., 2018. Off-fault plasticity in threedimensional dynamic rupture simulations using a modal Discontinuous Galerkin method on unstructured meshes: implementation, verification and application, *Geophys. J. Int.*, 214(3), 1556–1584.
- Yokota, R., Bardhan, J.P., Knepley, M.G., Barba, L.A. & Hamada, T., 2011. Biomolecular electrostatics using a fast multipole BEM on up to 512 GPUs and a billion unknowns, *Comput. Phys. Commun.*, **182**(6), 1272–1283

APPENDIX A: COERCIVITY AND BOUNDEDNESS

In eq. (24), the penalty δ_e needs to be chosen large enough such that the bilinear form a(u, v) is coercive, because it follows from coercivity that eq. (25) has a unique solution (Rivière 2008). However, the condition number of the matrix A resulting from eq. (25) increases with the penalty parameter (Antonietti & Houston 2011). That is, δ_e is ideally set to the lowest value that still ensures coercivity.

Explicit expressions for the penalty parameter are given by Shahbazi (2005) and Epshteyn & Rivière (2007) for a Poisson problem in which the coordinate transformation X_E is affine, that is, the element E is given by the planar D-simplex. In both papers, numerical experiments demonstrate that the estimate is sharp, that is, the lowest penalty parameter is close to its theoretical value. The estimates of the penalty parameter rely on the inverse trace inequality (Warburton & Hesthaven 2003)

$$\|u\|_{e} \le \sqrt{\frac{(N+1)(N+D)}{D} \frac{|e|}{|E|}} \|u\|_{E}, \quad \forall u \in P_{N}(E),$$
 (A1)

where E is a planar D-simplex, |E| is the volume of E, e is a facet of E and |e| is the length (D=2) or area (D=3) of e.

In the following, we find bounds for the penalty parameter for linear elasticity. Similarly to Shahbazi (2005) and Epshteyn & Rivière (2007) we restrict the analysis to affine mapping functions, because there are some unresolved difficulties for curvilinear coordinates. At the end of this section, we remark on these difficulties.

For the analysis of coercivity, we introduce the semi-norm

$$|\boldsymbol{u}|_{c,h} = \left(\sum_{E \in \mathcal{T}_h} \int_E \frac{\partial u_i}{\partial x_j} c_{ijrs} \frac{\partial u_r}{\partial x_s} \, \mathrm{d}\boldsymbol{x}\right)^{1/2} \tag{A2}$$

and the energy norm

$$\|\boldsymbol{u}\|_{*} = \left(|\boldsymbol{u}|_{c,h}^{2} + \sum_{e \in \Gamma^{i} \cup \Gamma^{D}} \int_{e} \delta_{e} [\![u_{i}]\!] [\![u_{i}]\!] \, \mathrm{d}s\right)^{1/2}.$$
(A3)

Moreover, we assume that the stiffness tensor is bounded, that is, let κ be a symmetric $D \times D$ matrix then we have on element E

$$0 < c_0^E \kappa_{ij} \kappa_{ij} \le \kappa_{ij} c_{ijkl} \kappa_{kl} \le c_1^E \kappa_{ij} \kappa_{ij}, \quad \forall \kappa \ne \mathbf{0}, \tag{A4}$$

where the constants c_0^E and c_1^E for the isotropic stiffness tensor c_{ijkl} are given by

$$c_0^E = \inf_{\mathbf{x} \in E} 2\mu(\mathbf{x}),$$

$$c_1^E = \sup_{\mathbf{x} \in E} \left(D\lambda(\mathbf{x}) + 2\mu(\mathbf{x}) \right).$$

Given assumption eq. (A4), we obtain the following bounds on the penalty parameter.

Theorem APPENDIX A.1 (Coercivity). Let X_E be an affine function (i.e. the Jacobian is constant). Moreover, let

$$\delta_e^*(\zeta) = \begin{cases} \frac{D+1}{4\zeta}(\beta_{e,1} + \beta_{e,2}) \text{ if } e \in \Gamma^i, \\ \frac{(D+1)}{\zeta}\beta_{e,1} \text{ if } e \in \Gamma^D, \end{cases}$$

where $0 < \zeta < 1$ and

$$\beta_{e,i} = \frac{N(N-1+D)}{D} \frac{|e|}{|E_i^e|} \frac{(c_1^{E_i^e})^2}{c_0^{E_i^e}}.$$

Then choosing $\delta_e > \delta_e^*(\zeta)$ ensures

$$a(\boldsymbol{u},\boldsymbol{u}) \ge k^*(\zeta) \|\boldsymbol{u}\|_*^2$$

with coercivity constant

$$k^*(\zeta) = \min \left\{ 1 - \zeta, \min_{e \in \Gamma^i \cup \Gamma^D} \left(1 - \frac{\delta_e^*(\zeta)}{\delta_e} \right) \right\}.$$

Proof. See Appendix A1.

Corollary APPENDIX A.1 (Boundedness).

$$a(u, u) \leq K^*(\zeta) \|u\|_*^2$$

with constant

$$K^*(\zeta) = \max\left\{1 + \zeta, \max_{e \in \Gamma^i \cup \Gamma^D} \left(1 + \frac{\delta_e^*(\zeta)}{\delta_e}\right)\right\}.$$

In practice, we do not expect equality to hold in Theorem A.1. Thus, we set δ_e to its limiting value, that is, $\delta_e = \delta_e^*(1)$. Moreover, the penalty parameter might also be adequate for curvilinear meshes with little distortion although a bound of the penalty parameter for the general case is desirable. The proof in Appendix A1 could be extended by establishing one of the following inequalities:

- (i)Prove the trace inequality $\|\boldsymbol{\varepsilon}(\boldsymbol{u})\|_{e} \leq C \|\boldsymbol{\varepsilon}(\boldsymbol{u})\|_{E}$ and determine the constant C, where we note that $\boldsymbol{\varepsilon}(\boldsymbol{u})$ is non-polynomial.
- (ii)Prove the 'discrete Korn's inequality' (e.g. Brenner 2004) for curved elements and determine the constant in the inequality.

A1 Proof of Theorem A.1

Several definitions are required before we proceed with the proof of Theorem A.1. For matrices A, B let $A : B = A_{ij}B_{ij}$. Given a vector-valued function m and a matrix-valued function M, on a facet e we will denote inner products via $\|m\|_e^2 = \int_e m \cdot m \, ds$ and $\|M\|_e^2 = \int_e M : M \, ds$. Inner products over a volume E will be denoted as $\|m\|_E^2 = \int_E m \cdot m \, dx$ and $\|M\|_E^2 = \int_E M : M \, dx$.

For improved readability of this section, we abbreviate the tensor contraction $c_{ijkl} \partial u_k / \partial x_l$ with $c \nabla u$. Using $\sigma(u) = c \nabla u$ the bilinear form is

$$a(\boldsymbol{u}, \boldsymbol{u}) = \sum_{E \in \mathcal{T}_L} \int_E \boldsymbol{\sigma}(\boldsymbol{u}) : \nabla \boldsymbol{u} \, d\boldsymbol{x} + \sum_{e \in \Gamma^i \cup \Gamma^D} \int_e \delta_e[\![\boldsymbol{u}]\!] \cdot [\![\boldsymbol{u}]\!] \, ds - 2 \sum_{e \in \Gamma^i \cup \Gamma^D} \int_e \{\boldsymbol{\sigma}(\boldsymbol{u})\boldsymbol{n}\} \cdot [\![\boldsymbol{u}]\!] \, ds . \tag{A5}$$

Note that the first two terms are equivalent to $\|u\|_{*}^{2}$, hence it is sufficient to find a lower bound for the last term.

We bound the last term in eq. (A5) using the Cauchy–Schwarz inequality:

$$\int_{e} \{\sigma(u)n\} \cdot \llbracket u \rrbracket \, \mathrm{d}s \le \|\{\sigma(u)n\}\|_{e} \|\llbracket u \rrbracket\|_{e}. \tag{A6}$$

Using the definition of the average, the triangle inequality, and recalling that |n| = 1, we have

$$\|\{\sigma(u)n\}\|_{e} \leq \frac{1}{2} \|c\nabla u|_{E_{1}^{e}}\|_{e} + \frac{1}{2} \|c\nabla u|_{E_{2}^{e}}\|_{e}. \tag{A7}$$

We denote the square root of stiffness tensor c with $c^{1/2}$. The square root has the property $c_{ijrs}^{1/2}c_{rskl}^{1/2}=c_{ijrs}$. For an isotropic stiffness tensor, the square root can be shown to be given by $c_{ijkl}^{1/2} = a\delta_{ij}\delta_{kl} + b(\delta_{ik}\delta_{jl} + \delta_{il}\delta_{jk})$, where $\lambda = Da^2 + 4ab$ and $\mu = 2b^2$. Using the square root $c^{1/2}$, $c\nabla u = c\varepsilon(u)$, and property (A4) we have on element E

$$c\nabla u : c\nabla u \le (c_1^E)^2 \varepsilon(u) : \varepsilon(u). \tag{A8}$$

Conversely, we have

$$c_0^E \boldsymbol{\varepsilon}(\boldsymbol{u}) : \boldsymbol{\varepsilon}(\boldsymbol{u}) \le \nabla \boldsymbol{u} : c \nabla \boldsymbol{u} = c^{1/2} \nabla \boldsymbol{u} : c^{1/2} \nabla \boldsymbol{u}. \tag{A9}$$

We proceed with bounding $\|\{\sigma(u)n\}\|_e$ using eq. (A8). As X_E is assumed to be affine we have $\varepsilon(u) \in [P_{N-1}(E)]^{D \times D}$ and eq. (A1) can be applied:

$$\begin{split} \|\{\sigma(u)n\}\|_{e} &\leq \frac{c_{1}^{E_{1}^{e}}}{2} \|\varepsilon(u)|_{E_{1}^{e}}\|_{e} + \frac{c_{1}^{E_{2}^{e}}}{2} \|\varepsilon(u)|_{E_{2}^{e}}\|_{e} \\ &\leq \frac{c_{1}^{E_{1}^{e}}\sqrt{\alpha_{e,1}}}{2} \|\varepsilon(u)\|_{E_{1}^{e}} + \frac{c_{1}^{E_{2}^{e}}\sqrt{\alpha_{e,2}}}{2} \|\varepsilon(u)\|_{E_{2}^{e}}, \end{split} \tag{A10}$$

where $\alpha_{e,i} := (N(N-1+D)/D)(|e|/|E_i^e|)$. With eq. (A9), we have

$$\|\{\sigma(u)n\}\|_{e} \leq \frac{\sqrt{\beta_{e,1}}}{2} \|c^{1/2}\nabla u\|_{E_{1}^{e}} + \frac{\sqrt{\beta_{e,2}}}{2} \|c^{1/2}\nabla u\|_{E_{2}^{e}}, \tag{A11}$$

where $\beta_{e,i} := \alpha_{e,i} (c_1^{E_i^e})^2 / c_0^{E_i^e}$. Similarly, we get for boundary facets

$$\int \{\sigma(u)n\} \cdot \llbracket u \rrbracket \, \mathrm{d}s \le \sqrt{\beta_{e,1}} \| c^{1/2} \nabla u \|_{E_1^e} \| \llbracket u \rrbracket \|_e. \tag{A12}$$

Summing over all edges and applying the Cauchy-Schwarz inequality, we obtain

$$\sum_{e \in \Gamma^{i} \cup \Gamma^{D}} \int_{e} \{ \boldsymbol{\sigma}(\boldsymbol{u}) \boldsymbol{n} \} \cdot [\![\boldsymbol{u}]\!] \, \mathrm{d}s \le \left((D+1) \sum_{E} \| \boldsymbol{c}^{1/2} \nabla \boldsymbol{u} \|_{E}^{2} \right)^{1/2}$$

$$\times \left(\sum_{e \in \Gamma^{i}} \frac{\beta_{e,1}}{4} \| [\![\boldsymbol{u}]\!] \|_{e}^{2} + \sum_{e \in \Gamma^{i}} \frac{\beta_{e,2}}{4} \| [\![\boldsymbol{u}]\!] \|_{e}^{2} + \sum_{e \in \Gamma^{D}} \beta_{e,1} \| [\![\boldsymbol{u}]\!] \|_{e}^{2} \right)^{1/2}$$
(A13)

The inequality $ab \le \zeta a^2/2 + b^2/(2\zeta)$ with $\zeta > 0$ (which follows from Young's inequality) is used to obtain

$$\sum_{e \in \Gamma^{l} \cup \Gamma^{D}} \int_{e} \{ \boldsymbol{\sigma}(\boldsymbol{u}) \boldsymbol{n} \} \cdot [\![\boldsymbol{u}]\!] dS \leq \frac{\zeta}{2} \sum_{E} \|\boldsymbol{c}^{1/2} \nabla \boldsymbol{u}\|_{E}^{2}
+ \frac{D+1}{2\zeta} \left(\sum_{P^{l}} \frac{\beta_{e,1}}{4} \|[\![\boldsymbol{u}]\!]\|_{e}^{2} + \sum_{P^{l}} \frac{\beta_{e,2}}{4} \|[\![\boldsymbol{u}]\!]\|_{e}^{2} + \sum_{P^{l}} \beta_{e,1} \|[\![\boldsymbol{u}]\!]\|_{e}^{2} \right).$$
(A14)

Inserting eq. (A14) into eq. (A5) yields

$$a(\boldsymbol{u}, \boldsymbol{u}) \geq (1 - \zeta) \sum_{E} \| \boldsymbol{c}^{1/2} \nabla \boldsymbol{u} \|_{E}^{2}$$

$$+ \sum_{e \in \Gamma^{i}} \left(\delta_{e} - \frac{D+1}{4\zeta} \left(\beta_{e,1} + \beta_{e,2} \right) \right) \| \boldsymbol{u} \|_{e}^{2}$$

$$+ \sum_{e \in \Gamma} \left(\delta_{e} - \frac{D+1}{\zeta} \beta_{e,1} \right) \| \boldsymbol{u} \|_{e}^{2}. \tag{A15}$$

Provided that $0 < \zeta < 1$, the first term is in eq. (A15) is always positive. Finally, we ensure the remaining two terms in eq. (A15) are always positive by selecting δ_e such that the result in parenthesis is greater than zero, that is,

$$\delta_e > \left\{ \begin{array}{l} \frac{D+1}{4\zeta}(\beta_{e,1}+\beta_{e,2}) \text{ if } e \in \Gamma^i, \\ \frac{(D+1)}{\zeta}\beta_{e,1} \text{ if } e \in \Gamma^D, \end{array} \right.$$

such that Theorem A.1 follows.

Theorem A.1 follows from noting that

$$-\int_{e} \{\sigma n\} \cdot \llbracket u \rrbracket \, \mathrm{d}s \le \|\{\sigma n\}\|_{e} \|\llbracket u \rrbracket\|_{e}. \tag{A16}$$